

Electronic Thesis and Dissertation Repository

9-10-2020 10:30 AM

Mechanistic Insights into Analyte Charge Enhancement using Mass Spectrometry and Molecular Dynamics Simulations

Leanne Martin, *The University of Western Ontario*

Supervisor: Konermann, Lars, *The University of Western Ontario*

A thesis submitted in partial fulfillment of the requirements for the Master of Science degree in Chemistry

© Leanne Martin 2020

Follow this and additional works at: <https://ir.lib.uwo.ca/etd>

Recommended Citation

Martin, Leanne, "Mechanistic Insights into Analyte Charge Enhancement using Mass Spectrometry and Molecular Dynamics Simulations" (2020). *Electronic Thesis and Dissertation Repository*. 7336.
<https://ir.lib.uwo.ca/etd/7336>

This Dissertation/Thesis is brought to you for free and open access by Scholarship@Western. It has been accepted for inclusion in Electronic Thesis and Dissertation Repository by an authorized administrator of Scholarship@Western. For more information, please contact wlsadmin@uwo.ca.

Abstract

Electrospray ionization mass spectrometry (ESI-MS) is a powerful technique to investigate proteins and many other analytes. However, many fundamental aspects of ESI remain poorly understood. In this thesis, we use a combination of molecular dynamics (MD) simulations and experiments to gain insights into the hidden complexities of ESI-MS. The structure and reactivity of electrosprayed protein ions is governed by their net charge. In Chapter 2, we sought to uncover the mechanistic basis of La^{3+} -induced charge enhancement. MD simulations showed that irreversible binding via multidentate contacts suppressed La^{3+} ejection from the vanishing droplets, such that the resulting gaseous proteins carried significantly more charge. In Chapter 3, we examined the supercharging effects of sulfolane on the ESI behavior of salt clusters using similar methods. Spiking NaI solutions with sulfolane resulted in the formation of highly charged cluster ions. MD simulations illustrate that sulfolane stabilizes the cluster to support additional charge. These results demonstrate that the combination of MS experiments and MD simulations can uncover intricate aspects of ESI mechanisms.

Keywords: Proteins, Electrospray Ionization Mass Spectrometry, Supercharging, Molecular Dynamics Simulations, Salt Clusters

Summary for Lay Audience

Proteins are important biological macromolecules that play a key role in virtually all cellular functions. A widely used technique to study proteins is electrospray ionization mass spectrometry (ESI-MS). A protein solution is introduced into the mass spectrometer through a charged capillary, which produces a plume of droplets that subsequently shrink as the solvent evaporates. The droplets contain charge carriers (including H^+ , Na^+ and NH_4^+) that are transferred to the protein through various mechanisms. The mass spectrometer then detects these charged gas phase proteins. Increasing the charge of these protein ions with solution additives known as “supercharging” agents (SCAs) improves the mass resolution for many experiments. However, the mechanism by which SCAs increase charge is still unclear.

In this thesis, we investigate the role of SCAs using ESI-MS experiments and molecular dynamics (MD) simulations. MD simulations are a computational tool used to model changes in molecular systems. Recently, it has become possible to apply this approach to ESI droplets. Here, we explore how $LaCl_3$ supercharges proteins. Our results show that La^{3+} tightly binds to the protein early in the ESI process, creating more highly charged protein ions than a singly charged metal counterpart (such as Na^+). In a subsequent chapter, we investigate the role of an organic SCA, sulfolane, during experiments on NaI salt clusters. The addition of sulfolane to NaI solution does indeed increase the charge of salt clusters. MD simulations reveal that sulfolane has stabilizing effects that enable the NaI clusters to support additional charge. Our results reveal how MD simulations can explain ESI mechanisms that we cannot investigate using mass spectrometry experiments.

Co-Authorship Statement

The work in Chapter 2 was reproduced with permission from:

Martin, L. M.; Konermann, L. Enhancing Protein Electrospray Charge States by Multivalent Metal Ions: Mechanistic Insights from MD Simulations and Mass Spectrometry Experiments. *J. Am. Soc. Mass Spectrom.* **2020**, *31*, 25–33. Copyright © 2020, American Chemical Society [featured on journal cover].

All experimental work was performed and analyzed by the author, Leanne Martin. The original draft for the above article was prepared by the author. Subsequent revisions were done by the author and Dr. Lars Konermann. All experimental work was performed under the supervision of Dr. Lars Konermann.

Acknowledgments

The work in this thesis would not have been possible without so many significant people who provided me with endless support and encouragement.

First, I would like thank Dr. Lars Konermann for allowing me to join his lab in September 2018. Under Lars' leadership, I have grown so much as a chemist and I am so grateful for his unwavering patience and guidance throughout this entire degree program. Lars explains concepts in the most understandable way and is the best lecturer I have ever heard. I am so pleased I was able to be a member of his lab for the past two years.

I would like to thank my committee members Dr. Ken Yeung and Dr. Patrick O'Donoghue for their valuable feedback on my work. I would also like to extend my sincere thanks to Sandra Zakaria Holtslag, Barakat Misk, Darlene McDonald, and Mike Brandt in the Chemistry department for their assistance during my graduate studies.

The best part of working in the lab was interacting with my amazing colleagues. A very special thank you to Victor, who answered every one of my relentless questions and always offered training, direction and words of encouragement. Nastaran, Vincent, Pablo, Alex, Haidy, Angela, Justin, and Derek always provided helpful comments on my work and I am so appreciative of their help. My dearest chemistry friends Elnaz, Insa and Megan always offered much needed emotional support, and I cannot overstate what their presence has meant to me.

I would also like to thank my parents Angie and Darrell Martin for encouraging me to pursue graduate studies and supporting me through everything I do in life. Thank you to my friends in KW and Ottawa for their reassurance in my abilities. Finally, thank you to Ryan Miller for his kindness, humour and love throughout this endeavor. I would not be the person I am today without each of these important people, and their support over the past two years has been immeasurable.

Table of Contents

Abstract	ii
Summary for Lay Audience	iii
Co-Authorship Statement	iv
Acknowledgments	v
Table of Contents	vi
List of Symbols and Abbreviations	viii
Chapter 1. Introduction	1
1.1 Proteins.....	1
1.2 Biophysical Techniques to Investigate Protein Structure	2
1.3 Mass Spectrometry	3
1.4 Ion Mobility Spectrometry and Collision Cross Sections.....	5
1.5 Electrospray Ionization Mechanisms	7
1.6 ESI Supercharging.....	10
1.6.1 Native Supercharging	11
1.6.2 Denaturing Supercharging.....	13
1.7 Molecular Dynamics (MD) Simulations.....	15
1.7.1 Force Fields	15
1.7.2 Applying MD Techniques to ESI Droplets.....	16
1.7.3 Comparison of MD Simulation Results and Experimental Data	17
1.8 Scope of the Thesis	18
1.9 References	19
Chapter 2. Enhancing Protein Electrospray Charge States by Multivalent Metal Ions: Mechanistic Insights from MD Simulations and Mass Spectrometry Experiments..	24
2.1 Introduction	24
2.2 Methods.....	27
2.2.1 Native ESI-MS and IMS	27
2.2.2 MD Simulations	27
2.3 Results and Discussion.....	29
2.3.1 Native ESI-MS	29

2.3.2	Charge Carriers for Droplet Simulations	31
2.3.3	Charge States of MD-Generated Protein Ions.....	32
2.3.4	Anatomy of the ESI Process.....	35
2.3.5	Mechanism of La ³⁺ Enhanced Protein Charging	40
2.3.6	Gas Phase Conformations	49
2.4	Conclusions	51
2.5	References	53
Chapter 3. Exploring the Effects of Supercharging Agents on Salt Clusters Generated During Electrospray Ionization		58
3.1	Introduction	58
3.2	Methods.....	60
3.2.1	Native ESI-MS and IMS	60
3.2.2	MD Simulations	61
3.3	Results and Discussion.....	63
3.3.1	ESI-MS of NaI Solutions	63
3.3.2	MD Simulations of Salt-Containing Electrospray Droplets.....	69
3.4	Conclusions	77
3.5	References	78
Chapter 4. Conclusions and Future Directions.....		81
4.1	Conclusions	81
4.2	Future Directions.....	82
4.3	References	83
Appendix I – Permissions.....		85
Curriculum Vitae.....		86

List of Symbols and Abbreviations

CEM	Chain Ejection Model
CHARMM	Chemistry at Harvard Molecular Mechanics
Ω	Collision Cross Section
CID	Collision-Induced Dissociation
CRM	Charged Residue Model
DC	Direct Current
ESI	Electrospray Ionization
FT-ICR	Fourier Transform Ion Cyclotron Resonance
hMb	Holomyoglobin
IEM	Ion Evaporation Model
IMS	Ion Mobility Spectrometry
m/z	Mass to Charge Ratio
MALDI	Matrix-Assisted Laser Desorption/Ionization
MD	Molecular Dynamics
MS	Mass Spectrometry
MS/MS	Tandem Mass Spectrometry
PDB	Protein Data Bank
RF	Radio Frequency
SCA	Supercharging Agent
t_D	Drift Time
TOF	Time of Flight

TWIMS	Traveling Wave Ion Mobility Spectrometry
Ubq	Ubiquitin
z_D	Droplet Charge
z_R	Rayleigh Charge

Chapter 1. Introduction

1.1 Proteins

Proteins are biological macromolecules that participate in virtually all physiological processes. There are four levels of protein structure.¹ Protein chains have a well-defined sequence of amino acids (primary structure) that are linked by amide bonds. These chains fold into secondary structures such as α -helices or β -sheets, which are stabilized by intramolecular hydrogen bonds. Non-covalent interactions between secondary structures including van der Waals and hydrophobic contacts, as well as salt bridges give rise to the formation of tertiary structure. The interaction of two or more protein chains through intermolecular contacts is described as the quaternary structure^{1,2} (Figure 1.1).

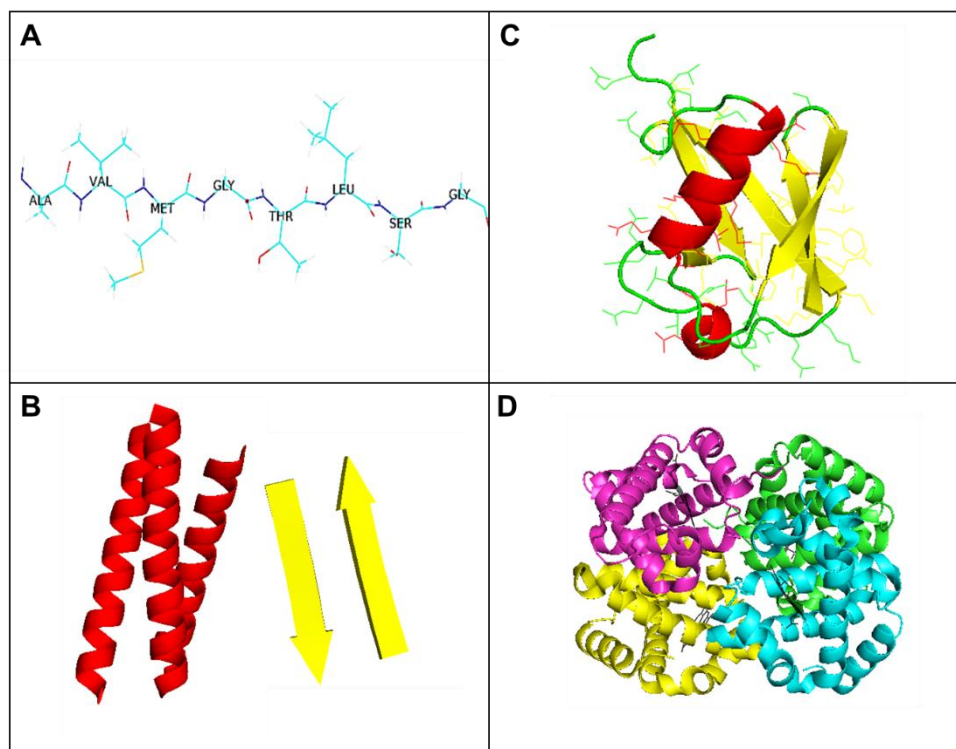


Figure 1.1 (A) Amino acid sequence of a protein chain. (B) Secondary structure consisting of α -helices (red) (PDB:1COS)³ or β -sheets (yellow)(PDB:3NI3).⁴ (C) Tertiary structure (PDB:1UBQ)⁵ forms from non-covalent interactions between secondary structure elements. (D) Quaternary structure (PDB:2QSS)⁶ arises from the interaction of two or more protein chains.

The structure of proteins governs their dynamics and function. The biologically active, folded conformation is referred to as the native state. Thermal or chemical denaturation causes proteins to adopt disordered, unfolded conformations.^{7,8} Aggregation of unfolded proteins is involved in many disease mechanisms,^{9,10} and therefore the study of protein structure and dynamics plays a critical role for developing novel therapeutic approaches. Proteins are the main drug target for the treatment of disease and a thorough understanding of the folding, structure, function and dynamics of proteins is necessary to develop high-affinity drug candidates.¹¹ In addition, proteins rarely function as isolated entities. Instead, they participate in large networks of protein-protein interactions.¹² Examining how these protein complexes interact and function is critical to understand physiological processes. Modern advances in analytical methods used to study protein structure and function have allowed scientists to investigate larger and more complex systems.¹³⁻¹⁵ The ongoing improvement of analytical methods also broadens the scope for practical applications. For example, high-resolution structure determination methods (discussed below) have led to improvements in targeted drug design for personalized medicine.¹⁶ Advances in analytical methodologies used to study proteins rely on an in-depth understanding of how these methods work. Thus, elucidating mechanistic aspects of analytical methods will yield novel avenues for exploring structural biology and proteomics. The quest to develop a better understanding of how protein-related analytical methods work represents the key goal of this thesis.

1.2 Biophysical Techniques to Investigate Protein Structure

Optical methods such as fluorescence or circular dichroism spectroscopy can be used to garner basic information regarding protein secondary and tertiary structure. Fluorescence spectroscopy can provide insights into the relative positioning of intrinsic fluorophores within the protein (i.e. buried or on the surface), and fluorescent labeling can reveal whether a protein binds to a ligand. However, the exact location of ligand binding, as well as mechanistic details, cannot be elucidated.¹⁷ Circular dichroism can be used to investigate which secondary structures are prevalent for a protein in solution, but it must be combined with reference data from additional methods.¹⁸ Techniques such as X-ray

crystallography, cryo-electron microscopy and nuclear magnetic resonance spectroscopy can yield more detailed structural information.

X-ray crystallography can be used to obtain the atomistic structure of a molecule in a crystal. Exposure of crystallized proteins to an X-ray beam yields diffraction patterns that provide information about the locations of individual atoms, with a resolution down to one Angstrom or even lower. However, this technique is limited by the necessity of crystallizing a purified, highly concentrated sample. This process is difficult and time-consuming, as experimental conditions may not allow the protein to be crystallized.¹⁹ Cryo-electron microscopy involves imaging frozen protein samples with an electron beam. This method may be used to determine protein structural information at near-atomic resolution by incorporating numerous 2D images to reconstruct 3D structures. NMR spectroscopy can be used to investigate protein structures in solution. This technique applies radio frequency radiation to a sample that is exposed to a strong magnetic field. Nuclei with spin including ¹H, ¹³C, and ¹⁵N report on the chemical environment of individual atoms and can be used to elucidate protein structures.^{17,20}

1.3 Mass Spectrometry

An extremely important class of methods for studying protein structure and dynamics involves the use of mass spectrometry (MS). Advanced structural information including high-resolution sequence coverage,^{21,22} post-translational modification sites,^{14,23,24} and ligand binding affinities^{14,25,26} can be obtained by using MS-based techniques. The three main components of a mass spectrometer are the ion source, the mass analyzer, and the detector. Gaseous ions are produced in the ion source, separated by their mass to charge ratio (m/z) by the mass analyzer, and quantified by the detector.^{13,27,28} Different means of ionization can be used to introduce analytes into the instrument. For example, Matrix-Assisted Laser Desorption/Ionization (MALDI) involves embedding the analyte in a matrix of small UV (or IR)-absorbing molecules. This is followed by desorption of matrix and analyte molecules from a surface using a laser. The gaseous analyte becomes charged via proton transfer from matrix ions.²⁹ Electrospray Ionization (ESI) produces gaseous ions by spraying an analyte-containing solution through a thin

capillary with an applied voltage in the kV range. As the electrospray droplets undergo rapid desolvation, charge is transferred to the analyte via different mechanisms (see details below). Both MALDI and ESI are “soft” ionization techniques as they can transfer macromolecular analytes into the gas phase without inducing fragmentation. ESI tends to produce ions that are more highly charged than in MALDI.^{13,29,30}

Mass analyzers separate ions according to their m/z . Several types of mass analyzers exist, including Fourier-transform ion cyclotron (FT-ICR) instruments, Orbitraps, quadrupoles and Time of Flight (TOF) analyzers. Time of Flight (TOF) instruments will be the focus of the following discussion, as it is the type of instrument that was used for the present work. TOF mass analyzers accelerate ions by a high voltage pulse at the pusher and subsequently, the ions travel through a field-free region.³¹ The potential energy, E_{pot} , of each ion generated from the applied voltage pulse is converted to kinetic energy, E_{kin} , according to Eqs 1.1-1.2:

$$E_{pot} = E_{kin} \quad \text{Eq 1.1}$$

$$ze\Delta U = \frac{1}{2}mv^2 \quad \text{Eq 1.2}$$

where z = charge state of the ion, e = elementary charge, ΔU = applied voltage, m = mass of the ion and v = speed of the ion. The speed of the ion along the flight path is thus dictated by its mass and charge.²⁷ Eq 1.2 can be rearranged to indicate how m/z influences the speed of the ion:

$$v = \sqrt{\frac{2\Delta Ue}{m/z}} \quad \text{Eq 1.3}$$

Ions with a lower m/z will reach the detector first.³² However, ions with the same m/z may have slightly different kinetic energies because of spatial positioning distributions in the pusher. This broadens the arrival times of ions with the same m/z , thereby decreasing the spectral resolution. Modern instruments solve this problem by employing a reflectron,

which increases the resolution by acting as an ion mirror, reversing the flight direction of the ions based on their kinetic energies.^{32,33} The further into the ion mirror an ion travels, the stronger the repulsive electric field becomes. Higher energy ions penetrate farther into the ion mirror and thus travel a slightly longer path. This allows two ions possessing the same m/z but slightly different kinetic energies to reach the detector at the same time, increasing the resolution by limiting peak broadening.²⁷ TOFs possess a high transmission efficiency, and all ions are detected by a multichannel plate detector. These characteristics imply that TOF mass analyzers have a high sensitivity.³³ Each ion that hits the detector produces an electrical signal. By tallying these individual ion count events, an intensity vs. m/z distribution is obtained, which (after proper calibration) represents the mass spectrum.

A quadrupole can be used as a mass filter to select for ions with a specific m/z . It consists of four parallel rod-shaped electrodes that carry both a radio frequency (RF) and direct current (DC) voltages. Only ions with a specific m/z will be transmitted through the quadrupole, as governed by the amplitude of voltages and the RF frequency. All other ions will have unstable trajectories and crash into one of the rods. When only RF voltage is applied, all ions are transmitted and the quadrupole acts as a simple ion guide.³⁴

MS is often coupled to chromatographic separation techniques including gas chromatography and high-performance liquid chromatography, which allows an additional dimension of separation in solution, before separation in the gas phase.

1.4 Ion Mobility Spectrometry and Collision Cross Sections

Ion Mobility Spectrometry (IMS) is a complementary tool for the separation of gaseous ions.³⁵ Two protein ions with the same m/z may have different conformations. These structural differences give rise to different collision cross sections (CCS), represented by the symbol Ω .^{36,37} Ω describes the protein “size”, or more accurately, its rotationally averaged projection area. IMS is a useful tool to study the structures of gaseous protein ions, specifically to monitor the occurrence of unfolding events. Traveling Wave IMS or TWIMS works by applying RF voltages to a series of stacked rings in an ion guide.³⁸ Protein ions are pushed by DC waves that move along the ion guide and cause protein ions to undergo occasional ‘rollover’ events.³⁸ Large, unfolded species have larger

Ω values than their folded counterparts. Therefore, the former have longer drift times because they experience more frequent rollover events.³⁹ As a result, a TWIMS device separates ions according to their Ω/z .

The MS and IMS concepts outlined above are implemented in the instrument that was used for the current work, a SYNAPT HDMS G2Si Q-TOF (Waters, Milford MA) mass spectrometer (Figure 1.2). This instrument is equipped with an ESI source, quadrupole, Triwave for TWIMS, and a reflectron-TOF mass analyzer. In this work, the quadrupole simply acts as an ion guide. When inactivated, the Triwave also serves as a simple ion guide. Alternatively, the instrument can be operated in tandem MS (or MS/MS) mode, where specific precursor ions are selected in the quadrupole, fragmented in the trap cell, with subsequent fragment ions mass analysis in the TOF.

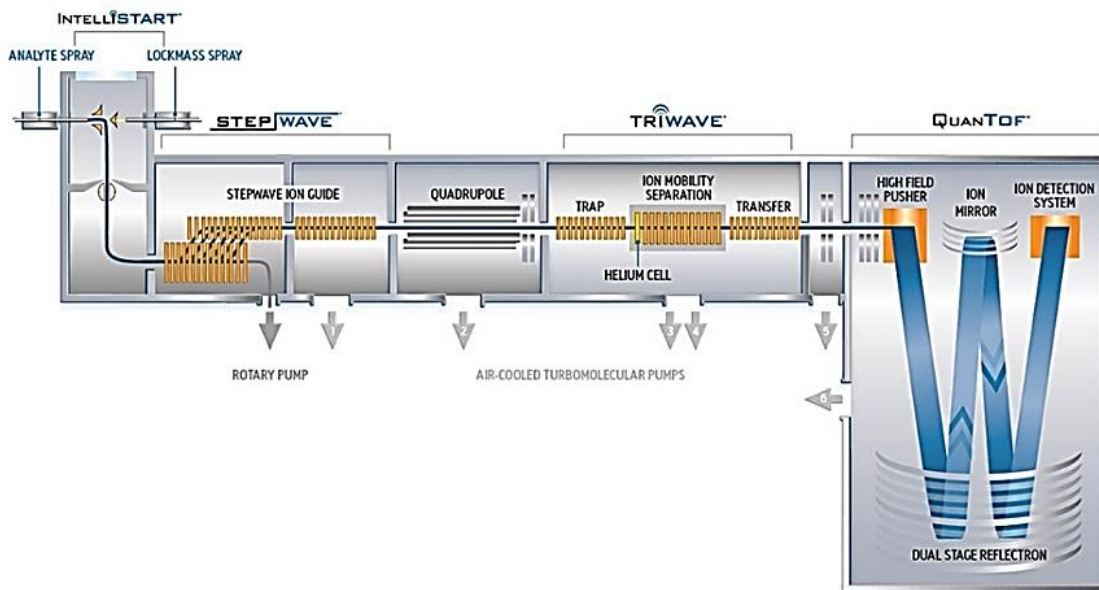


Figure 1.2 Schematic of a SYNAPT G2Si mass spectrometer (Waters, Milford MA).

1.5 Electrospray Ionization Mechanisms

Highly charged droplets of analyte solution that are emitted from a Taylor cone at the outlet of the ESI capillary undergo solvent evaporation and fission, ultimately culminating in the release of analyte ions into the gas phase.⁴⁰ In the commonly used positive ion mode, the excess droplet charge is due to the presence of cations such as H⁺, Na⁺, and NH₄⁺. The maximum charge that a droplet with radius r can sustain is represented by Eq 1.4, the Rayleigh charge,⁴¹ z_R :

$$z_R = \frac{8\pi\sqrt{(\varepsilon_0\gamma r^3)}}{e} \quad \text{Eq 1.4}$$

where γ = surface tension, ε_0 = vacuum permittivity, and e = elementary charge.¹³ As the solvent evaporates, the droplet radius decreases and the droplet charge, z_D approaches z_R . This buildup of charge density continues until $z_D \approx z_R$, at which point either the emission of small charged offspring droplets or the ejection of solvated charge carriers from the droplet surface takes place.^{42,43} Following these charge reduction events, Coulombic repulsion is reduced, and the droplet enters a regime where it is temporarily stable. As solvent continues to evaporate, z_D once again approaches z_R and additional fission or ion ejection events occur. The ejection of small solvated charge carriers from the droplet surface is described by the Ion Evaporation Model (Figure 1.3A).⁴⁴

Proteins ESI mechanisms and the charge states of the resulting multiply charged $[M + zH]^{z+}$ ions depend on the protein conformation in solution. Under non-denaturing ('native') ESI conditions, globular proteins tend to follow the Charged Residue Model (CRM).⁴⁵ During the CRM, droplets evaporate to dryness. This droplet shrinkage is accompanied by the IEM ejection of small charge carriers. As the last solvent layers disappear, the remaining charges are transferred to the protein (Figure 1.3B).^{13,40,45} Because the shrinking droplets stay close to the Rayleigh limit, the resulting protein charge tends to be close to the z_R of a protein-sized water droplet.^{46,47} Native proteins formed via the CRM tend to have a narrow distribution of low charge states. While native protein MS does not yield high-level structural information, coexisting species in solution can be probed simultaneously. In addition, the stoichiometry of protein-ligand and protein-protein

complexes can be elucidated under native ESI conditions, complementary to other biophysical methods.¹⁷

Under denaturing conditions (e.g. in acidified solvent mixtures), proteins unfold.^{48–50} The presence of exposed hydrophobic residues forces the protein to migrate to the droplet surface. The protein chain then ejects, driven by electrostatic repulsion between the chain and the remaining droplet charges.⁵¹ As the protein chain leaves the droplet, charge migration along the chain is facilitated by the high mobility of H^+ in water and in desolvated proteins.^{52–54} Highly charged ions arise as mobile H^+ migrate across the protein chain in equilibrium with the droplet to minimize electrostatic repulsion. This process describes the Chain Ejection Model (CEM) (Figure 1.3C). Generating highly charged protein ions is advantageous for fragmentation carried out in the collision cell of the mass spectrometer.⁵⁵ Protein ions generated via the CEM tend to have a broad charge state distribution because of differences in droplet size as well as fluctuations in protein conformation as chains leave the droplet.^{13,56}

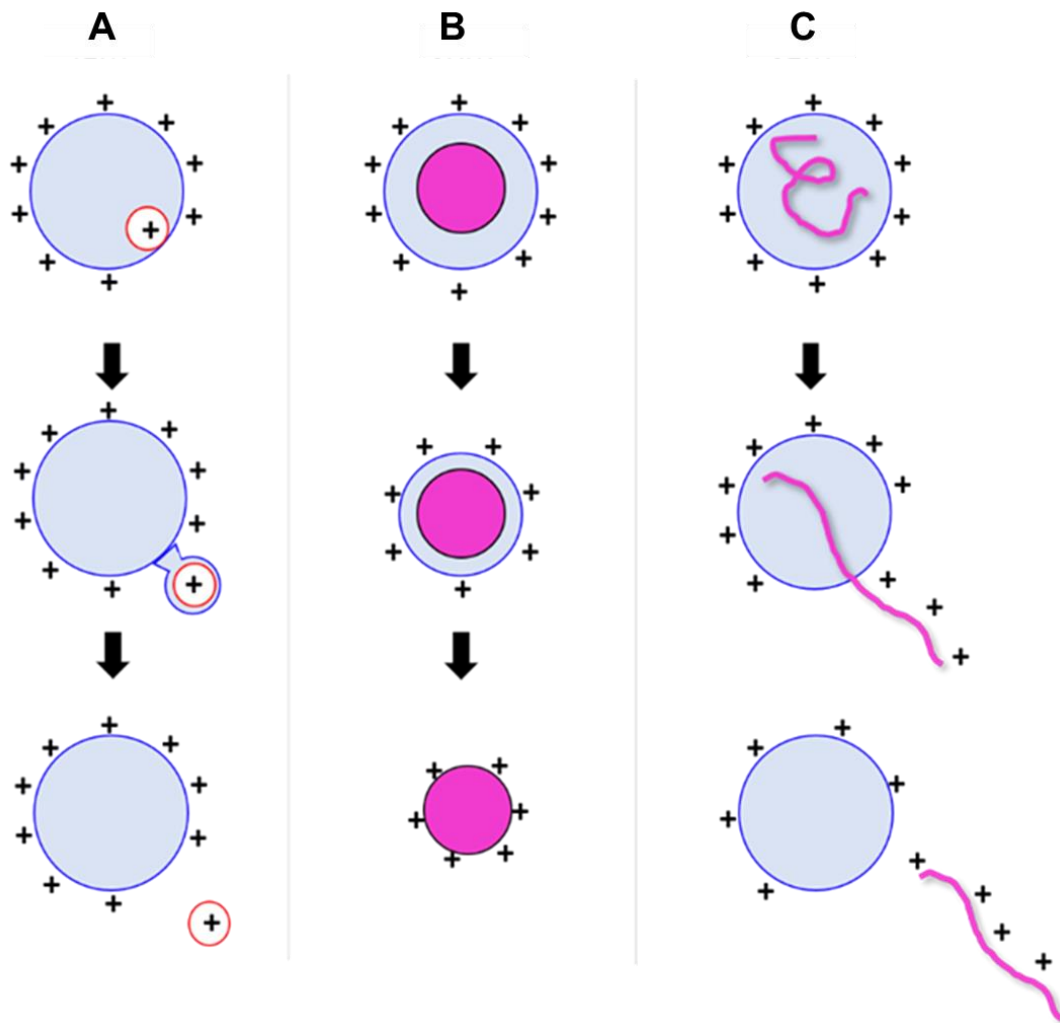


Figure 1.3 Proposed mechanisms for the formation of gaseous ions during ESI. (A) Small charge carriers will follow the IEM, whereas proteins may follow (B) the CRM or (C) the CEM depending on their conformation.

1.6 ESI Supercharging

Means of increasing the ESI charge states of proteins with low concentrations of solution additives (or ‘supercharging’) has become an active field of research. Common supercharging agents (SCAs) include organic cosolvents such as sulfolane, *m*-nitrobenzyl alcohol, or butylene carbonate, among others (Figure 1.4).⁵⁷⁻⁵⁹ Supercharging is useful for tandem MS, where precursor ions with a specific *m/z* are selectively fragmented using techniques such as electron capture/transfer dissociation (ECD/ETD) or collision-induced dissociation (CID) to reveal sequence information.⁵⁷ Supercharging protein ions has a marked effect on their fragmentation efficiency. Methods including ECD and ETD fragment the peptide backbone at N-C_α bonds, producing *c* and *z*[•] ions.⁶⁰ The electron capture/transfer cross section describes the effective area within which an electron or radical anion must be to be captured.⁶¹ The capture/transfer cross section increases with charge, implying that supercharged protein ions will undergo facilitated ECD/ETD. CID relies on collisional heating to fragment the peptide backbone at carbonyl-N bonds, forming *b* and *y* ions.^{13,27,62} For CID, Eq 1.5 describes how *m/z* influences the speed of the ion; ions with the same mass but different charge states *z* will have different velocities:

$$v = \sqrt{\frac{z2\Delta Ue}{m}} \quad \text{Eq 1.5}$$

From Eq 1.5, it becomes apparent that increasing the charge of the ion increases its velocity. Faster ions will collide with neutral gas molecules at higher energies and thus fragment with higher efficiency.^{61,63} Increasing the fragmentation efficiency yields better sequence coverage. Thus, boosting the magnitude of *z* will generally enhance the fragmentation efficiency of protein ions, which is the reason why supercharging is so important.

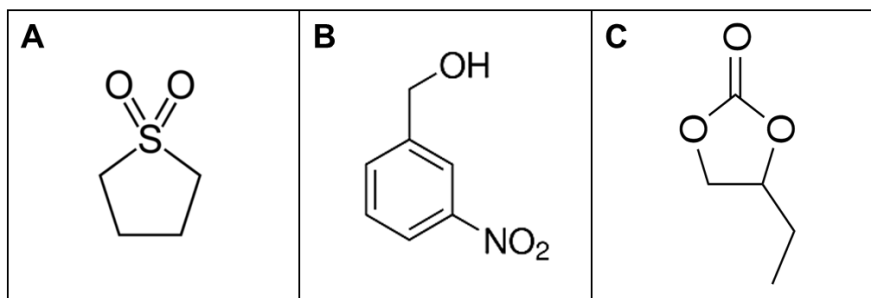


Figure 1.4 Molecular structure of common supercharging agents (A) sulfolane, (B) *m*-nitrobenzyl alcohol, and (C) butylene carbonate

SCAs have lower volatilities and larger dipole moments than water. Under typical experimental concentrations (1-5% v/v), SCAs do not affect protein structure or stability in bulk solution.^{59,64} However, due to their low volatility they become strongly enriched in the final ESI nanodroplets that release protein ions into the gas phase. The mechanisms by which SCAs enhance protein charge states are poorly understood, bringing forth various contradicting theories that are briefly summarized below.^{57,64-66}

1.6.1 Native Supercharging

ESI of folded proteins under native conditions produces low charge states via the CRM. However, the charge state can be increased by adding SCAs into solution.^{58,67} Protein unfolding within the droplet has been proposed as an avenue for native supercharging, an idea that is supported (to some extent) by the observation of increased Ω values of some supercharged proteins (Figure 1.5A).^{57,68} However, Ω values are measured after the protein is completely desolvated, and is prone to unfolding in the gas phase. This phenomenon can be explained by the electrostatic repulsion, F , experienced by two charges, described by Coulomb's Law, Eq 1.6:

$$F = \frac{1}{4\pi\epsilon_0} \frac{1}{\epsilon} \cdot \frac{q_1 q_2}{r^2} \quad \text{Eq 1.6}$$

where ϵ_0 = vacuum permittivity, ϵ = relative permittivity, q = the charge of each atom and r = the distance between the atoms. In a vacuum, the relative permittivity ϵ is 1; whereas in water, the permittivity value is 80.¹⁷ When there is no solvent available, the positive charges on the protein experience 80 times stronger repulsive forces than in water, so the protein will easily unfold. Therefore, the fact that some supercharged proteins are unfolded does not necessarily support the view that unfolding is the root cause of supercharging, instead gas phase unfolding could be the *result* of supercharging.^{67,69} Also, some supercharged proteins preserve native-like compactness in the gas phase⁷⁰ with preservation of protein-protein and protein-ligand-binding,^{58,71} an observation that is difficult to reconcile with the unfolding model.

Surface tension effects attributed to SCAs have also been explored as a possible explanation of native protein supercharging.⁵⁷ Increasing surface tension would allow a droplet at Z_R to sustain more charge before becoming unstable and potentially lead to the formation of highly charged protein ions under CRM conditions (Figure 1.5B).⁴¹ However, experiments using solvents with surface tensions lower than water yield no shifts in charge state distributions.⁷² In addition, the enrichment of some SCAs actually decreases the surface tension of aqueous droplets.⁶⁴ Thus, the formation of highly charged protein ions does not seem to be strongly dependent on the surface tension of the solvent.

Another proposed model for native protein supercharging is that SCAs suppress the IEM ejection of charge carriers. This model is referred to as “charge trapping”.^{67,73} Typically, charge carriers are mobile in aqueous droplets and undergo IEM ejection until late-stage desolvation when charge binds to the protein via the CRM. Previous work has shown that SCA-containing ESI droplets form an aqueous core surrounded by a highly ordered SCA solvation shell near the surface. Charge carriers have poor solubility in SCA and remain trapped in the aqueous core near the protein, thereby suppressing IEM ejection. As the final water molecules leave the droplet, the trapped charge carriers irreversibly bind to the protein (Figure 1.5C).⁶⁷ This results in the formation of highly charged protein ions. This model provides an explanation for the observation that proteins can preserve a somewhat native conformation in the gas phase and maintain ligand-binding.⁷⁴

Alternative SCAs that do not disrupt protein structure in solution continue to be investigated. Work by Flick and Williams⁷⁵ revealed that LaCl_3 as a solution additive can

be used to enhance protein charge states in native MS. Clearly, this type of SCA is very different from the compounds discussed above, all of which were small organic molecules (Figure 1.4). Non-specific La^{3+} adduction also showed improved protein fragmentation efficiency and sequence coverage.⁷⁵ However, it remains unclear how La^{3+} enhances the charge states of protein ions, as mechanistic aspects of the ESI process are difficult to probe experimentally. Thus, additional analytical tools must be used to explain the mechanism of La^{3+} -induced supercharging. Elucidating this mechanism is a key goal of the present work.

1.6.2 Denaturing Supercharging

Denaturing ESI conditions tend to produce highly charged protein ions. The charge states of the protein can be further increased by adding SCAs to solution. Under denaturing conditions, the formation of an outer SCA solvation shell does not seem to be the main mechanism of action, unlike the “charge trapping” model for native supercharging. Instead, the supercharging mechanism in denaturing ESI relies on the low volatility and the large dipole moments of SCAs.^{51,66} Low volatility causes SCA molecules to remain attached to the protruding protein tail during the early stages of CEM ejection. These SCA molecules stabilize protonated basic sites via strong charge-dipole interactions. Solvent-mediated charge stabilization prevents H^+ migration back to the droplet, allowing the protein chain to accommodate additional charge^{51,59} (Figure 1.5D).

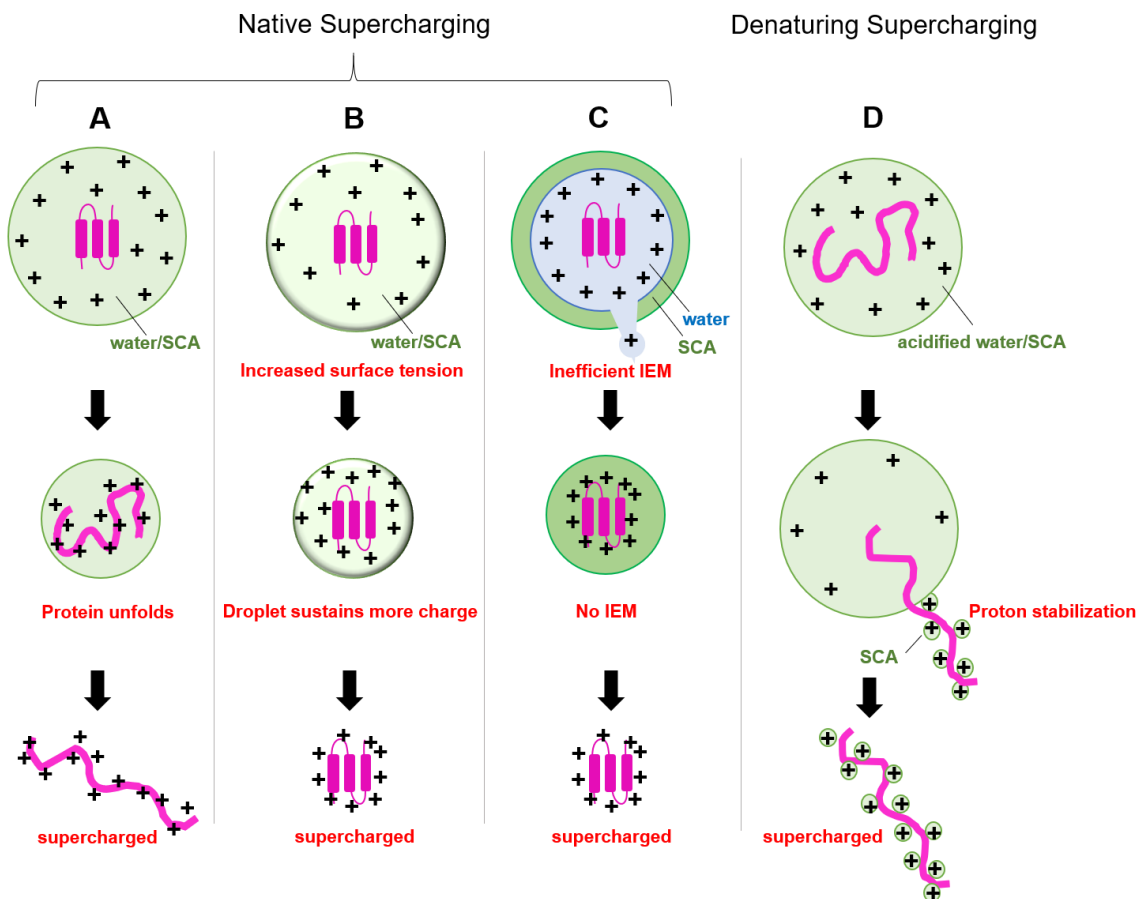


Figure 1.5 Proposed mechanisms for supercharging protein ions. (A) unfolding model, (B) surface tension model and (C) “charge trapping” model describe possible supercharging mechanisms under native ESI conditions. (D) solvent-mediated charge stabilization describes denaturing supercharging behavior.

1.7 Molecular Dynamics (MD) Simulations

Molecular Dynamics (MD) simulations are a computational technique that can be used to model the dynamic evolution of chemical systems containing many atoms as a function of time.⁷⁶ In traditional MD simulations, one or more molecules of interest (often proteins) are placed in a simulation box, surrounded by solvent, and allowed to run at a certain temperature for a certain time interval. X-ray crystal structures can be used as the starting point for protein MD runs. As the simulation progresses, the positions of atoms within the system are iteratively recalculated based on the integration of Newton's second law of motion $F = ma$. Traditionally, MD simulations have been used to probe the behaviour of proteins in bulk solution. More recently, several research groups have started to use MD methods for investigating mechanistic aspects of the ESI process by simulating the behavior of ESI droplets.^{51,67,77}

1.7.1 Force Fields

MD Force fields represent a set of parameters that define the atoms in the system. Individual atoms interact via covalent bonds (or "bonded contacts"), as well as non-bonded contacts. The latter include electrostatic interactions defined by Coulomb's law which can be repulsive or attractive, (Eq 1.7 Figure 1.6A):

$$U_E = \frac{1}{4\pi\epsilon_0} \cdot \frac{q_1q_2}{r} \quad \text{Eq 1.7}$$

Van der Waals interactions, dispersion forces, as well as short range repulsion among atoms are modeled via Lennard-Jones potential energies, U_{L-J} (Eq 1.8, Figure 1.6B):

$$U_{L-J} = 4\epsilon \left(\left(\frac{\sigma}{r} \right)^{12} - \left(\frac{\sigma}{r} \right)^6 \right) \quad \text{Eq 1.8}$$

where ϵ = depth of the local potential well. σ is the r value where the potential is zero; both σ and ϵ are distinct for different types of atoms in the force field. At short range,

the repulsive component $\left(\frac{\sigma}{r}\right)^{12}$ dominates, whereas at long range the attractive component $\left(\frac{\sigma}{r}\right)^6$ takes over. These parameters are typically derived from density functional theory (DFT) calculations. A commonly used force field for proteins in solution is the Chemistry at Harvard Molecular Mechanics (CHARMM),⁷⁸ which is used in the present work.

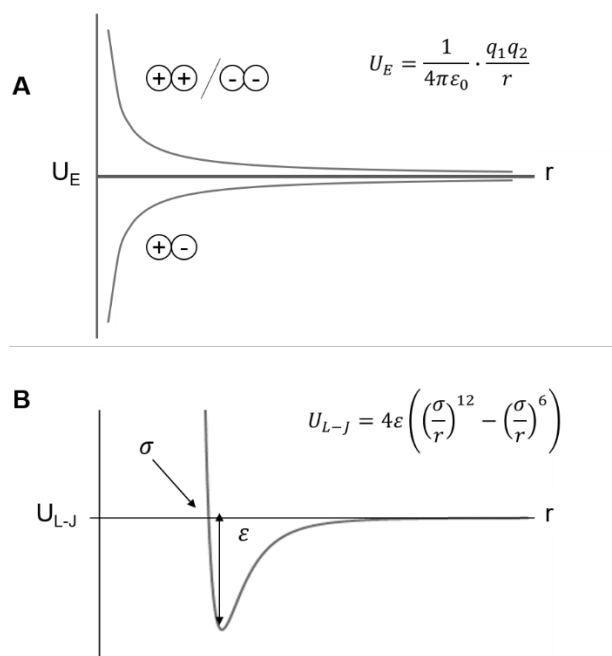


Figure 1.6 Forces acting on non-bonded atoms within an MD forcefield. (A) Coulombic (electrostatic) potential increases or decreases as a function of the distance between two atoms depending on their charge. (B) Lennard-Jones Potentials are dominated by short range repulsive forces and long-range attraction.

1.7.2 Applying MD Techniques to ESI Droplets

Continuous developments in MD simulations have allowed the development of models that tend to correlate well with experimental results. Previous studies exploring the ESI process have utilized MD simulations to computationally emulate what is occurring to highly charged droplets during the final stages of ESI. This includes the ejection of small ions via the IEM,^{74,79,80} the CRM behavior of compact folded proteins and peptides^{74,81} and the CEM process for unfolded proteins.⁷⁴ These computational models accurately reflect the previously discussed ESI mechanisms in Figure 1.3.

Standard MD simulations are run in bulk solution to limit artifacts from gas-surface interactions.⁸² In such cases, a quasi-infinite solvent environment is created by applying periodic boundary conditions (PBC). In this technique, the simulation box is surrounded by images of itself in three dimensions where molecules can leave on one side of the box and reappear in an adjacent cell.⁸³ This allows the system to utilize graphics processing unit packages to decrease computational time.

PBC conditions cannot be used to simulate systems with a net positive charge, (such as positively charged ESI droplets) because the charge of the PBC system would be infinite, and the simulation would be unstable.⁸⁴ To simulate aqueous droplets in a vacuum, a pseudo-PBC method is used.⁸⁵ The PBC box size, as well as Coulombic and Lennard-Jones interaction cut-offs, are increased. This prevents interactions between the PBC images while decreasing computational time and allows the user to simulate a droplet with a net-positive charge, which would not be possible under normal PBC conditions. Ions defined with mass, charge and Lennard-Jones parameters are introduced into the system and allowed to freely interact with the protein and solvent.⁸⁵ Different water models can be used to solvate the system. The TIP4P-2005⁸⁶ model is well suited for droplet simulations, as the addition of a ‘dummy’ site creates a 4-point molecule that accurately recreates water surface tension.

1.7.3 Comparison of MD Simulation Results and Experimental Data

MD simulations of ESI droplets culminate in the production of gaseous ions. The reliability of the simulations can be tested by comparing MD data with experimental observables. For example, the MD-generated charge states of protein ions can be compared to charge states seen in experimental mass spectra. In addition, the Ω values of a protein ion in the simulation can be compared to the conformations of protein ions measured by IMS. Collidoscope⁸⁷ is an open-source software that can be used to calculate Ω values of MD-generated protein conformers. This software uses the Trajectory Method to explicitly model the protein interactions with a buffer gas (He or N₂) as it travels through a drift tube or TWIMS device.⁸⁷ For protein conformations that are known with reasonable certainty,

the Ω values produced from Collidoscope are typically within a few percent of experimentally obtained ion mobility Ω values.^{51,88} Thus, the reliability of MD simulation results can be tested through comparisons of experimental and MD-simulated Ω values.

1.8 Scope of the Thesis

Supercharging is a promising strategy for increasing the ESI charge states of proteins under non-denaturing conditions. The mechanisms of action for SCAs are incompletely understood and we sought to thoroughly examine how different supercharging reagents influence protein ionization.

Chapter 2 provides an investigation of the effects of LaCl_3 as an SCA. We combined ESI-MS experiments with MD simulations to uncover the mechanism by which La^{3+} affects protein charge states. We also sought to investigate if currently available MD simulation strategies could probe the subtle effects of salt-induced charge enhancement to protein structure. Our findings indicate that early and irreversible binding of trivalent metal cations to the protein at acidic residues is responsible for the increased ESI charge states.

Chapter 3 is somewhat more “fundamental”, in that it examines the supercharging effects of sulfolane on the ESI behavior of salt solutions, without proteins. Specifically, we combined ESI-MS experiments with MD simulations to scrutinize the validity of the charge trapping theory. This model predicts that sulfolane should promote the formation of more highly charged salt clusters. Our preliminary findings indicate that the addition of sulfolane to aqueous solutions of NaI increases the charge state of the resulting clusters, but our data point to a mechanism that is somewhat different from the charge trapping model that was discussed above.

1.9 References

- 1 R. H. Garrett, C. H. Grisham, S. Andreopoulos, W. G. Willmore and I. G. Gallouz, *Biochemistry: 1st Canadian Edition*, Nelson Education, Toronto, Ontario, 2014.
- 2 A. Lehninger, *Biochemistry: The Molecular Basis of Cell Structure and Function (2nd Edition)*, Worth Publishing, New York, NY, 1975.
- 3 B. Lovejoy, S. Choe, D. Cascio, D. McRorie, W. DeGrado and D. Eisenberg, *Science*, 1993, **259**, 1288–1293.
- 4 O. Khakshoor, A. J. Lin, T. P. Korman, M. R. Sawaya, S.-C. Tsai, D. Eisenberg and J. S. Nowick, *J. Am. Chem. Soc.*, 2010, **132**, 11622–11628.
- 5 S. Vijay-Kumar, C. E. Bugg and W. J. Cook, *J. Mol. Biol.*, 1987, **194**, 531–544.
- 6 R. Aranda, H. Cai, C. E. Worley, E. J. Levin, R. Li, J. S. Olson, G. N. Phillips and M. P. Richards, *Proteins*, 2009, **75**, 217–230.
- 7 K. A. Dill and J. L. MacCallum, *Science*, 2012, **338**, 1042–1046.
- 8 N. N. Tajoddin and L. Konermann, *Anal. Chem.*, 2020, **92**, 10058–10067.
- 9 C. A. Ross and M. A. Poirier, *Nat. Med.*, 2004, **10**, S10.
- 10 S. Ahmadi, S. L. Zhu, R. Sharma, D. J. Wilson and H. B. Kraatz, *J. Inorg. Biochem.*, 2019, **194**, 44–51.
- 11 T. M. Bakheet and A. J. Doig, *Bioinformatics*, 2009, **25**, 451–457.
- 12 B. Schwikowski, P. Uetz and S. Fields, *Nat. Biotechnol.*, 2000, **18**, 1257–1261.
- 13 P. Kebarle and U. H. Verkerk, *Mass Spectrom. Rev.*, 2009, **28**, 898–917.
- 14 S. Mehmood, T. M. Allison and C. V. Robinson, *Annu. Rev. Phys. Chem.*, 2015, **66**, 453–474.
- 15 D. S. Chorev, L. A. Baker, D. Wu, V. Beilsten-Edmands, S. L. Rouse, T. Zeev-Ben-Mordehai, C. Jiko, F. Samsudin, C. Gerle, S. Khalid, A. G. Stewart, S. J. Matthews, K. Grünwald and C. V. Robinson, *Science*, 2018, **362**, 829–834.
- 16 S. A. Dugger, A. Platt and D. B. Goldstein, *Nat. Rev. Drug Discov.*, 2018, **17**, 183–196.
- 17 I. Campbell, *Biophysical Techniques*, Oxford University Press, New York, NY, 2012.
- 18 S. Khrapunov, *Anal. Biochem.*, 2009, **389**, 174–176.

- 19 M. S. Smyth and J. H. J. Martin, *J. Clin. Pathol. - Mol. Pathol.*, 2000, **53**, 8–14.
- 20 H. Van Den Bedem and J. S. Fraser, *Nat. Methods*, 2015, **12**, 307–318.
- 21 D. F. Hunt, J. R. Yates, J. Shabanowitz, S. Winston and C. R. Hauer, *Proc. Natl. Acad. Sci. U. S. A.*, 1986, **83**, 6233–6237.
- 22 N. R. Barthélemy, F. Fenaille, C. Hirtz, N. Sergeant, S. Schraen-Maschke, J. Vialaret, L. Buée, A. Gabelle, C. Junot, S. Lehmann and F. Becher, *J. Proteome Res.*, 2016, **15**, 667–676.
- 23 M. Mann and O. N. Jensen, *Nat. Biotechnol.*, 2003, **21**, 255–261.
- 24 H. J. Yoo, N. Wang, S. Zhuang, H. Song and K. Håkansson, *J. Am. Chem. Soc.*, 2011, **133**, 16790–16793.
- 25 S. M. Clark and L. Konermann, *Anal. Chem.*, 2005, **76**, 7077–7083.
- 26 G. T. H. Nguyen, T. N. Tran, M. N. Podgorski, S. G. Bell, C. T. Supuran and W. A. Donald, *ACS Cent. Sci.*, 2019, **5**, 308–318.
- 27 J. H. Gross, *Mass Spectrometry Third Edition*, Springer International Publishing, Cham, Switzerland, 2017.
- 28 A. C. Leney and A. J. R. Heck, *J. Am. Soc. Mass Spectrom.*, 2017, **28**, 5–13.
- 29 S. A. Trauger, W. Webb and G. Siuzdak, *Spectroscopy*, 2002, **16**, 15–28.
- 30 T. R. Covey, B. A. Thomson and B. B. Schneider, *Mass Spectrom. Rev.*, 2009, **28**, 870–897.
- 31 J. A. Loo, *Int. J. Mass Spectrom.*, 2000, **200**, 175–186.
- 32 I. A. Kaltashov and S. J. Eyles, *Mass Spectrometry in Structural Biology and Biophysics: Architecture, Dynamics, and Interaction of Biomolecules*, John Wiley & Sons, Hoboken, NJ, 2012.
- 33 A. N. Verentchikov, W. Ens and K. G. Standing, *Anal. Chem.*, 1994, **66**, 126–133.
- 34 P. E. Miller and M. B. Denton, *J. Chem. Educ.*, 1986, **63**, 617–623.
- 35 E. Jurneczko and P. E. Barran, *Analyst*, 2011, **136**, 20–28.
- 36 K. B. Shelimov and M. F. Jarrold, *J. Am. Chem. Soc.*, 1997, **119**, 2987–2994.
- 37 S. Ghassabi Kondalaji, M. Khakinejad, A. Tafreshian and S. J. Valentine, *J. Am. Soc. Mass Spectrom.*, 2017, **28**, 947–959.
- 38 A. A. Shvartsburg and R. D. Smith, *Anal. Chem.*, 2008, **80**, 9689–9699.

- 39 Y. Sun, S. Vahidi, M. A. Sowole and L. Konermann, *J. Am. Soc. Mass Spectrom.*, 2016, **27**, 31–40.
- 40 L. Konermann, E. Ahadi, A. D. Rodriguez and S. Vahidi, *Anal. Chem.*, 2013, **85**, 2–9.
- 41 L. Rayleigh, *Philos. Mag. J. Sci.*, 1882, **14**, 184–186.
- 42 A. Gomez and K. Tang, *Phys. Fluids*, 1994, **6**, 404–414.
- 43 R. L. Grimm and J. L. Beauchamp, *J. Phys. Chem. A*, 2010, **114**, 1411–1419.
- 44 J. V. Iribarne and B. A. Thomson, *J. Chem. Phys.*, 1976, **64**, 2287–2294.
- 45 M. Dole, L. L. Mack, R. L. Hines, D. O. Chemistry, R. C. Mobley, L. D. Ferguson and M. B. Alice, *J. Chem. Phys.*, 1968, **49**, 2240–2249.
- 46 F. J. de la Mora, *Anal. Chim. Acta*, 2000, **406**, 93–104.
- 47 R. G. McAllister, H. Metwally, Y. Sun and L. Konermann, *J. Am. Chem. Soc.*, 2015, **137**, 12667–12676.
- 48 A. Dobo and I. A. Kaltashov, *Anal. Chem.*, 2001, **73**, 4763–4773.
- 49 J. Li, C. Santambrogio, S. Brocca, G. Rossetti, P. Carloni and R. Grandori, *Mass Spectrom. Rev.*, 2016, **35**, 111–122.
- 50 J. A. Loo, C. G. Edmonds, H. R. Udseth and R. D. Smith, *Anal. Chem.*, 1990, **62**, 693–698.
- 51 I. Peters, H. Metwally and L. Konermann, *Anal. Chem.*, 2019, **91**, 6943–6952.
- 52 M. Chen, L. X. Zheng, B. Santra, H. Y. Ko, R. A. DiStasio, M. L. Klein, R. Car and X. F. Wu, *Nat. Chem.*, 2018, **10**, 413–419.
- 53 Y. Peng, J. M. J. Swanson, S. G. Kang, R. Zhou and G. A. Voth, *J. Phys. Chem. B*, 2015, **119**, 9212–9218.
- 54 S. Cukierman, *Biochim. Biophys. Acta - Bioenerg.*, 2006, **1757**, 876–885.
- 55 A. T. Iavarone and E. R. Williams, *Int. J. Mass Spectrom.*, 2002, **219**, 63–72.
- 56 H. Metwally, Q. Duez and L. Konermann, *Anal. Chem.*, 2018, **90**, 10069–10077.
- 57 A. T. Iavarone and E. R. Williams, *J. Am. Chem. Soc.*, 2003, **125**, 2319–2327.
- 58 S. H. Lomeli, S. Yin, R. R. Ogorzalek Loo and J. A. Loo, *J. Am. Soc. Mass Spectrom.*, 2009, **20**, 593–596.
- 59 C. A. Teo and W. A. Donald, *Anal. Chem.*, 2014, **86**, 4455–4462.

- 60 J. E. P. Syka, J. J. Coon, M. J. Schroeder, J. Shabanowitz and D. F. Hunt, *Proc. Natl. Acad. Sci. U. S. A.*, 2004, **101**, 9528 LP – 9533.
- 61 R. A. Zubarev, N. L. Kelleher and F. W. McLafferty, *J. Am. Chem. Soc.*, 1998, **120**, 3265–3266.
- 62 R. A. Zubarev, A. R. Zubarev and M. M. Savitski, *J. Am. Soc. Mass Spectrom.*, 2008, **19**, 753–761.
- 63 M. W. Senko, J. P. Speir and F. W. McLafferty, *Anal. Chem.*, 1994, **66**, 2801–2808.
- 64 S. H. Lomeli, I. X. Peng, S. Yin, R. R. Ogorzalek Loo and J. A. Loo, *J. Am. Soc. Mass Spectrom.*, 2010, **21**, 127–131.
- 65 R. R. Ogorzalek Loo, R. Lakshmanan and J. A. Loo, *J. Am. Soc. Mass Spectrom.*, 2014, **25**, 1675–93.
- 66 K. A. Douglass and A. R. Venter, *J. Am. Soc. Mass Spectrom.*, 2012, **23**, 489–497.
- 67 H. Metwally, R. G. McAllister, V. Popa and L. Konermann, *Anal. Chem.*, 2016, **88**, 5345–5354.
- 68 C. C. Going and E. R. Williams, *Anal. Chem.*, 2015, **87**, 3973–3980.
- 69 H. J. Sterling, A. F. Kintzer, G. K. Feld, C. A. Cassou, B. A. Krantz and E. R. Williams, *J. Am. Soc. Mass Spectrom.*, 2012, **23**, 191–200.
- 70 Z. Hall, A. Politis, M. F. Bush, L. J. Smith and C. V. Robinson, *J. Am. Chem. Soc.*, 2012, **134**, 3429–3438.
- 71 H. Metwally, R. G. McAllister, V. Popa and L. Konermann, *Anal. Chem.*, 2016, **88**, 5345–5354.
- 72 M. Šamalíková and R. Grandori, *J. Am. Chem. Soc.*, 2003, **125**, 13352–13353.
- 73 H. Metwally and L. Konermann, *Anal. Chem.*, 2018, **90**, 4126–4134.
- 74 L. Konermann, H. Metwally, Q. Duez and I. Peters, *Analyst*, 2019, **144**, 6157–6171.
- 75 T. G. Flick and E. R. Williams, *J. Am. Soc. Mass Spectrom.*, 2012, **23**, 1885–1895.
- 76 M. Karplus and J. A. McCammon, *Nat. Struct. Biol.*, 2002, **9**, 646–652.
- 77 S. Consta and J. K. Chung, *J. Phys. Chem. B*, 2011, **115**, 10447–10455.
- 78 J. Huang and A. D. Mackerell, *J. Comput. Chem.*, 2013, **34**, 2135–2145.
- 79 S. Consta, *J. Mol. Struct. THEOCHEM*, 2002, **591**, 131–140.
- 80 V. Znamenskiy, I. Marginean and A. Vertes, *J. Phys. Chem. A*, 2003, **107**, 7406–7412.

- 81 D. Kim, N. Wagner, K. Wooding, D. E. Clemmer and D. H. Russell, *J. Am. Chem. Soc.*, 2017, **139**, 2981–2988.
- 82 J. Wong-ekkabut and M. Karttunen, *Biochim. Biophys. Acta - Biomembr.*, 2016, **1858**, 2529–2538.
- 83 E. Lindahl, in *Molecular Modeling of Proteins*, Humana Press, New York, NY, 2015, pp. 3–26.
- 84 C. Kutzner, S. Páll, M. Fechner, A. Esztermann, B. L. De Groot and H. Grubmüller, *J. Comput. Chem.*, 2015, **36**, 1990–2008.
- 85 L. Konermann, H. Metwally, R. G. McAllister and V. Popa, *Methods*, 2018, **144**, 104–112.
- 86 J. L. F. F. Abascal and C. Vega, *J. Chem. Phys.*, 2005, **123**, 234505.
- 87 S. A. Ewing, M. T. Donor, J. W. Wilson and J. S. Prell, *J. Am. Soc. Mass Spectrom.*, 2017, **28**, 587–596.
- 88 A. I. M. Sever and L. Konermann, *J. Phys. Chem. B*, 2020, **124**, 3667–3677.

Chapter 2. Enhancing Protein Electrospray Charge States by Multivalent Metal Ions: Mechanistic Insights from MD Simulations and Mass Spectrometry Experiments

2.1 Introduction

Metal ions are essential for the biological function of many proteins, e.g., as enzyme cofactors or as cellular signals that trigger conformational changes. Protein-metal binding takes place via multidentate contacts with electron-rich moieties. These include the side chains of Glu⁻, Asp⁻, Cys⁻, Asn, Gln, His, Met as well as backbone carbonyl oxygens.¹⁻³

Electrospray ionization (ESI) mass spectrometry (MS) offers several avenues for interrogating protein structure and dynamics.⁴⁻⁷ One of these is “native” ESI-MS, a strategy that uses neutral aqueous solutions and gentle ion sampling conditions. The low protein charge states⁸⁻¹⁰ generated during native ESI promote the preservation of solution-like conformations and interactions in the gas phase,^{7,11-19} thereby revealing binding interactions with various ligands including metal ions. The combination of native ESI-MS with ion mobility spectrometry (IMS) reports on structural events such as metal-induced conformational changes.²⁰⁻²⁵

Metal ions can also affect ESI experiments in undesired ways. The presence of non-volatile salts in analyte solutions tends to produce nonspecific adducts. For example, Na⁺ salts cause the formation of $[M + zH + n(\text{Na-H})]^{z+}$ species, where n adopts a range of values for any given charge state z .⁹ Analogous nonspecific binding takes place for other metals.^{19,26-29} These adducts cause peak splitting and low S/N ratios. This is in contrast to the clean $[M + zH]^{z+}$ signals generated from solutions that are free of nonvolatile salts.^{19,26-29}

The propensity of metal ions to form nonspecific adducts reflects the mechanism by which protein ions are formed during native ESI. Charged droplets generated at the emitter undergo solvent evaporation. This process dramatically increases the concentration of salts and other nonvolatile solutes.^{9,30} Evaporation takes place in concert with jet fission,^{9,31,32} ultimately generating nanometer-sized droplets. According to the charged residue model (CRM), proteins are released from these nanodroplets via solvent

evaporation to dryness.^{8-10,33} Nonspecific adducts are formed when nonvolatile solutes bind to the protein as the last solvent layers vanish.^{9,10,15,34,35}

While nonspecific metal adduction is undesirable in many ESI-MS experiments,^{19,26-29} it also has beneficial aspects. Adducts often give rise to interesting gas phase ion chemistry, stimulating investigations on the reactivity of peptides and proteins bound to mono-, di-, and trivalent metal ions.³⁶⁻⁴⁴ Also, multidentate protein-metal interactions formed by nonspecific Ca^{2+} and Mg^{2+} binding stabilizes electrosprayed protein complexes.⁴⁵

The current study addresses an intriguing discovery made by Flick and Williams,⁴⁶ who reported that nonspecific La^{3+} adduction enhances native ESI protein charge states by ~20%. Such charge state enhancements can be significant because they affect key properties of gaseous proteins including their transmission,⁴⁷ reactivity,⁴⁸ and detection.^{49,50} The low charge states normally generated by native ESI cause poor top-down fragmentation efficiencies.^{51,52} La^{3+} induced charge enhancement boosts top-down sequence coverage.⁴⁶ Hence, the possibility to modulate ESI charge states by La^{3+} could open up interesting experimental avenues.

Clearly, there are ways to boost protein charge states that go beyond the aforementioned La^{3+} effects. One approach is to use denaturing additives that cause unfolding.^{10,53,54} Solutions can also be supplemented with supercharging agents such as sulfolane or m-nitrobenzyl alcohol.^{10,55-58} The highest charge states are obtained when combining denaturation with supercharging.^{10,56-58} Protein ions generated in this way carry two to three times more charge than in native ESI, making them well suited for fragmentation experiments.^{51,52} However, solution-phase denaturation and/or electrostatic gas phase unfolding renders such conditions unsuitable for experiments aimed at preserving native-like structures.^{10,58} Charge enhancement by La^{3+} could be attractive in cases that require more subtle control of the ESI process.⁴⁶

The mechanism whereby La^{3+} enhances protein charge states remains unclear. Flick and Williams proposed that La^{3+} binds to native-like proteins at some point during ESI,⁴⁶ but this scenario remains to be proven. Also, this proposition does not address the mechanism of protein ion formation, nor does it specify how the effects of La^{3+} differ from those of other metal ions.

Molecular dynamics (MD) simulations of charged droplets can provide atomistic insights into the ESI process. We and others have used this approach to explore the behavior of different analytes under a range of conditions.^{10,34,59-66} Those MD studies support the view that the CRM is the dominant ion formation mechanism during native ESI.^{8-10,33,64} The chain ejection model (CEM) describes the protein behavior under denaturing conditions.^{10,14,67}

The purpose of the current work was twofold. (1) By combining experiments and MD simulations we aimed to uncover the mechanism by which La^{3+} affects protein charge states. (2) More generally, we wanted to ascertain if currently available ESI simulation strategies have advanced to the point where even relatively subtle effects, such as La^{3+} -induced charge enhancement can be probed. Gratifyingly, our MD data mirrored the experimentally observed shifts to higher ESI charge states. Charge state enhancement was found to result from multidentate contacts that trap La^{3+} on the protein surface long before proteins are released into the gas phase.

2.2 Methods

2.2.1 Native ESI-MS and IMS

Equine holo-myoglobin (hMb) and bovine ubiquitin (Ubq) were purchased from Sigma (St. Louis, MO). 5 μ M aqueous protein solutions at pH 7 were prepared in 10 mM ammonium acetate or in 1 mM of either NaCl, CaCl₂, or LaCl₃. Data were acquired on a Synapt G2-Si quadrupole time-of-flight mass spectrometer (Waters, Milford, MA). Protein solutions were infused at 5 μ L min⁻¹. The ESI source was operated at +2.8 kV. Gentle conditions were used to minimize structural perturbations (sample cone voltage 5 V, source temperature 25 °C, desolvation temperature 40 °C), resulting in instrument operation close to the transmission threshold. Average charge states were calculated as $z_{av} = \sum(z_i I_i) / \sum I_i$ from three spectra for each salt condition. The intensities I_i in this equation included all adducts for any given charge state z_i . For IMS, the same source parameters were used, with Triwave enabled (trap DC entrance 1 V, trap DC bias 15 V, Trap DC -2 V, trap DC exit 0 V, IMS DC entrance 6.7 V, He cell DC 10 V, He exit -5 V, IMS bias 3 V, IMS DC exit 0 V, transfer DC entrance 1 V, transfer DC exit 1 V, trap wave velocity 100 m s⁻¹, trap wave height 1 V, IMS wave velocity 300 m s⁻¹, IMS wave height 6.5 V, transfer wave velocity 247 m s⁻¹, transfer wave height 4 V). Drift times were converted to effective He collision cross sections (Ω) using a mix of denatured proteins as calibrant ions.⁶⁸

2.2.2 MD Simulations

ESI droplets were simulated following previously described methods.¹⁰ Briefly, Gromacs 2018⁶⁹ was used with the CHARMM36 force field⁷⁰ and TIP4P-2005 water⁷¹ for modeling the temporal evolution of aqueous droplets with an initial radius of 5 nm (~16,000 water molecules) in vacuum. The protein was initially placed at the droplet center, using the crystal structures 1wla and 1ubq as starting conformations. All titratable sites were in their default states, i.e., N-terminus⁺, Arg⁺, Lys⁺, His⁰, Asp⁻, Glu⁻, C-terminus⁻, heme²⁻, resulting in an intrinsic charge of 2- for hMb and zero for Ubq. Various combinations of Na⁺, Ca²⁺, and La³⁺ ions were inserted in random positions to ensure an initial droplet charge close to the Rayleigh charge of 40+ (actual values ranged from 38+ to 41+). Tests were performed

to ensure the proper parametrization of metal ions (Figure 2.1).⁷² Following energy minimization and equilibration, MD runs were performed for 100 ns at 370 K, followed by 100 ns at 450 K to speed up the final solvent evaporation events. ESI charge states were determined by tallying the total metal ion and protein charge values after complete desolvation. Runs for each condition were repeated at least three times with different initial velocities and metal ion starting positions. The Ω values of MD-generated conformers were calculated using Collidoscope,⁷³ after running the desolvated proteins for an additional 500 ns in vacuum at 320 K.

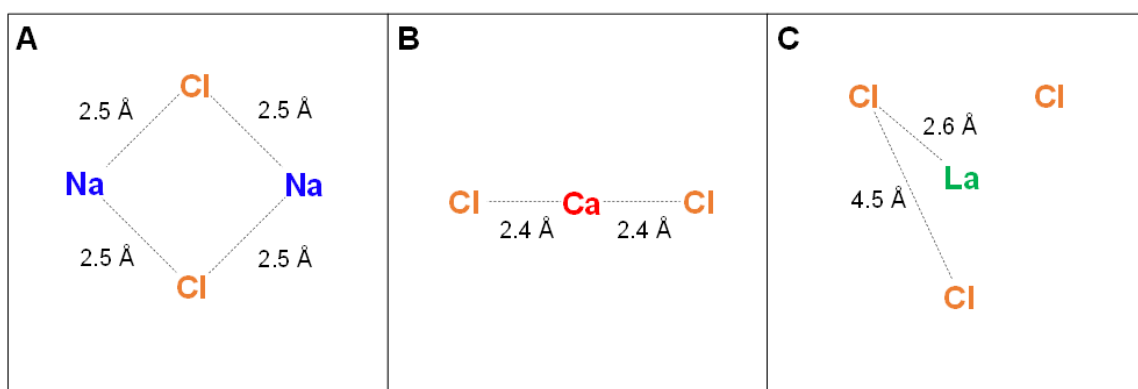


Figure 2.1 Testing the force field parametrization of Na^+ , Ca^{2+} , and La^{3+} . The three panels show MD-derived geometries for metal chloride assemblies. Each system was equilibrated at 300 K for 10 ns, then the temperature was lowered to 10 K and center-to-center distances were determined (indicated as dashed lines). These distances compare favorably with density functional theory (DFT) results, supporting the validity of the force field parameters used here. DFT distances for metal-Cl are 2.462 Å for NaCl,⁷⁴ 2.540 Å for CaCl₂,⁷⁵ and 2.589 Å (La-Cl) and 4.409 Å (Cl-Cl) for LaCl₃.⁷⁶ Lennard-Jones parameters for Na^+ , Ca^{2+} , and Cl were adopted from the Gromacs implementation of the CHARMM36 force field. Parameters for La^{3+} were taken from literature,⁷² i.e., $R_{\text{min}}/2 = 0.19$ nm and $\epsilon = 0.2092$ kJ mol⁻¹, when expressing the Lennard-Jones potential as $V(r) = \epsilon[(R_{\text{min}}/r)^{12} - 2(R_{\text{min}}/r)^6]$.

2.3 Results and Discussion

2.3.1 Native ESI-MS

Holo-myoglobin (hMb) and ubiquitin (Ubq) served as test proteins for the current work. Both have a globular native structure with a hydrophobic core, while most charged and hydrophilic side chains are solvent exposed.^{77,78} ESI was performed in neutral aqueous solutions. Mass spectra were initially recorded under typical native ESI conditions (10 mM ammonium acetate),⁹ producing $[M + zH]^{z+}$ charge state distributions with maxima at 9+ and 6+ for hMb and Ubq, respectively (Figure 2.2A/F). The salt concentration for subsequent experiments was lowered to 1 mM to avoid excessive peak broadening. Compared to the ammonium acetate data, the presence of LaCl_3 shifted the spectral maxima to significantly higher charge states, i.e., 9+ \rightarrow 11+ for hMb, and 6+ \rightarrow 8+ for Ubq (Figure 2.2D/I). These observations are consistent with the literature.⁴⁶

Trivalent ions such as La^{3+} are not normally encountered in biological solutions. To test the effects of more common metals we also studied the effects of a monovalent (Na^+) and a divalent (Ca^{2+}) species. Charge state distributions in the presence of 1 mM NaCl were quite similar to those in ammonium acetate, although NaCl caused a slight charge enhancement for Ubq (Figure 2.2B/G). CaCl_2 resulted in notable shifts to higher charge states for both proteins (Figure 2.2C/H), but not as large as those seen for LaCl_3 (Figure 2.2D/I). Protein ions formed in the presence of all three metal salts showed extensive metal adduction.

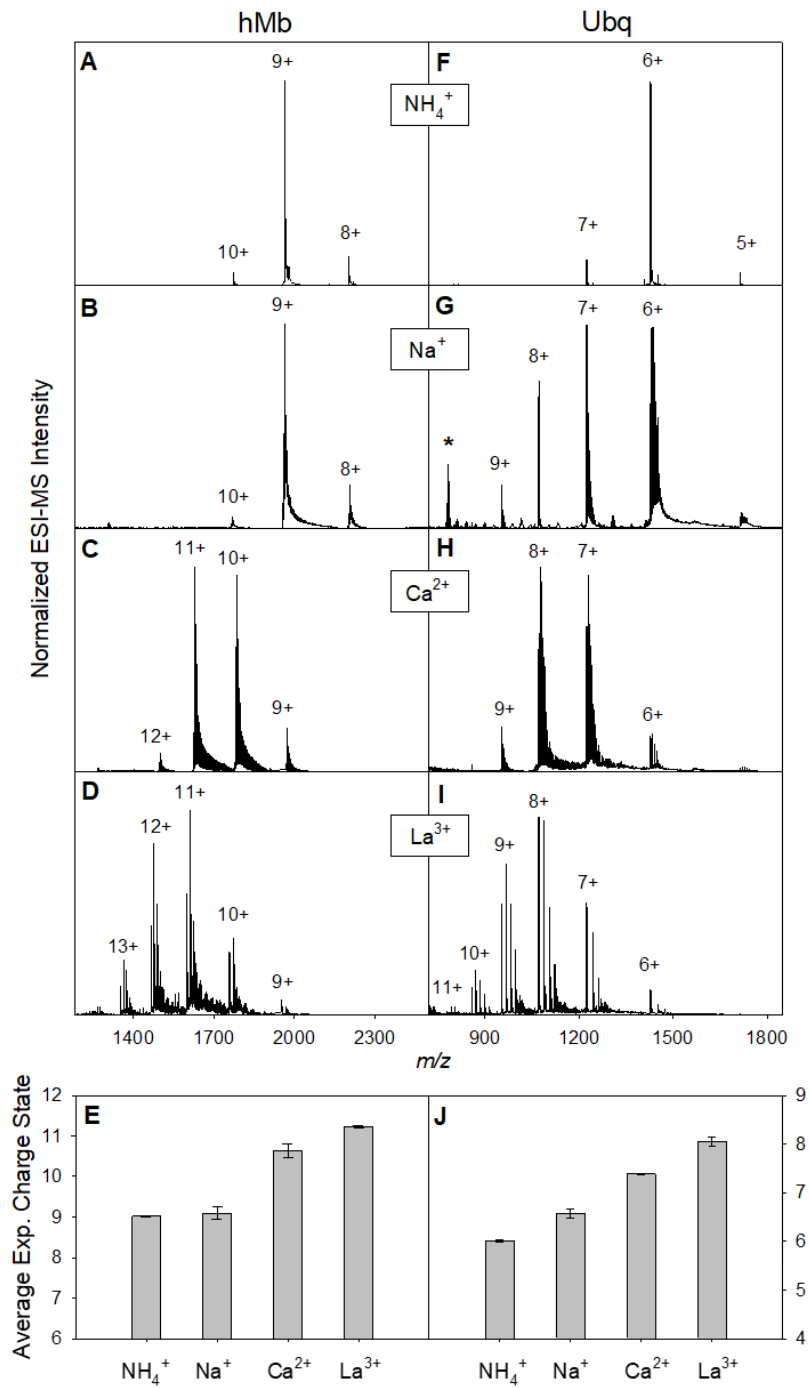


Figure 2.2 Experimental ESI mass spectra of (A-E) hMb and (F-J) Ubq at pH 7 recorded in (A/F) 10 mM ammonium acetate, (B/G) 1 mM NaCl, (C/H) 1 mM CaCl₂, and (D/I) 1 mM LaCl₃. Panels E/J display average protein charge states, error bars represent standard deviations from three independent measurements. The asterisk in panel G at m/z 782 refers to a NaCl cluster.

The bar diagrams in Figure 2.2 summarize the metal-induced charge state shifts, reiterating that protein charge states increase in the order $\text{NH}_4^+ \approx \text{Na}^+ < \text{Ca}^{2+} < \text{La}^{3+}$ (Figure 2.2E/J). The metals used here have similar ionic radii (1.02 / 1.00 / 1.03 Å for Na^+ / Ca^{2+} / La^{3+}).⁷⁹ Thus, there is a clear correlation between the charge of the metals and their capability to enhance protein ESI charge states, with La^{3+} being most effective. The following discussion focuses primarily on a comparison between Na^+ and La^{3+} , because these metals show the largest differences (Figure 2.2). Very similar mechanistic considerations apply to La^{3+} and Ca^{2+} , with the caveat that La^{3+} causes larger effects because of its higher charge.

2.3.2 Charge Carriers for Droplet Simulations

MD simulations were performed to obtain insights into the ESI mechanism in the presence of different metal ions. Consistent with previous work,^{8-10,31-34,64-66} all simulated droplets were initially charged to the Rayleigh limit, which is 40+ for the 5 nm droplet radius used here. This size range matches the droplets present towards the end of the evaporation/fission events in the ESI plume.⁹ Before examining simulation results, it is necessary to discuss how this 40+ droplet charge was implemented in the MD runs.

The net charge of experimental ESI droplets arises from various charge carriers. Protons are a key contributor; these are formed by redox processes within the ESI emitter (e.g., $2\text{H}_2\text{O} \rightarrow 4\text{H}^+ + \text{O}_2 + 4\text{e}^-$).⁸⁰ Metal ions play a major role as well, especially for solutions spiked with salts as in the current work.⁹ Even in the absence of added salts, Na^+ is usually present as a ubiquitous contaminant in biological samples.^{9,81}

The use of protons in MD simulations is challenging because H^+ Grotthuss shuttling cannot be described by classical force fields.⁸² Previous ESI simulations sidestepped this difficulty by substituting H^+ for Na^+ , culminating in the formation of $[\text{M} + z\text{Na}]^{z+}$ instead of $[\text{M} + z\text{H}]^{z+}$ ions.¹⁰ Here we pursued an analogous strategy. LaCl_3 experiments produced $[\text{M} + z\text{H} + n(\text{La}-3\text{H})]^{z+}$ ions (Figure 2.2). For MD runs we emulated this scenario using a combination of Na^+ and La^{3+} , such that the simulations produced $[\text{M} + z\text{Na} + n(\text{La}-3\text{Na})]^{z+}$ ions.

The 40+ droplet charge can be implemented by various $\text{La}^{3+}/\text{Na}^+$ combinations. Choosing the most suitable ratio *a priori* is difficult. We thus performed MD runs under various conditions, using droplets charged with 0%, 33%, 50%, 66%, and 100% La^{3+} . In all cases the remainder was supplied by Na^+ to ensure a total droplet charge of $\sim 40+$. The integer nature of charge dictates that these percentages are somewhat approximate, e.g., for 50% La^{3+} we used 7 La^{3+} and 19 Na^+ . Analogously, Ca^{2+} containing runs used different $\text{Ca}^{2+}/\text{Na}^+$ ratios.

2.3.3 Charge States of MD-Generated Protein Ions

ESI simulations produced gaseous protein ions charged by metal adduction. Droplets containing only Na^+ generated charge states 9+ for hMb and 6+ for Ubq (Figure 2.3). These simulation results agree well with experimental spectra recorded in the presence of NaCl or ammonium acetate (blue horizontal lines in Figure 2.3). The same results were reported previously for simulations on smaller droplets (3 nm instead of 5 nm radius¹⁰), attesting to the robustness of the MD strategy used here.

Simulations conducted with increasing $\text{La}^{3+}/\text{Na}^+$ ratios produced significantly higher charge states. For hMb droplets containing 100% La^{3+} this shift was from 9+ to 19+ (Figure 2.3A). Similarly, Ubq showed a shift from 6+ to 14+ (Figure 2.3C). Droplets containing a mix of La^{3+} and Na^+ predominantly resulted in La^{3+} adduction. Mixed $\text{Na}^+/\text{La}^{3+}$ bound protein ions were prevalent only for droplets with low (33%) La^{3+} content (Figure 2.3). Analogous considerations apply to droplets charged with $\text{Ca}^{2+}/\text{Na}^+$ (Figure 2.3B/D, Figure 2.4B/D).

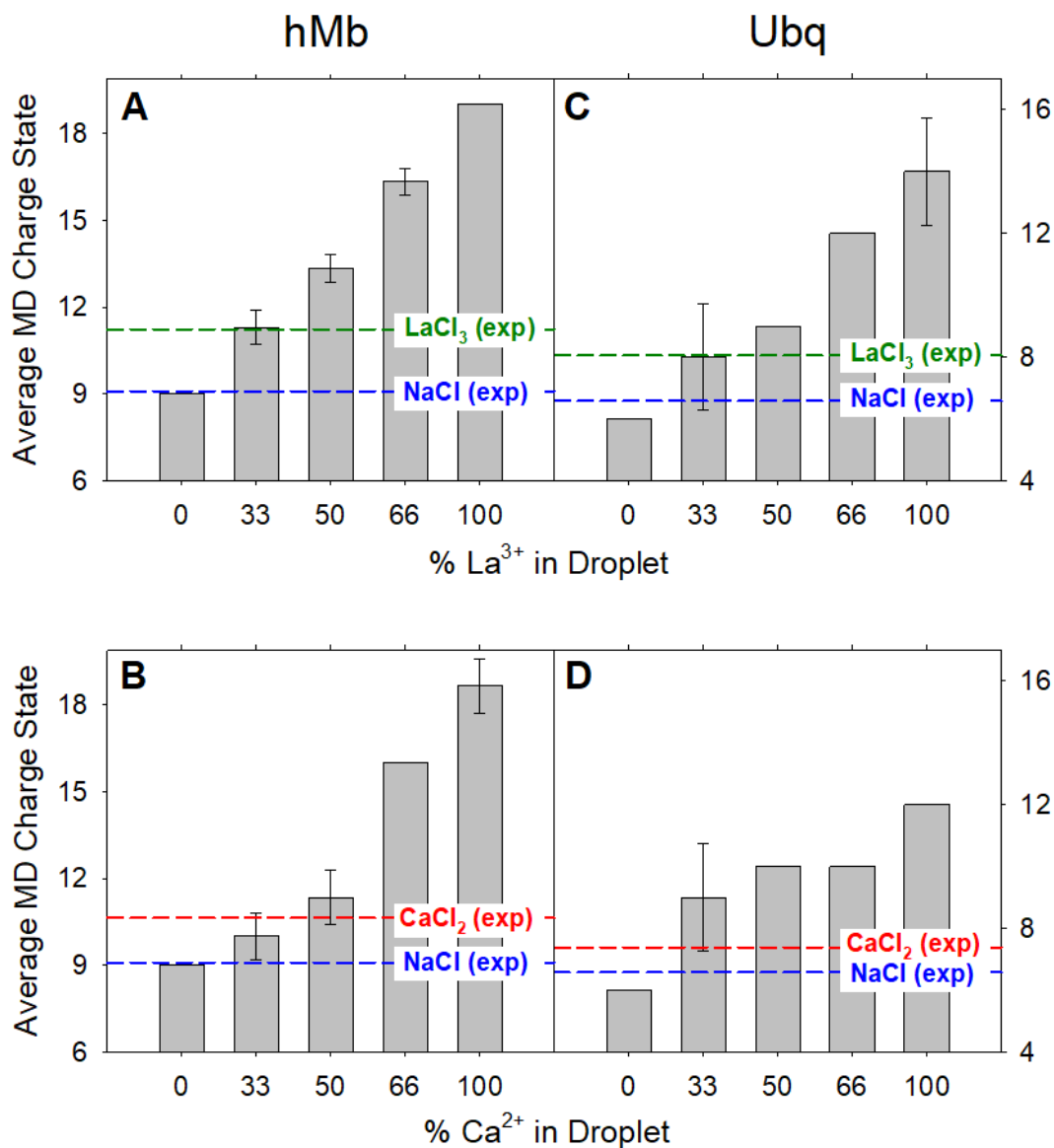


Figure 2.3 MD-simulated ESI charge states for (A/B) hMb and (C/D) Ubq. Top panels are for droplets containing La³⁺ and Na⁺; the contribution of La³⁺ to the initial ~40+ droplet charge is indicated (0% La³⁺ = 100% Na⁺). Bottom panels show the corresponding results for Ca²⁺/Na⁺ charged droplets. Error bars represent the standard deviation of three repeat runs. The absence of error bars refers to conditions that consistently yielded the same charge state. Dashed vertical lines indicate experimental average charge states measured in NaCl, CaCl₂, or LaCl₃ (from Figure 2.2).

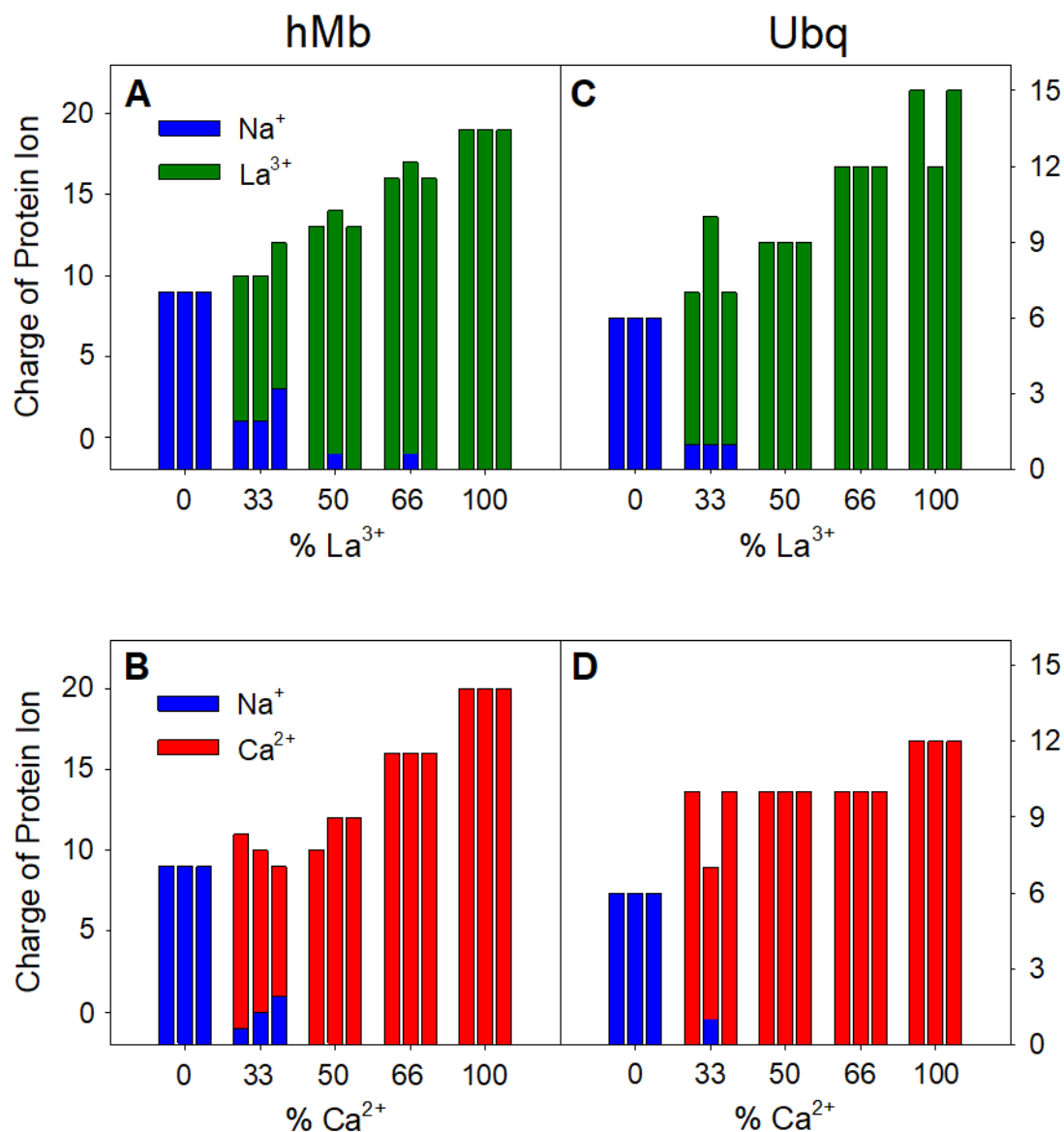


Figure 2.4 Contributions of different metal ions to the total protein charge after droplet evaporation to dryness. Each bar represents the result of one MD simulation. (A) hMb in the presence of Na⁺ and La³⁺, (B) hMb in the presence of Na⁺ and Ca²⁺, (C) Ubq in the presence of Na⁺ and La³⁺, (D) Ubq in the presence of Na⁺ and Ca²⁺. X-axes represent the contribution of La³⁺ (or Ca²⁺) to the 40+ initial droplet charge, the remainder of the droplet charge was supplied by Na⁺. Y-axes in panels A, B are offset by two charge units to account for the intrinsic 2- charge of hMb. For Ubq there is no offset, because the intrinsic protein charge is zero.

It is remarkable that our MD data reproduced the experimentally observed trend, where the presence of La^{3+} (or Ca^{2+}) increased the ESI charge states of proteins. Simulations conducted with 33% and 50% La^{3+} (or Ca^{2+}) provided the best match with the experimentally observed range of charge states (Figure 1, green/red horizontal lines in Figure 2.3). This finding suggests that ESI droplets under the experimental conditions of Figure 1 have a net charge that is approximately 33% to 50% due to La^{3+} (or Ca^{2+}), the remainder being contributed by other charge carriers.

2.3.4 Anatomy of the ESI Process

Typical MD snapshots for hMb in a Na^+ charged droplet (0% La^{3+}) are shown in Figure 2.5A. The droplet underwent shrinkage due to water evaporation, with occasional ejection of solvated Na^+ . These charge loss events are consistent with the ion evaporation model (IEM).^{9,10,83-85} The protein stayed within the droplet, reflecting the tendency of solvent exposed charged/hydrophilic side chains to remain solvated.⁷⁷ During the final stages of water evaporation the remaining Na^+ underwent binding to the protein. Ultimately, water evaporation to dryness generated gaseous hMb⁹⁺ (final frame in Figure 2.5A).

ESI events for a droplet charged with 50% La^{3+} are exemplified in Figure 2.5B, keeping in mind that simulations under these conditions produced charge states consistent with our experiments. Evaporative droplet shrinkage in Figure 2.5B was accompanied by IEM events for both La^{3+} and Na^+ . Evaporation to dryness culminated in gaseous hMb bound to five La^{3+} . Considering the intrinsic 2- charge of hMb, the charge state of this gaseous protein ion is 13+. Very similar ESI events were observed for Ubq (Figure 2.6). Additional details such as water and charge loss kinetics are compiled in Figures 2.7 and 2.8.

In summary, for the simulations of this work protein ions were released by solvent evaporation to dryness, i.e., ESI followed a CRM scenario.^{8-10,33} The shrinking droplets underwent IEM ejection of charge carriers (Na^+ , Ca^{2+} , La^{3+}), in line with previous reports.^{10,86,87} Other scenarios such as protein release via the CEM were not observed, consistent with the view that the CEM is operative only for unfolded conformers^{10,14,67}

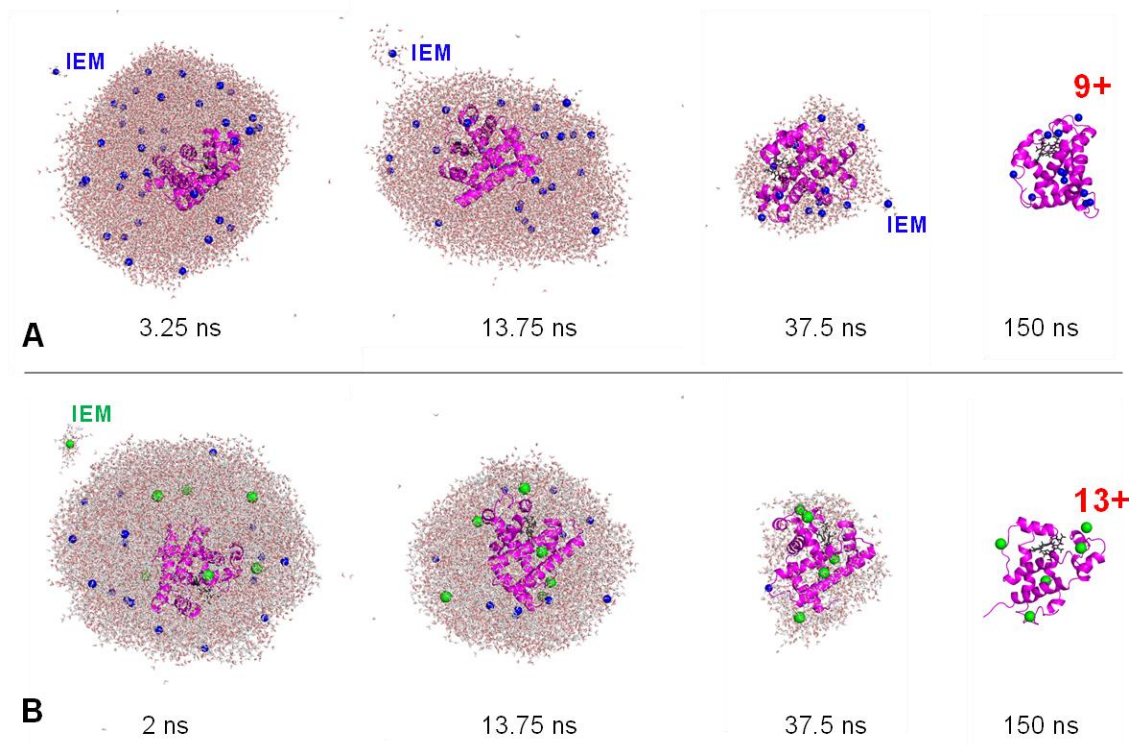


Figure 2.5 MD simulation snapshots of aqueous ESI droplets containing hMb. Initial droplet charge and diameter were $\sim 40+$ and ~ 5 nm. (A) Droplet charged with Na⁺ (0% La³⁺). (B) Droplet charged with La³⁺ and Na⁺ (50% La³⁺). Coloring is as follows – protein: magenta; Na⁺: blue; La³⁺: green. Field emission events for Na⁺ or La³⁺ are marked as “IEM”. Charge states of the gaseous protein ions released upon droplet evaporation to dryness are shown in red.

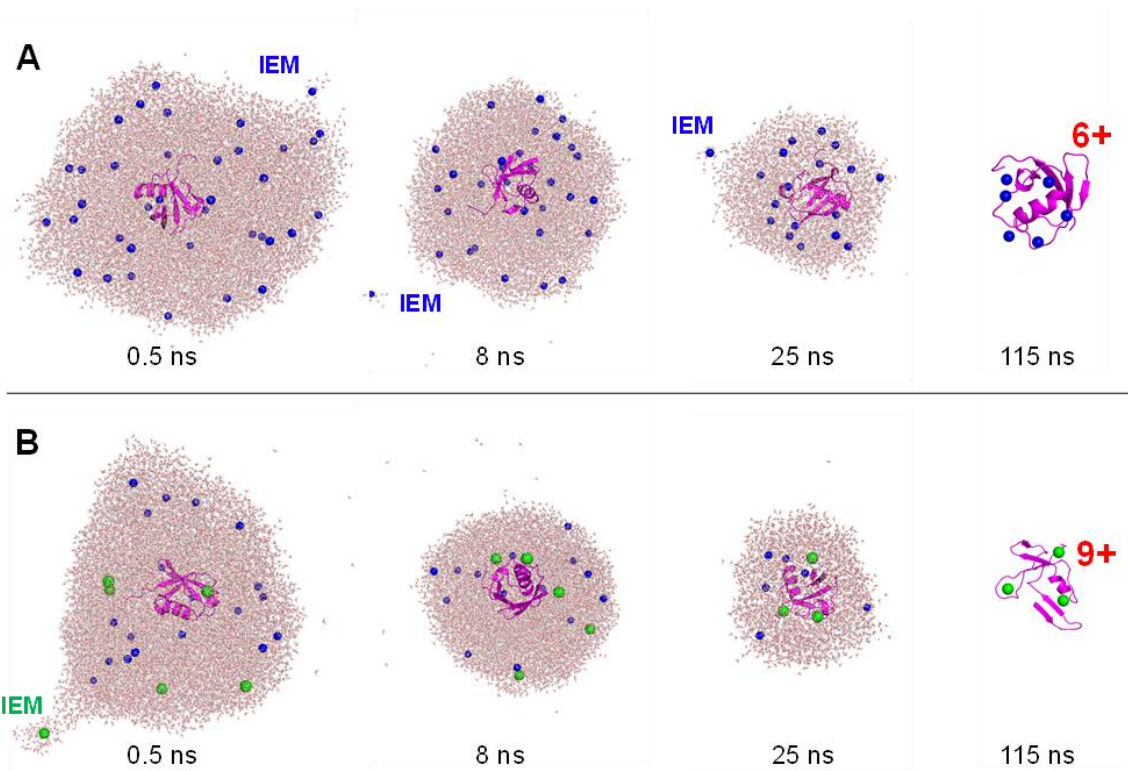


Figure 2.6 MD simulation snapshots of aqueous ESI droplets containing Ubq. The initial droplet charge was 40+. (A) Droplet charged with Na⁺ (0% La³⁺). (B) Droplet charged with La³⁺ and Na⁺ (50% La³⁺). Protein: magenta; Na⁺: blue; La³⁺: green. Field emission events for Na⁺ or La³⁺ are marked as “IEM”. Charge states of the gaseous protein ions released via droplet evaporation to dryness are shown in red.

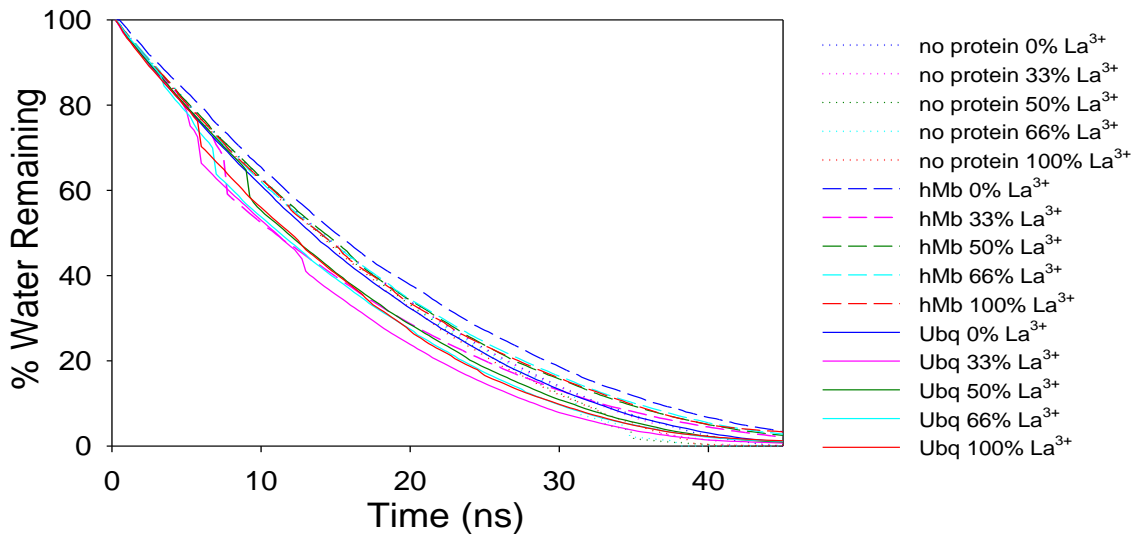


Figure 2.7 MD simulation data, displaying the number of water molecules in evaporating aqueous droplets. For all runs the initial droplet radius was ~ 5 nm, with a $\sim 40+$ net charge and a total of $\sim 16,000$ water molecules. The droplets contained various $\text{La}^{3+}/\text{Na}^{+}$ ratios as noted in the figure legend and explained in the main text. Three types of droplets were studied, without protein, with hMb, and with Ubq. The data shown here illustrate that the water evaporation kinetics are very similar for the different $\text{La}^{3+}/\text{Na}^{+}$ ratios, and largely independent of the presence of protein. Each curve represents the average of three runs.

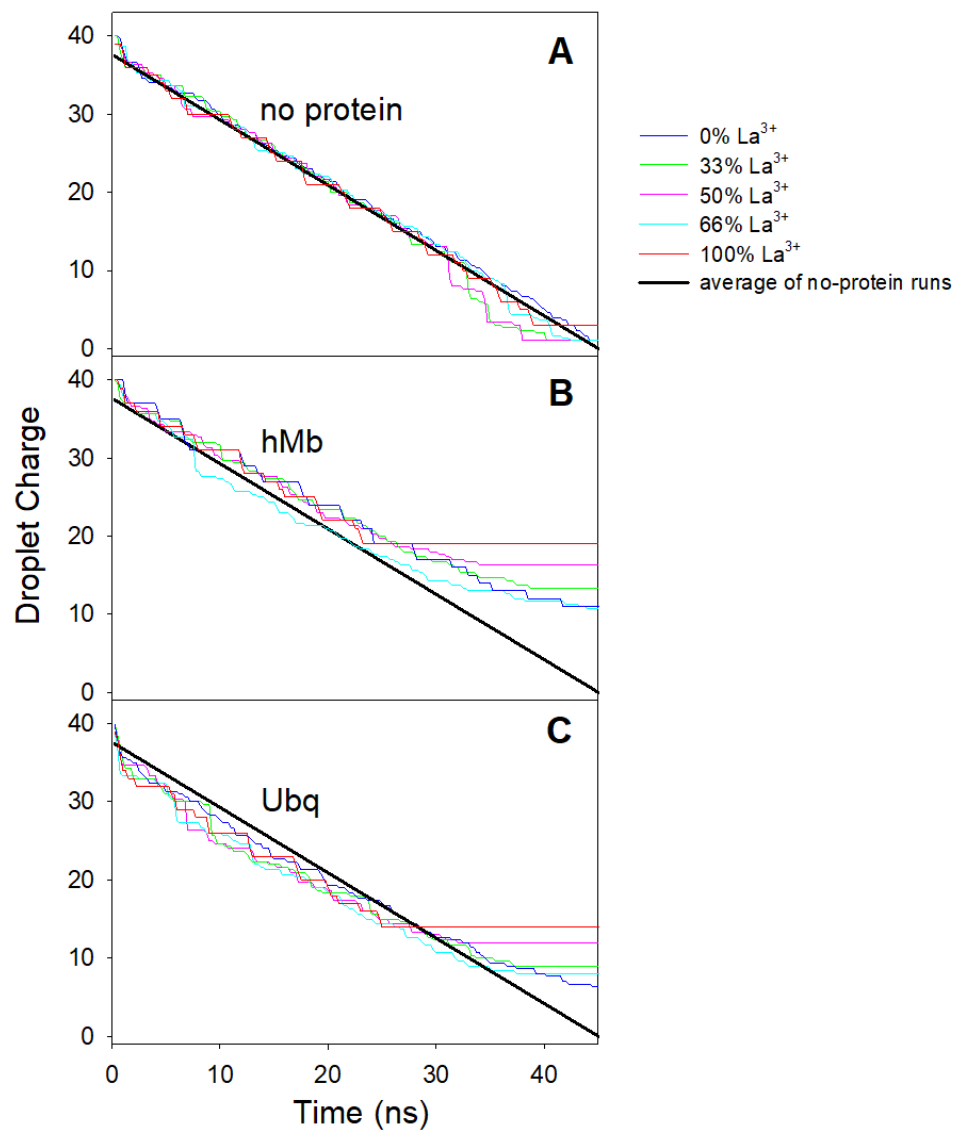


Figure 2.8 MD simulation data, displaying the charge on evaporating aqueous droplets as a function of time. The initial droplet radius was ~ 5 nm and the initial charge was $\sim 40+$. The droplets contained various $\text{La}^{3+}/\text{Na}^+$ ratios as noted in the legend and explained in the main text. (A) Droplets without protein. The solid line represents a linear regression that captures the average charge loss kinetics for this droplet type. (B) hMb containing droplets. (C) Ubq containing droplets. For reference, the regression line from panel A is reproduced in B and C. The data shown here illustrate that the charge loss kinetics are very similar for the different $\text{La}^{3+}/\text{Na}^+$ ratios. Each colored line represents the average of three runs.

2.3.5 Mechanism of La^{3+} Enhanced Protein Charging

The reasons why La^{3+} enhances protein charge states starts to emerge from Figure 2.9, which tracks the droplet charge z_D relative to the Rayleigh charge $z_R = 8\pi/e \times (\epsilon_0 \gamma r^3)^{1/2}$, where γ = surface tension, ϵ_0 = vacuum permittivity, and e = elementary charge.⁹ The droplet radius r was calculated by assuming spherical shape and a density of 1 g cm^{-3} .⁸ The z_D/z_R profiles in Figure 2.9 start off in zigzag patterns, reflecting the alternation between solvent evaporation at constant z_D (which gradually increases z_D/z_R), and IEM ejection of a metal ion (causing a sudden drop of z_D/z_R)¹⁰ These events occurred in a fairly narrow z_D/z_R interval between ~ 0.75 and 1, consistent with studies on other droplets.^{8-10,31,32}

Na^+ charged droplets (0% La^{3+}) underwent IEM events until late during the evaporation process ($t \approx 50 \text{ ns}$, red lines in Figure 2.9A/D). In contrast, the presence of La^{3+} caused IEM events to terminate much earlier, i.e., $t \approx 38 \text{ ns}$ for 50% La^{3+} and $t \approx 24 \text{ ns}$ for 100% La^{3+} (red lines in Figure 2.9B/C/E/F). Continuing water evaporation after these final IEM events caused the La^{3+} droplets to enter a regime where $z_D/z_R > 1$. This effect was most pronounced for 100% La^{3+} , where the profiles approached $z_D/z_R \approx 2$ at the end of the process (Figure 2.9C/F).

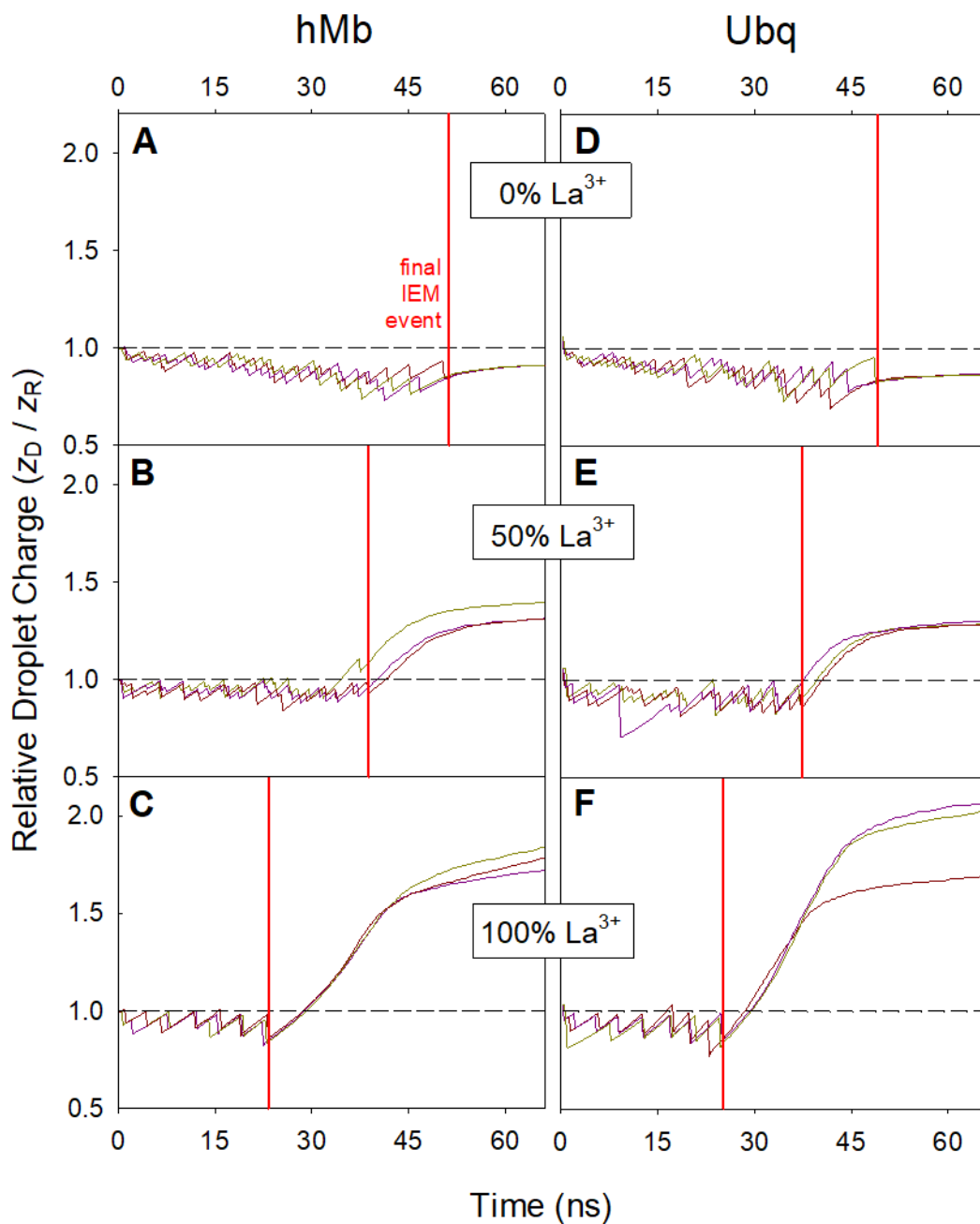


Figure 2.9 MD data for ESI droplets containing (A-C) hMb or (D-F) Ubq displaying the ratio of droplet charge z_D to the Rayleigh charge z_R . The initial value of z_D was $\sim 40+$ due to the presence of Na^+ and La^{3+} ions, with a La^{3+} charge contribution of (A/D) 0%, (B/E) 50%, and (C/F) 100%. Each panel contains data for three runs. Horizontal dashed lines at $z_D/z_R = 1$ represent the Rayleigh limit. Vertical red lines indicate the time point where the final IEM event occurs.

Why do La^{3+} droplets venture into a $z_D/z_R > 1$ regime towards the end of the evaporation process? The answer becomes clear when tracking the metal ion positions within the droplets. We will first discuss hMb droplets charged with Na^+ (0% La^{3+} , Figure 2.10A) and 100% La^{3+} (Figure 2.10B). Figure 2.10A shows that all Na^+ diffuse freely in the aqueous layer that surrounds the protein. This high mobility allows Na^+ to reach any location within the droplet, including surface positions from where IEM ejection can take place. Na^+ adduction to the protein occurs late, when the last water layers evaporate, generating the final $[\text{M} + z\text{Na}]^{z+}$ product at $t \approx 70$ ns. A different scenario applies to La^{3+} droplets (Figure 2.10B). La^{3+} adduction to the protein takes place very early, starting immediately after the onset of the MD runs. The protein attains its final $[\text{M} + z/3\text{La}]^{z+}$ charge state while it is still embedded in the droplet, at $t \approx 20$ ns. These irreversible binding events prevent the corresponding La^{3+} ions from undergoing IEM ejection. Data for Ubq revealed a very similar behavior (Figure 2.11).

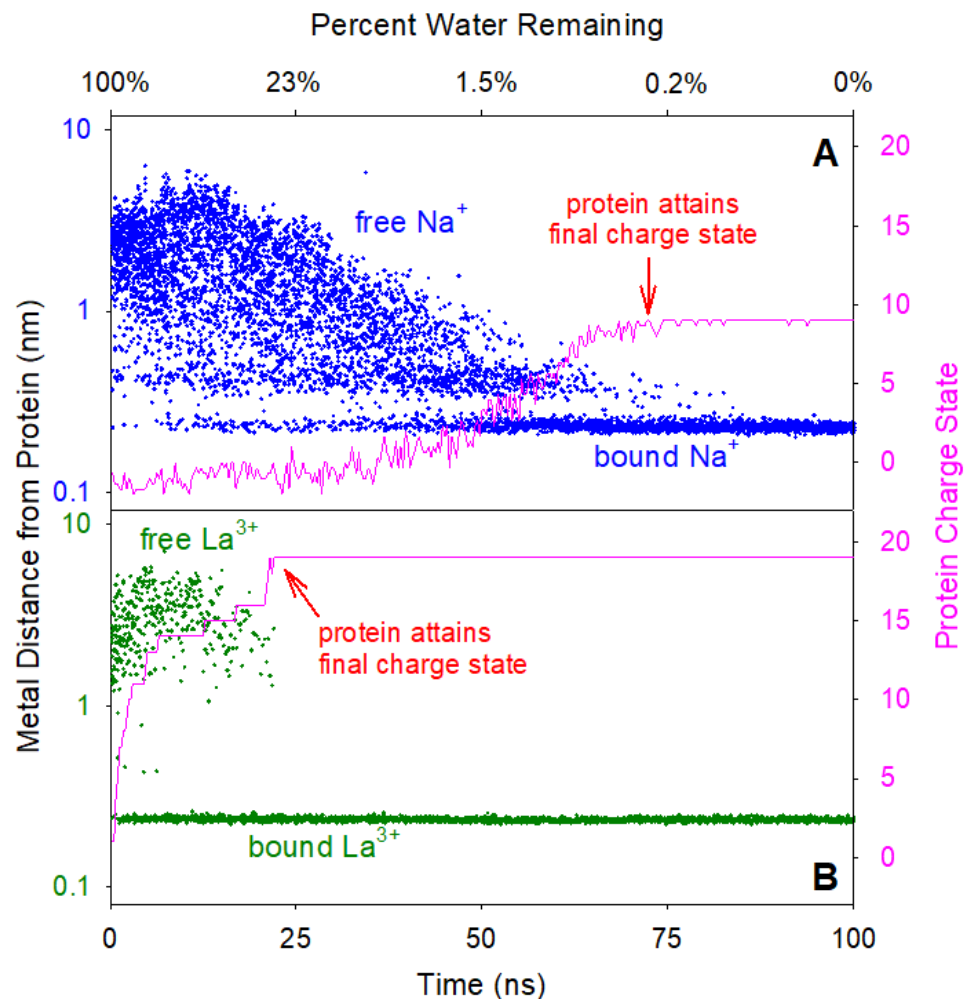


Figure 2.10 Binding of metal ions to hMb in evaporating aqueous droplets during MD runs. (A) Droplets charged with Na⁺ (0% La³⁺). (B) Droplets charged with 100% La³⁺. Point clouds represent the distance of individual metal ions from the closest protein heavy atom. Distances of less than 0.3 nm correspond to metal ions that are bound to the protein. Magenta profiles tally how the protein charge state changes due to metal ion binding. Distance points are for one representative simulation; protein charge states are averages of three runs.

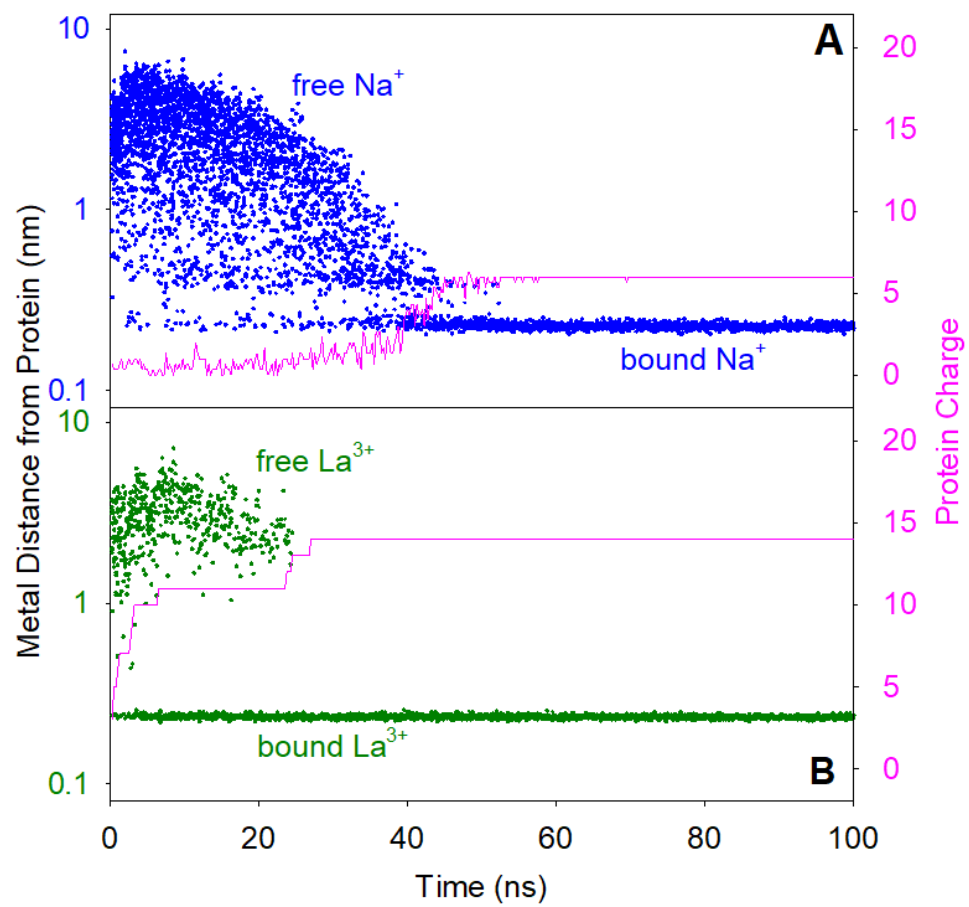


Figure 2.11 Same as in *Figure 2.10*, but for *Ubq*.

Why do La^{3+} and Na^+ show different adduction behavior? Figure 2.12A/B reveals that the high protein affinity of La^{3+} arises from multidentate contacts involving five or six charged/polar moieties per metal ion (Asp^- and Glu^- side chains, but also carbonyl oxygens in neutral side chains, plus main chain $\text{C}=\text{O}$ sites). The high stability of such chelation interactions involving multivalent metals is well established.¹ In contrast, Na^+ binding is much less extensive, with only two or three protein-metal contacts that result in a lower affinity to the protein surface (Figure 2.12C/D). The situation is analogous to metal interactions with chelators such as EDTA, which has an affinity of $10^{1.9}$ M for Na^+ , while the affinity for La^{3+} is $10^{15.4}$ M.⁸⁸

Effects analogous to those illustrated in Figure 2.10 were also seen for mixed $\text{La}^{3+}/\text{Na}^+$ droplets, i.e., early high affinity binding of La^{3+} enhanced the charge of the resulting protein ions. This includes MD runs for 33% La^{3+} and 50% La^{3+} that resulted in charge states consistent with our experiments (Figures 2.13/2.14). For these 33% La^{3+} and 50% La^{3+} droplets the z_D/z_R ratio increased to ~ 1.3 at the end of the evaporation process (Figure 2.9B/E), which is within a range that has been shown to be possible experimentally.³² In contrast, the $z_D/z_R \rightarrow 2$ behavior seen for 100% La^{3+} (Figure 2.9C/F) likely exceeds the range that can be expected under experimental conditions.^{8,10,31,32} We nonetheless chose to highlight the 100% La^{3+} data in Figure 2.10B because they most clearly illustrate the charge enhancement mechanism, without complications arising from the simultaneous presence of La^{3+} and Na^+ .

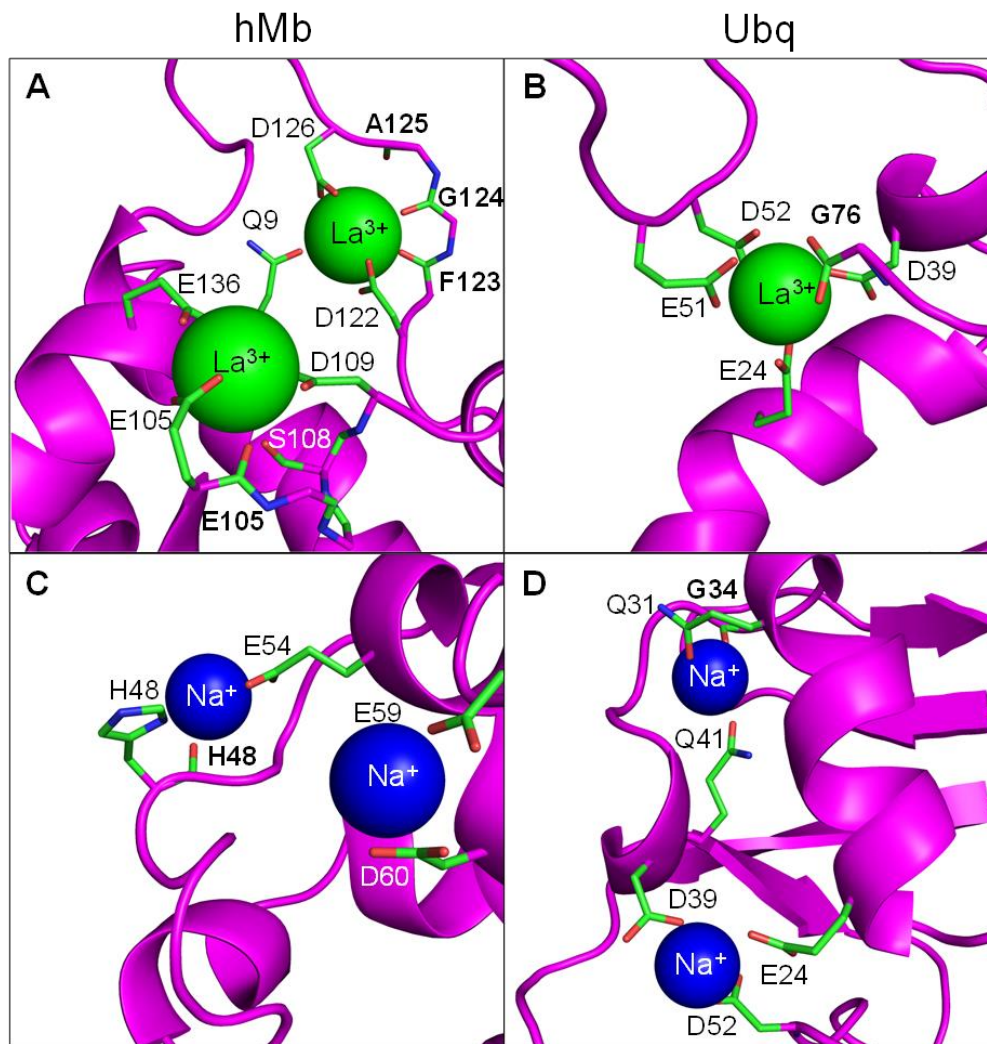


Figure 2.12 Protein- La^{3+} and protein- Na^{+} contacts seen upon solvent evaporation to dryness for (A/C) hMb and (B/D) Ubq. Side chains are identified using regular font, bold letters refer to main chain sites. Note that more protein sites are involved in binding each La^{3+} ion (green), compared to Na^{+} (blue).

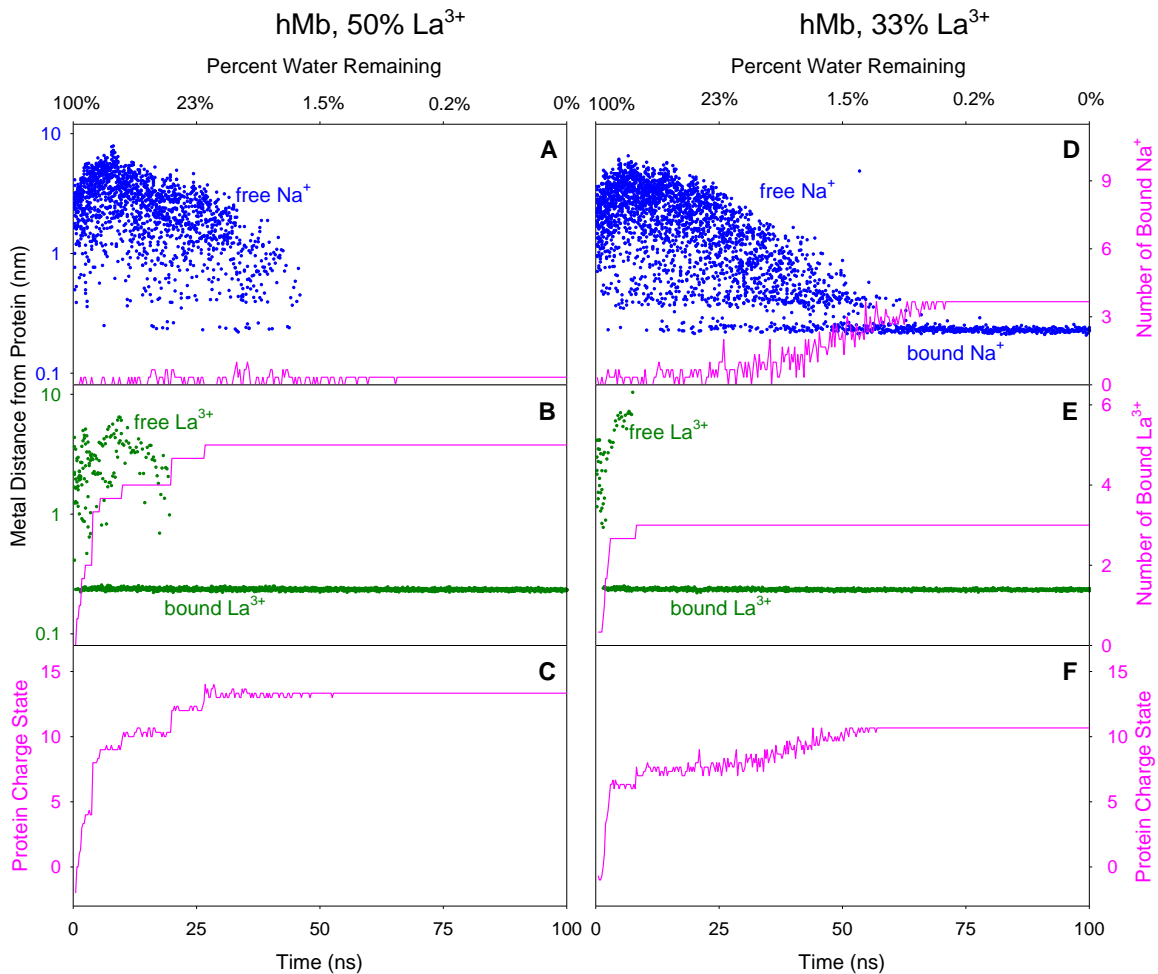


Figure 2.13 Binding of metal ions to hMb in evaporating aqueous droplets during MD runs. For the simulations shown here the droplets contained a mix of La^{3+} and Na^+ . (A-C) Droplets charged with (50% La^{3+}). (D-F) Droplets charged with 33% La^{3+} . Point clouds represent the distance of individual metal ions from the closest protein heavy atom. Distances of less than 0.3 nm correspond to metal ions that are bound to the protein. Panels C/F tally how the protein charge state changes due to metal ion binding. Distance points are for one representative simulation; all other profiles represent averages of three runs.

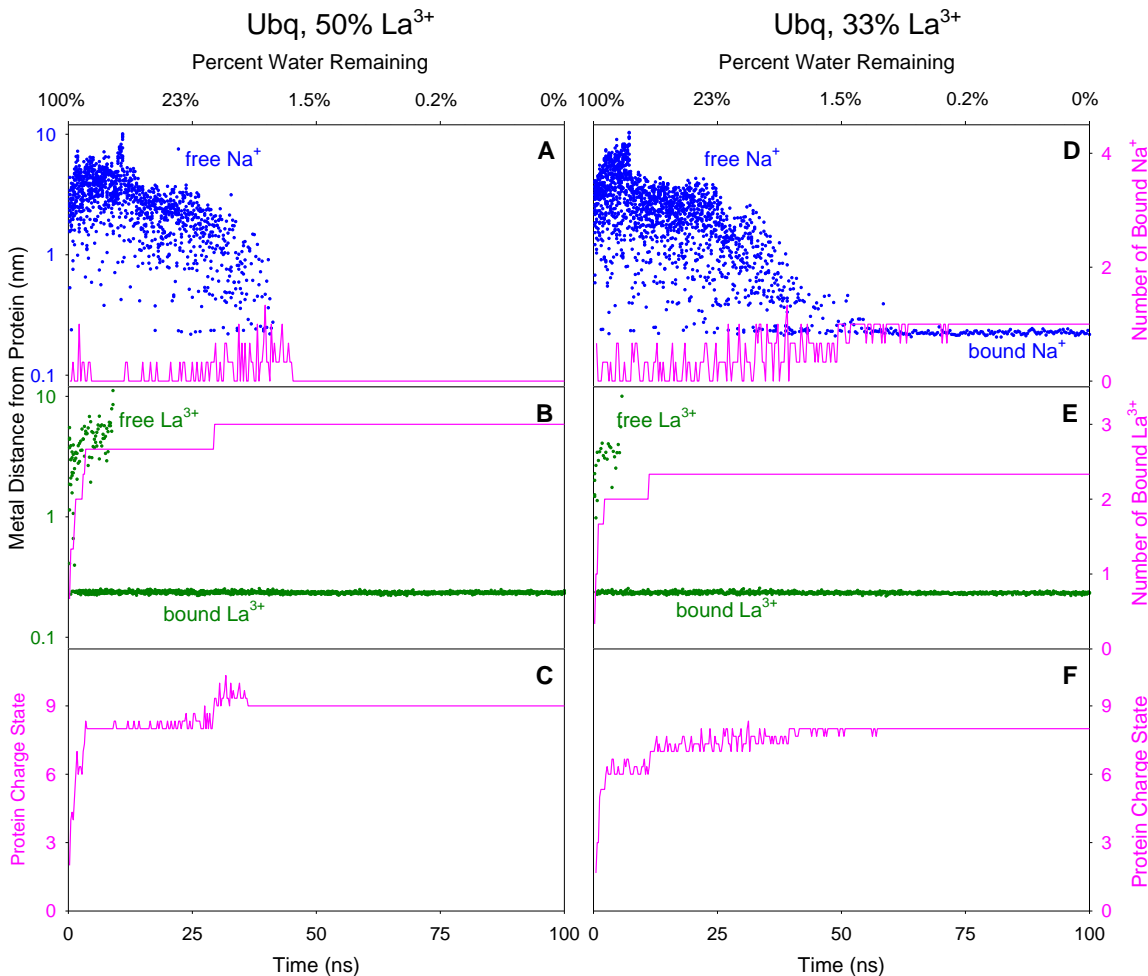


Figure 2.14 Same as in Figure 2.13, but for Ubq

In summary, Figure 2.10 uncovers the principle whereby La^{3+} enhances ESI charge states: La^{3+} has a very high affinity to the protein surface, causing early protein- La^{3+} binding within the ESI droplet. The irreversible nature of these interactions precludes IEM ejection of the bound La^{3+} from the droplet, culminating in the formation of charge-enhanced protein ions. The situation is different for droplets charged only with monovalent ions such as Na^+ , which remain mobile within the aqueous layer where they are subject to IEM ejection. Thus, proteins released by solvent evaporation to dryness carry less charge because Na^+ ejection is not impeded by premature protein-metal binding.

2.3.6 Gas Phase Conformations

IMS experiments revealed that La^{3+} mediated charge enhancement induced a gradual expansion of protein structure. Raising the hMb charge from 9+ to 13+ caused the experimental Ω to increase by 33%, while the 6+ \rightarrow 10+ transition of Ubq resulted in a 73% increase (Figure 2.15). These effects arise from the electrostatic repulsion within the protein ions.^{89,90} For comparing these observations with simulation results, MD-generated protein ions were allowed to evolve in vacuum for 500 ns. The resulting MD structures mirrored the experimental trend, *i.e.*, a charge state dependent expansion (Figure 2.15, 2.16). For hMb 9+ to 11+ and Ubq 6+ to 8+ the MD structures had Ω values that overlapped with the experimental distributions (vertical lines in Figure 2.15). This agreement suggests that the MD structures represent suitable candidates for the experimental gas phase ions in this charge state range. Multidentate protein- La^{3+} contacts somewhat limited the Coulombic expansion of the more highly charged protein ions (e.g. hMb¹³⁺, Ubq¹⁰⁺), in agreement with earlier MD data and experiments.^{45,91}

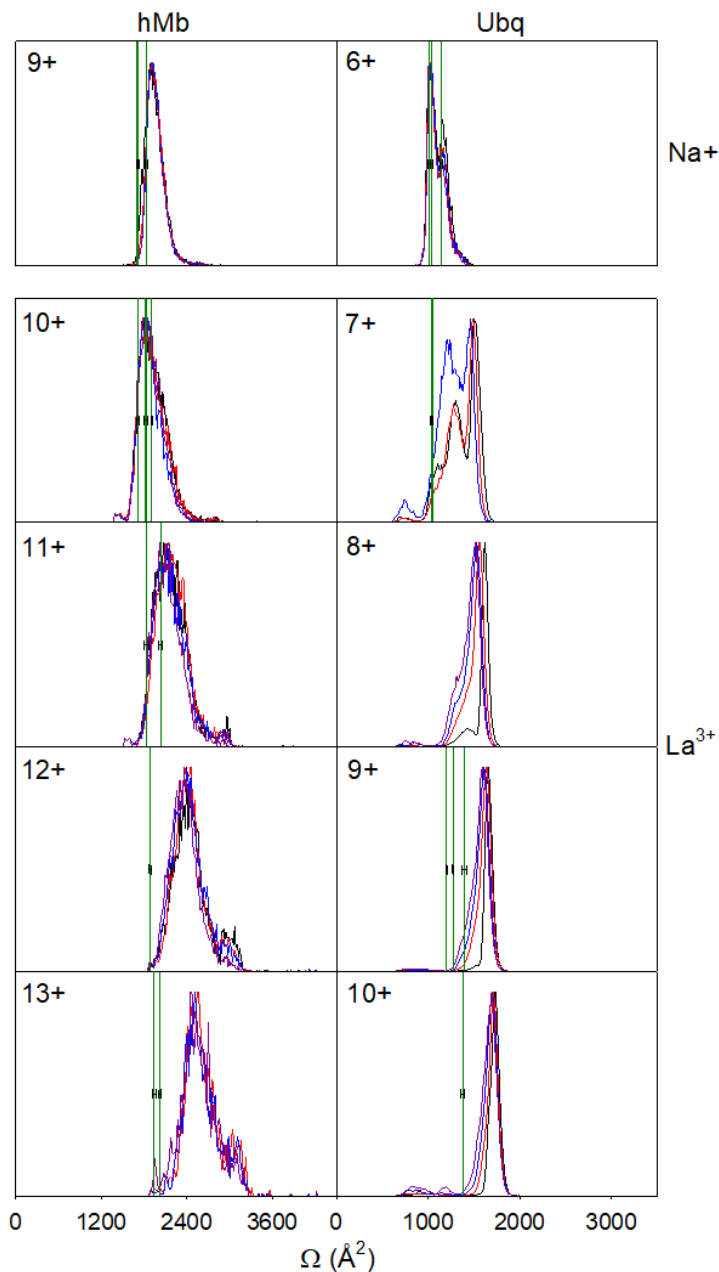


Figure 2.15 IMS data for hMb and Ubq electro sprayed in the presence of NaCl (top panels) and LaCl₃ (bottom panels). Each panel contains three or four Ω profiles that represent different adduction levels: black – no metal bound (protonated only); red – one metal ion bound; blue – two metal ions bound; purple – three metal ions bound. Vertical lines reflect average Ω collisions of MD generated gas phase structures, error bars represent standard deviations of the MD results extracted in 100 ns intervals, at $t = 100 \dots 500$ ns.

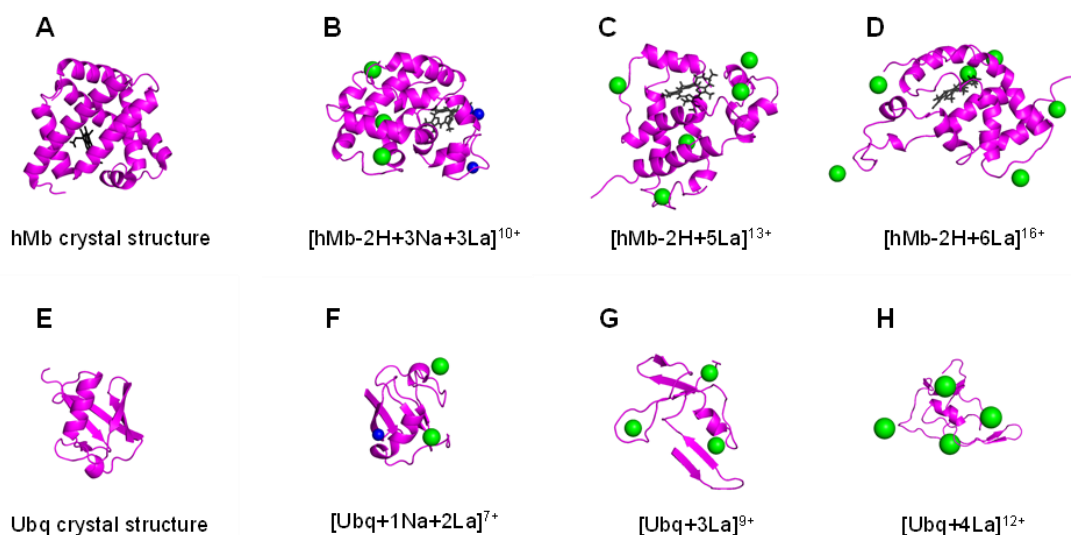


Figure 2.16 Comparison of crystal structure (A) and typical MD-generated gas phase structures of hMb in various charge states (B-D). Data for Ubq are shown in (E-H). Simulation conditions were 33% La³⁺ (B/F), 50% La³⁺ (C/G), and 66% La³⁺ (D/H). La³⁺ is shown in green, Na⁺ is blue, and heme²⁻ is black. Note how increasing the charge states causes a gradual breakdown of protein structure.

2.4 Conclusions

We employed MD simulations to explore the mechanism whereby multivalent metal ions such as La³⁺ enhance protein charge states when electrosprayed from non-denaturing aqueous solutions. Previous work referred to this effect as “supercharging”.⁴⁶ Here we avoided this term, because the ~20% charge enhancement caused by La³⁺ is quite subtle compared to the much larger shifts induced by organic supercharging agents.^{10,55–58}

Under the conditions studied here protein ions are released via the CRM which entails solvent evaporation to dryness (Figure 2.5). As already shown in earlier work,^{10,86,87} droplet shrinkage is accompanied by the IEM ejection of charge carriers which is driven by the electrostatic repulsion within the system (Figure 2.9).^{8–10,31,32} Each charge carrier can experience only one of two outcomes: (1) IEM ejection from the droplet, or (2) binding to the protein. Thus, any suppression of IEM events will enhance the charge of the dried-

out protein formed at the end of the process. Monovalent charge carriers (Na^+ , but also H^+_{aq} and NH_4^+)⁹ are highly soluble in water and roam freely in the aqueous phase surrounding the protein; there are no factors that interfere with IEM ejection of these species. Consequently, only relatively few of the monovalent charge carriers stay behind until the final solvent layers evaporate; binding of these residual ions to the protein generates low ESI charge states. In contrast, the trivalent nature of La^{3+} drives the formation of highly stable chelation contacts¹ with the protein early during the process, when the droplet still contains thousands of water molecules (Figure 2.10). Irreversible binding of multiple La^{3+} ions to the protein prevents the IEM ejection of these charge carriers. The resulting dried-out protein therefore carries more charge than for droplets that only contain monovalent ions.

The aforementioned mechanism of La^{3+} induced charge enhancement bears conceptual similarities to the “charge trapping model” that has been proposed for the way in which organic supercharging agents enhance protein charge states during native ESI.¹⁰ Both scenarios are rooted in a suppression of IEM events under CRM conditions. For organic supercharging agents this IEM suppression has been attributed to an ionophobic solvent layer surrounding the protein-containing droplet core.¹⁰ For the La^{3+} containing droplets studied here IEM events are suppressed by the high affinity of charge carriers to the protein surface.

The current work complements earlier MD simulation studies that have uncovered the mechanistic foundation of numerous ESI-related phenomena.^{10,34,59–66} It is remarkable that the relatively simple MD methods employed here are capable of reproducing features as intricate as the effects of different metal charge carriers. It is hoped that future computational and experimental advances will continue to provide new insights into the mechanisms by which biomolecular analytes are transferred from solution into the gas phase during ESI.

2.5 References

- 1 T. Dudev and C. Lim, *Chem. Rev.*, 2014, **114**, 538–556.
- 2 M. M. Yamashita, L. Wesson, G. Eisenman and D. Eisenberg, *Proc. Natl. Acad. Sci. U. S. A.*, 1990, **87**, 5648–5652.
- 3 A. T. Bozzi, L. B. Bane, W. A. Weihofen, A. L. McCabe, A. Singharoy, C. J. Chipot, K. Schulten and R. Gaudet, *Proc. Natl. Acad. Sci. U. S. A.*, 2016, **113**, 10310–10315.
- 4 G. F. Pirrone, R. E. Iacob and J. R. Engen, *Anal. Chem.*, 2015, **87**, 99–118.
- 5 V. L. Mendoza and R. W. Vachet, *Mass Spectrom. Rev.*, 2009, **28**, 785–815.
- 6 U. Kaur, D. T. Johnson, E. E. Chea, D. J. Deredge, J. A. Espino and L. M. Jones, *Anal. Chem.*, 2019, **91**, 142–155.
- 7 A. Sinz, C. Arlt, D. Chorev and M. Sharon, *Protein Sci.*, 2015, **24**, 1193–1209.
- 8 F. J. de la Mora, *Anal. Chim. Acta*, 2000, **406**, 93–104.
- 9 P. Kebarle and U. H. Verkerk, *Mass Spectrom. Rev.*, 2009, **28**, 898–917.
- 10 L. Konermann, H. Metwally, Q. Duez and I. Peters, *Analyst*, 2019, **144**, 6157–6171.
- 11 A. C. Leney and A. J. R. Heck, *J. Am. Soc. Mass Spectrom.*, 2017, **28**, 5–13.
- 12 A. Konijnenberg, A. Butterer and F. Sobott, *Biochim. Biophys. Acta, Proteins Proteomics*, 2013, **1834**, 1239–1256.
- 13 N. Khristenko, J. Amato, S. Livet, B. Pagano, A. Randazzo and V. Gabelica, *J. Am. Soc. Mass Spectrom.*, 2019, **30**, 1069–1081.
- 14 S. Mehmood, T. M. Allison and C. V Robinson, *Annu. Rev. Phys. Chem.*, 2015, **66**, 453–474.
- 15 E. N. Kitova, A. El-Hawiet, P. D. Schnier and J. S. Klassen, *J. Am. Soc. Mass Spectrom.*, 2012, **23**, 431–441.
- 16 J. L. P. Benesch and B. T. Ruotolo, *Curr. Opin. Struct. Biol.*, 2011, **21**, 641–649.
- 17 A. F. M. Gavriilidou, F. P. Holding, D. Mayer, J. E. Coyle, D. B. Veprintsev and R. Zenobi, *Biochemistry*, 2018, **57**, 1685–1689.
- 18 O. Fatunmbi, R. R. Abzalimov, S. N. Savinov, A. Gershenson and I. A. Kaltashov, *Biochemistry*, 2016, **55**, 1918–1928.
- 19 G. T. H. Nguyen, T. N. Tran, M. N. Podgorski, S. G. Bell, C. T. Supuran and W. A. Donald, *ACS Cent. Sci.*, 2019, **5**, 308–318.

- 20 P. Hu, Q.-Z. Ye and J. A. Loo, *Anal. Chem.*, 1994, **66**, 4190–4194.
- 21 T. T. Ngu and M. J. Stillman, *J. Am. Chem. Soc.*, 2006, **128**, 12473–12483.
- 22 S. H. Chen, L. X. Chen and D. H. Russell, *J. Am. Chem. Soc.*, 2014, **136**, 9499–9508.
- 23 Y. Yamazaki and T. Takao, *Anal. Chem.*, 2008, **80**, 8246–8252.
- 24 I. A. Kaltashov, C. E. Bobst, M. Zhang, R. Leverence and D. R. Gumerov, *Biochim. Biophys. Acta, Gen. Subj.*, 2012, **1820**, 417–426.
- 25 S. Ahmadi, S. L. Zhu, R. Sharma, D. J. Wilson and H. B. Kraatz, *J. Inorg. Biochem.*, 2019, **194**, 44–51.
- 26 J. T. S. Hopper, K. Sokratous and N. J. Oldham, *Anal. Biochem.*, 2012, **421**, 788–790.
- 27 W. Rist, P. M. Mayer, J. S. Andersen, P. Roepstorff and T. J. D. Jørgensen, *Anal. Biochem.*, 2005, **342**, 160–162.
- 28 J. Cavanagh, L. M. Benson, R. Thompson and S. Naylor, *Anal. Chem.*, 2003, **75**, 3281–3286.
- 29 N. Xu, Y. Lin, S. A. Hofstadler, D. Matson, C. J. Call and R. D. Smith, *Anal. Chem.*, 1998, **70**, 3553–3556.
- 30 R. Juraschek, T. Dulcks and M. Karas, *J. Am. Soc. Mass Spectrom.*, 1999, **10**, 300–308.
- 31 A. Gomez and K. Tang, *Phys. Fluids*, 1994, **6**, 404–414.
- 32 R. L. Grimm and J. L. Beauchamp, *J. Phys. Chem. A*, 2010, **114**, 1411–1419.
- 33 A. T. Iavarone and E. R. Williams, *J. Am. Chem. Soc.*, 2003, **125**, 2319–2327.
- 34 D. Kim, N. Wagner, K. Wooding, D. E. Clemmer and D. H. Russell, *J. Am. Chem. Soc.*, 2017, **139**, 2981–2988.
- 35 A. R. McKay, B. T. Ruotolo, L. L. Ilag and C. V Robinson, *J. Am. Chem. Soc.*, 2006, **128**, 11433–11442.
- 36 V. W.-M. Lee, H. Li, T.-C. Lau and K. W. M. Siu, *J. Am. Chem. Soc.*, 1998, **120**, 7302–7309.
- 37 A. A. Shvartsburg and R. C. Jones, *J. Am. Soc. Mass Spectrom.*, 2004, **15**, 406–408.
- 38 H. Liu and K. Hakansson, *J. Am. Soc. Mass Spectrom.*, 2006, **17**, 1731–1741.

- 39 X. F. Chen, Y. M. E. Fung, W. Y. K. Chan, P. S. Wong, H. S. Yeung and T. W. D. Chan, *J. Am. Soc. Mass Spectrom.*, 2011, **22**, 2232–2245.
- 40 J. A. Mosely, B. S. Murray and D. Parker, *Eur. J. Mass Spectrom.*, 2009, **15**, 145–155.
- 41 A. J. Kleinnijenhuis, R. Mihalca, R. M. A. Heeren and A. J. R. Heck, *Int. J. Mass Spectrom.*, 2006, **253**, 217–224.
- 42 Y. E. M. van der Burgt, M. Palmblad, H. Dalebout, R. M. A. Heeren and A. M. Deelder, *Rapid Commun. Mass Spectrom.*, 2009, **23**, 31–38.
- 43 L. Feketeova, V. Ryzhov and R. A. J. O’Hair, *Rapid Commun. Mass Spectrom.*, 2009, **23**, 3133–3143.
- 44 E. M. Schneeberger and K. Breuker, *Chem. Sci.*, 2018, **9**, 7338–7353.
- 45 L. Han, S.-J. S. J. Hyung and B. T. Ruotolo, *Angew. Chem., Int. Ed.*, 2012, **51**, 5692–5695.
- 46 T. G. Flick and E. R. Williams, *J. Am. Soc. Mass Spectrom.*, 2012, **23**, 1885–1895.
- 47 T. R. Covey, B. A. Thomson and B. B. Schneider, *Mass Spectrom. Rev.*, 2009, **28**, 870–897.
- 48 M. A. Zenaidee, M. G. Leeming, F. T. Zhang, T. T. Funston and W. A. Donald, *Angew. Chem., Int. Ed.*, 2017, **56**, 8522–8526.
- 49 A. G. Marshall, C. L. Hendrickson and G. S. Jackson, *Mass Spectrom. Rev.*, 1998, **17**, 1–35.
- 50 A. R. Zubarev and A. Makarov, *Anal. Chem.*, 2013, **85**, 5288–5296.
- 51 S. Yin and J. A. Loo, *Int. J. Mass Spectrom.*, 2011, **300**, 118–122.
- 52 P. D. Compton, L. Zamdborg, P. M. Thomas and N. L. Kelleher, *Anal. Chem.*, 2011, **83**, 6868–6874.
- 53 A. Dobo and I. A. Kaltashov, *Anal. Chem.*, 2001, **73**, 4763–4773.
- 54 A. Natalello, C. Santambrogio and R. Grandori, *J. Am. Soc. Mass Spectrom.*, 2017, **28**, 21–28.
- 55 S. H. Lomeli, S. Yin, R. R. Ogorzalek Loo and J. A. Loo, *J. Am. Soc. Mass Spectrom.*, 2009, **20**, 593–596.
- 56 A. T. Iavarone, J. C. Jurchen and E. R. Williams, *Anal. Chem.*, 2001, **73**, 1455–

- 1460.
- 57 K. A. Douglass and A. R. Venter, *J. Am. Soc. Mass Spectrom.*, 2012, **23**, 489–497.
- 58 M. T. Donor, S. A. Ewing, M. A. Zenaidee, W. A. Donald and J. S. Prell, *Anal. Chem.*, 2017, **89**, 5107–5114.
- 59 V. Znamenskiy, I. Marginean and A. Vertes, *J. Phys. Chem. A*, 2003, **107**, 7406–7412.
- 60 A. Patriksson, E. Marklund and D. van der Spoel, *Biochemistry*, 2007, **46**, 933–945.
- 61 M. Z. Steinberg, K. Breuker, R. Elber and R. B. Gerber, *Phys. Chem. Chem. Phys.*, 2007, **9**, 4690–4697.
- 62 S. Consta and J. K. Chung, *J. Phys. Chem. B*, 2011, **115**, 10447–10455.
- 63 S. Consta, M. I. Oh, V. Kwan and A. Malevanets, *J. Am. Soc. Mass Spectrom.*, 2018, **29**, 2287–2296.
- 64 M. Porrini, F. Rosu, C. Rabin, L. Darre, H. Gomez, M. Orozco and V. Gabelica, *ACS Cent. Sci.*, 2017, **3**, 454–461.
- 65 S. G. Kondalaji, M. Khakinejad and S. J. Valentine, *J. Am. Soc. Mass Spectrom.*, 2018, **29**, 1665–1677.
- 66 R. Beveridge, L. G. Migas, R. K. Das, R. V Pappu, R. W. Kriwacki and P. E. Barran, *J. Am. Chem. Soc.*, 2019, **141**, 4908–4918.
- 67 R. Beveridge, A. S. Phillips, L. Denbigh, H. M. Saleem, C. E. MacPhee and P. E. Barran, *Proteomics*, 2015, **15**, 2872–2883.
- 68 Y. Sun, S. Vahidi, M. A. Sowole and L. Konermann, *J. Am. Soc. Mass Spectrom.*, 2016, **27**, 31–40.
- 69 M. J. Abraham, T. Murtola, R. Schulz, S. Páll, J. C. Smith, B. Hess and E. Lindahl, *SoftwareX*, 2015, **1–2**, 19–25.
- 70 J. Huang and A. D. Mackerell, *J. Comput. Chem.*, 2013, **34**, 2135–2145.
- 71 J. L. F. F. Abascal and C. Vega, *J. Chem. Phys.*, 2005, **123**, 234505.
- 72 B. F. Qiao, S. Skanthakumar and L. Soderholm, *J. Chem. Theory Comput.*, 2018, **14**, 1781–1790.
- 73 S. A. Ewing, M. T. Donor, J. W. Wilson and J. S. Prell, *J Am Soc Mass Spectrom*, 2017, **28**, 587–596.

- 74 J. O. Löfken, G. Yalovega, T. Möller, M. Riedler, A. Wark, C. Nowak, A. Kolmakov, A. V. Soldatov and A. R. B. de Castro, *Phys. Rev. B - Condens. Matter Mater. Phys.*, 2001, **64**, 1–9.
- 75 L. Seijo and Z. Barandiaran, *J. Chem. Phys.*, 1991, **94**, 3762–3773.
- 76 A. V. Zakharov, N. Vogt, S. A. Shlykov, N. I. Giricheva, I. E. Galanin, G. V. Girichev and J. Vogt, *J. Mol. Struct.*, 2004, **707**, 147–152.
- 77 R. Maurus, C. M. Overall, R. Bogumil, Y. Luo, A. G. Mauk, M. Smith and G. D. Brayer, *Biochim.Biophys.Acta*, 1997, **1341**, 1–13.
- 78 S. Vijay-Kumar, C. E. Bugg and W. J. Cook, *J.Mol.Biol.*, 1987, **194**, 531–544.
- 79 D. . Lide, *CRC Handbook of Chemistry and Physics*, CRC Press, Boca Raton, London, New York, Washington, 82nd edn., 2001.
- 80 G. J. Van Berkel and V. Kertesz, *Anal. Chem.*, 2007, **79**, 5510–5520.
- 81 N. B. Cech and C. G. Enke, *Mass Spectrom. Rev.*, 2001, **20**, 362–387.
- 82 M. Chen, L. X. Zheng, B. Santra, H. Y. Ko, R. A. DiStasio, M. L. Klein, R. Car and X. F. Wu, *Nat. Chem.*, 2018, **10**, 413–419.
- 83 J. V. Iribarne and B. A. Thomson, *J. Chem. Phys.*, 1976, **64**, 2287–2294.
- 84 I. G. Loscertales and J. F. de la Mora, *J. Chem. Phys.*, 1995, **103**, 5041–5060.
- 85 S. Consta, *J. Mol. Struct. THEOCHEM*, 2002, **591**, 131–140.
- 86 C. J. Hogan, J. A. Carroll, H. W. Rohrs, P. Biswas and M. L. Gross, *Anal. Chem.*, 2009, **81**, 369–377.
- 87 S. J. Allen, A. M. Schwartz and M. F. Bush, *Anal. Chem.*, 2013, **85**, 12055–12061.
- 88 D. C. Harris, *Quantitative Chemical Analysis*, 2010.
- 89 K. B. Shelimov and M. F. Jarrold, *J. Am. Chem. Soc.*, 1997, **119**, 2987–2994.
- 90 T. Wyttenbach and M. T. Bowers, *J. Phys. Chem. B*, 2011, **115**, 12266–12275.
- 91 C. E. Bartman, H. Metwally and L. Konermann, *Anal. Chem.*, 2016, **88**, 6905–6913.

Chapter 3. Exploring the Effects of Supercharging Agents on Salt Clusters Generated During Electrospray Ionization

3.1 Introduction

Electrospray Ionization Mass Spectrometry (ESI-MS) is a powerful tool for studying proteins and many other analytes.¹⁻⁴ The ESI process generates gaseous ions from molecules in solution. The ESI source produces a plume of droplets that are charged due to the presence of excess cations (such as H^+ , NH_4^+ , and Na^+).⁵ These droplets undergo solvent evaporation and fission events, ultimately releasing analyte ions into the gas phase. These charged species can range from atomic ions to proteins and other supramolecular species. Small analyte ions undergo Coulombically-driven ejection from the droplet surface, as described by the ion evaporation model (IEM).^{6,7} Large globular analytes such as folded proteins usually follow the charged residue model (CRM) which involves droplet evaporation to dryness with charge carriers binding to the analyte as the final solvent layers disappear.⁸ Unfolded proteins follow the chain ejection model (CEM).^{9,10} For a more thorough discussion of these mechanisms, see Chapter 1.

Many MS experiments benefit from high analyte charge states because highly charged ions are more reactive, thereby improving the fragmentation efficiency for MS/MS.^{11,12} In addition, mass analyzers that rely on image currents (such as FT-ICR and Orbitrap) have greater mass resolution with higher charge states.¹³ In the case of proteins, high charge states can be generated by supplementing the solution with organic “supercharging agents” (SCAs) such as sulfolane.¹⁴⁻¹⁶ However, the mechanisms by which proteins and other analytes become supercharged remain under investigation. Some research groups postulate that highly charged proteins are formed because SCAs cause protein unfolding in the droplet.^{14,17} A competing model is that SCAs accumulate at the droplet surface. According to this model, SCAs are poor solvents for charge carriers, and they therefore interfere with the IEM ejection of charge carriers from the droplet.^{18,19} Under CRM conditions, this implies that there are a larger number of charge carriers as the droplet dries out, such that the resulting analyte ions end up with higher charge states.

Non-volatile salts such as NaCl are a common contaminant in protein solutions. In addition, studies on salt solutions have served an important role for exploring mechanistic aspects of the ESI process.^{20–22} A particularly interesting aspect is the formation of salt clusters during ESI. Salts such as NaCl are highly soluble in water, implying that salts in bulk solution completely dissociate into single hydrated cations and anions. Yet, when electrospraying such solutions the resulting spectra show a range of cluster ions such as $[\text{Na}_{n+1}\text{Cl}_n]^+$.^{23–25} The formation mechanism of these clusters has remained controversial for many years, but recent work has shown that they assemble when nanometer-sized ESI droplets evaporate to dryness under CRM conditions.^{25–27} In other words, these clusters are prototypical “charged residues” of the ESI process.

The ESI-induced formation of salt clusters, often shows interesting magic number patterns, i.e., prominent signals that represent particularly stable cluster geometries.^{22–25} Another interesting aspect is the dissociation of these clusters following collisions with gas molecules or other activation methods.^{22,28} Considering the role of salt clusters for past ESI mechanistic investigations, it appears that these species might also contribute to a better understanding of supercharging. Specifically, very little is known about the spectral changes that are triggered by spiking salt solutions with SCAs. Will the charge states of salt clusters increase (analogous to those of proteins)? Or is supercharging a phenomenon that is limited to polypeptides, such that salt clusters are impartial to the addition of SCAs? All of these aspects are yet to be explored.

In the current chapter, we conducted experiments on salt solutions to examine whether SCAs cause supercharging of ESI-generated inorganic clusters. The initial motivation for our experiments was to test the validity of the “protein unfolding mechanism of supercharging” that has been introduced above and in Chapter 1.^{14,17} Evidently, salt clusters cannot “unfold”; the observation of more highly charged salt clusters in the presence of SCAs would therefore indicate that unfolding events are not the root cause of supercharging. On the other hand, the charge trapping model predicts that SCAs should promote the formation of more highly charged salt clusters because SCAs might suppress ion ejection from the droplet.¹⁹ Initial tests in the early stages of this work revealed that the isotopic heterogeneity of the most commonly used salt (NaCl) generated tremendously complicated spectra due to the presence of two Cl isotopes (³⁵Cl and ³⁷Cl) compounded by

the $^{12}\text{C}/^{13}\text{C}$ contributions of residual sulfolane. We therefore opted for NaI because naturally occurring ^{23}Na and ^{127}I are isotopically pure. Also, NaI and its resulting cluster ions are commonly used for ESI-MS mass calibration.²⁹ For the experiments described in this chapter, NaI solutions were infused into the ESI source in the presence and absence of sulfolane, $(\text{CH}_2)_4\text{SO}_2$, also known as tetramethylene sulfone (Figure 1.4). This compound was chosen because it represents the most commonly used SCA.^{16,30,31} Sulfolane embodies all of the typical SCA features, i.e., it has a larger dipole moment³² and a higher surface tension than water,¹⁶ as well as a low vapour pressure which makes it evaporate more slowly than water.^{16,30,33,34}

In the recent past, MD simulations have been used to address many mechanistic aspects of the ESI process.^{18,35–37} In addition to the work described in Chapter 2, this includes modeling the formation of salt-containing ESI droplets.²⁵ Here, we study the behavior of aqueous NaI solutions using a combination of experiments and MD simulations. Our results confirm that there is charge enhancement of NaI clusters when electrosprayed in the presence of sulfolane. MD simulations reveal that salt clusters are formed via the CRM following solvent evaporation to dryness. Sulfolane supports additional charge in the shrinking droplet compared to sulfolane-free solutions, and sulfolane favors the formation of highly charged salt clusters by dipole-mediated electrostatic stabilization.

3.2 Methods

3.2.1 Native ESI-MS and IMS

ESI-MS experiments were performed on a SYNAPT G2 quadrupole time-of-flight mass spectrometer (Waters, Milford, MA) in positive ion mode. Aqueous solutions containing 10 mM NaI were infused into the ESI source at $5 \mu\text{L min}^{-1}$. For supercharging experiments, the solutions were supplemented with 5% (v/v) sulfolane. Unless noted otherwise, gentle source conditions were used to limit the dissociation of salt clusters and to maintain sulfolane adducts. The ESI source was operated at 1.6 kV. The source and desolvation temperatures were 30 and 40 °C, respectively, and the cone was set to 5 V. To separate different ion species that had overlapping m/z values, we applied ion mobility separation

(IMS). For this purpose the Triwave was enabled (trap DC entrance 0 V, trap DC bias 15 V, Trap DC -2 V, trap DC exit 1 V, IMS DC entrance 6.7 V, He cell DC 10 V, He exit -5 V, IMS bias 3 V, IMS DC exit 0 V, transfer DC entrance 1 V, transfer DC exit 1 V, trap wave velocity 100 m s⁻¹, trap wave height 1 V, IMS wave velocity 450 m s⁻¹, IMS wave height 8 V, transfer wave velocity 247 m s⁻¹, and transfer wave height 4 V). Isotope distributions were modeled using the Scientific Instrument Services online isotopic abundance calculator (<https://www.sisweb.com/mstools/isotope.htm>).

3.2.2 MD Simulations

ESI droplets were simulated with Gromacs 2019³⁸ using the CHARMM36³⁹ forcefield and the TIP4P/2005⁴⁰ water model. Droplets with a radius of 3 nm were built (~2600 water or ~2300 water / 200 sulfolane molecules) and charged using randomly placed Na⁺ and I⁻ ions. Different numbers of Na⁺ and I⁻ were tested, but the initial droplet charge was always 18+, which corresponds to the Rayleigh limit for a 3 nm droplet radius. After energy minimization and equilibration, MD runs were performed for 200 ns at 370 K, followed by 150 ns at 450 K to speed up solvent evaporation, for a total simulation time of 350 ns. To promote desolvation of salt/sulfolane clusters produced from water/sulfolane droplets, these clusters were subject to “forced evaporation” starting at $t = 300$ ns. The temperature remained at 450 K, but every 2.5 ns a single sulfolane molecule (the one that was farthest from the droplet center of mass) was removed from the cluster. This procedure continued until the simulation time reached 350 ns. This same forced evaporation procedure has previously been used in earlier ESI simulation studies on proteins to deal with the extremely slow evaporation of sulfolane during the final stages of CRM runs.¹⁹ ESI charge states were determined by tallying the number of Na⁺ and I⁻ ions within the final salt cluster. In addition, some of the clusters produced in the MD runs were exposed to heating from 450 to 1400 K over a period of 100 ns. All runs were repeated five times for each solvent condition, with different starting conformations and velocities. Lennard-Jones parameters for Na⁺ were adapted from the CHARMM36³⁹ forcefield, and parameters for I⁻ were taken from literature ($\epsilon = 0.656496$ kJ/mol; $\sigma = 0.519226$ nm).⁴¹ The resulting bond length for an isolated Na—I unit (2.9 Å) in low temperature MD runs (0 K) was similar to earlier

density functional theory (DFT) results (2.73 Å),⁴² thereby supporting the appropriateness of the Lennard-Jones parameters.

3.3 Results and Discussion

3.3.1 ESI-MS of NaI Solutions

In positive ion mode under gentle ion sampling conditions, 10 mM solutions of NaI electrosprayed in water generated mostly singly charged $[\text{Na}_{(n+1)}\text{I}_n]^+$ cluster ions, with some contributions from $[\text{Na}_{(n+2)}\text{I}_n]^{2+}$ at much lower intensity (Figure 3.1A). Spiking the NaI solution with 5% sulfolane resulted in the formation of sulfolane-adducted NaI clusters $[\text{Na}_n\text{I}_m\text{Sulfolane}_s]^{(n-m)+}$, mostly with a 2+ charge, but with some contributions from 3+ species (Figure 3.1B/C). In other words, sulfolane caused a substantial charge enhancement (“supercharging”) of ESI-generated NaI clusters. It appears that this is the first time that an SCA has been shown to have this effect on salt clusters. Thus, our data demonstrate that sulfolane can boost charge states not only for proteins, but also for simple inorganic species.

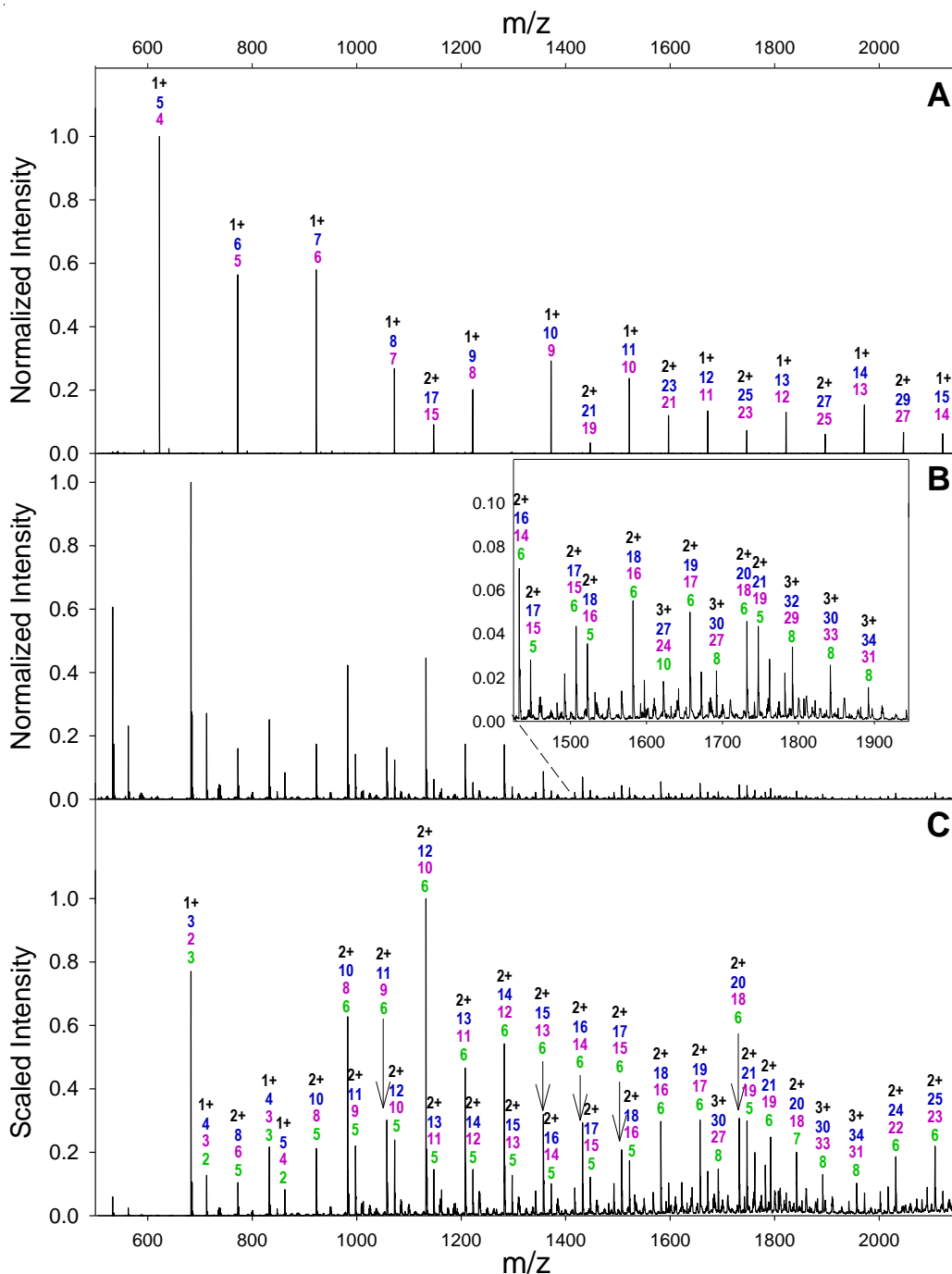


Figure 3.1 ESI mass spectra of 10 mM NaI acquired under gentle ion sampling conditions (cone = 5 V). (A) water, and (B) in water with 5% sulfolane. (C) Same as in panel B, but with y axis scaled according to $y = \text{intensity} \times (m/z - m/z_{\min})$ to facilitate the visualization of low intensity peaks. Ionic signals are annotated with their charge state z (black), number of Na^+ (blue) number of I^- (purple), and number of sulfolane (green).

Interestingly, the shift to higher charge was accompanied by sulfolane molecule adduction. That is, only salt clusters that were decorated with sulfolane showed higher charge states. Raising the cone voltage from 5 to 100 V caused collisional heating of the clusters. Under these conditions all sulfolane molecules dissociated from the clusters, accompanied by a decrease in the size of the observed clusters to roughly half their original values (Figure 3.2.). In other words, collision-induced dissociation of these clusters not only caused the loss of residual sulfolane but also the fragmentation of doubly charged ions into singly charged product ions. This last aspect is consistent with fragmentation experiments on other clusters in the absence of sulfolane.²⁸ The remaining clusters obtained under these conditions all corresponded to singly charged $[\text{Na}_{(n+1)}\text{I}_n]^+$ species (Figure 3.2). The data of Figure 3.1 reinforce the view that the viability of highly charged clusters depends on direct interactions with sulfolane. This is in contrast to the behavior of proteins, where high charge states persist even after all SCA molecules have left.^{19,35} Nonetheless, the role of direct sulfolane/analyte interactions for salt cluster supercharging is reminiscent of mechanistic proposals that were developed in the context of protein supercharging.^{31,35}

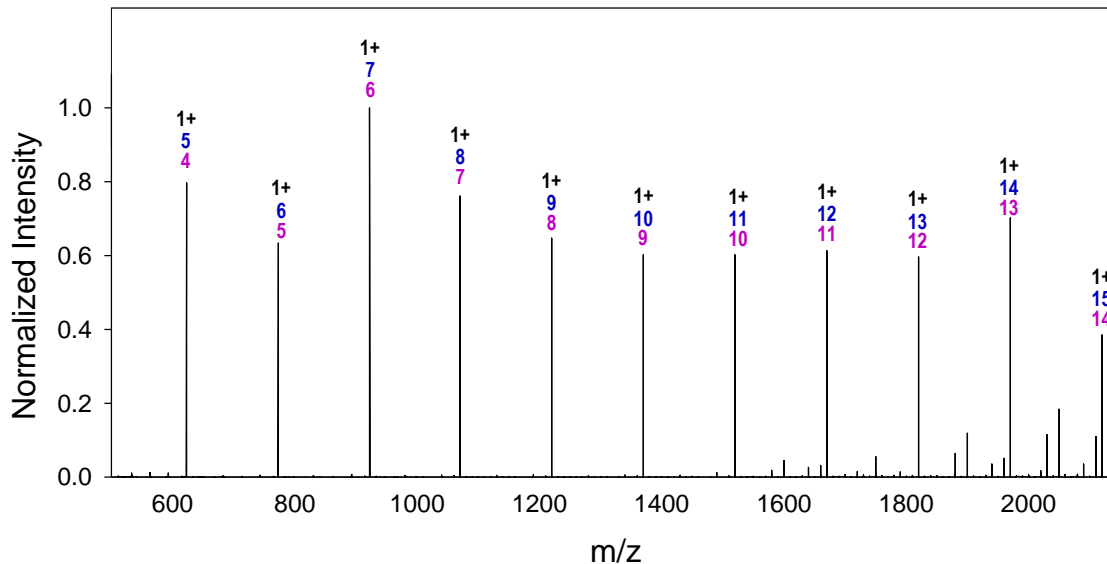


Figure 3.2 ESI mass spectrum of 10 mM NaI in 5% sulfolane acquired using harsh ion sampling conditions (cone voltage =100 V). Peaks are annotated as in Figure 3.1

For NaI in 5% sulfolane, there is substantial overlap of coexisting species in the mass spectra because multiple ions occupy very similar m/z regions (Figure 3.1A/B). For example, $[\text{Na}_{10}\text{I}_8\text{Sulfolane}_6]^{2+}$ has the same monoisotopic m/z as $[\text{Na}_5\text{I}_4\text{Sulfolane}_3]^+$. IMS can be used to deconvolute the contributions of 2+ and 1+ clusters in such regions (Figure 3.3A). As an example, the sulfolane data in Figure 3.1B/C show a strong signal at m/z 982.6. IMS reveals that two ion species contribute to this signal, with the stronger contribution being due to the 2+ cluster. The exact identity of the clusters can be elucidated using isotopic modeling, because the $^{12}\text{C}/^{13}\text{C}$ isotope pattern of sulfolane provides characteristic signatures (Figure 3.3C/D). The isotopic models for all peaks match extremely well, confirming the legitimacy of our assignments. For most of the signals in the absence of sulfolane, only single ion species were detected by IMS. This is exemplified for m/z 622.6 (Figure 3.4A) and m/z 772.5 (Figure 3.4B), thereby confirming the absence of 2+/1+ overlap.

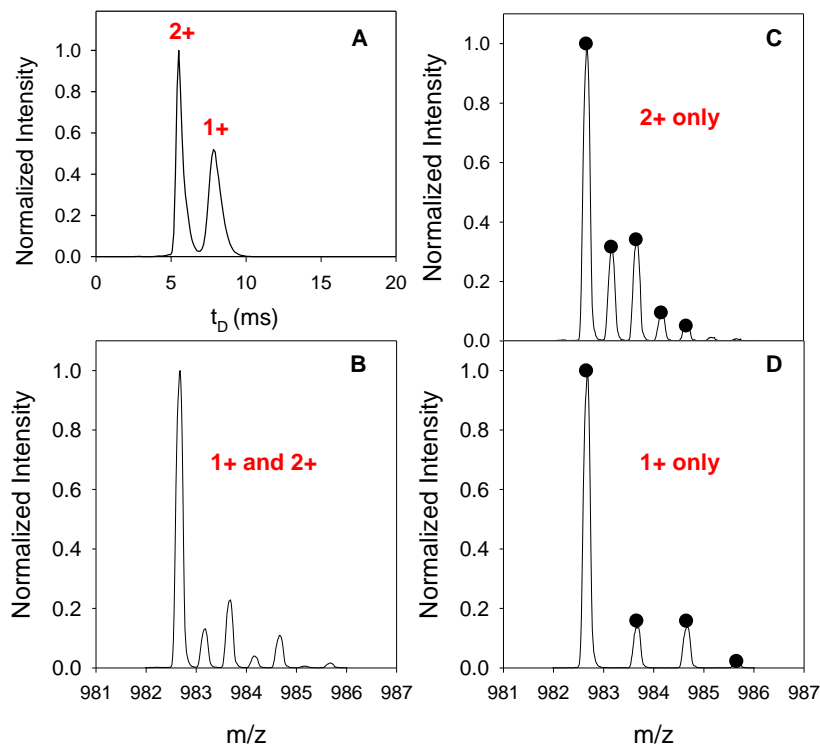


Figure 3.3 (A) Drift time mobilogram for a signal at $m/z=982.6$ seen after electrospraying 10 mM NaI in 5% sulfolane. (B) Cumulative ESI mass spectrum extracted from the mobilogram. (C) ESI mass spectrum for doubly charged species extracted from the mobilogram, with isotope model for $[Na_{10}I_8Sulfolane_6]^{2+}$; black circles. (D) ESI mass spectrum for singly charged extracted from the mobilogram with isotope model for $[Na_5I_4Sulfolane_3]^+$; black circles.

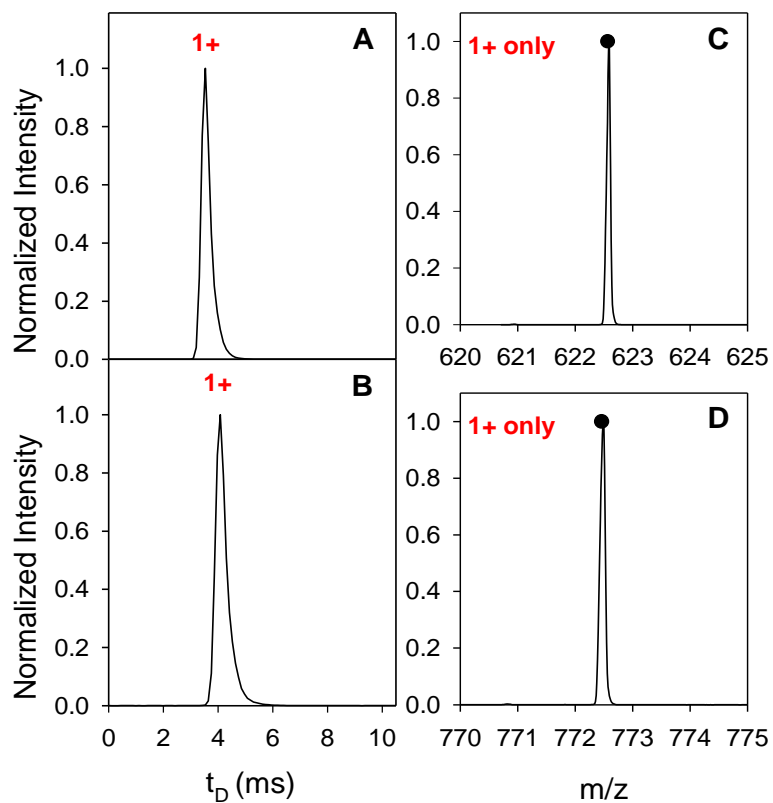


Figure 3.4 (A/B) Drift time mobilogram and (C/D) ESI mass spectrum for 10 mM NaI in water from (A/C) peak at $m/z=622.6$, and (B/D) peak at $m/z=772.5$. Only singly charged ion species are detected. (C) Model for $[\text{Na}_5\text{I}_4]^+$; black circle, and (D) model for $[\text{Na}_6\text{I}_5]^+$; black circle.

3.3.2 MD Simulations of Salt-Containing Electrospray Droplets

ESI droplets consisting of water or water/sulfolane with Na^+ and I^- ions were assembled computationally, and their temporal evolution was studied in MD simulations. We will first focus on droplets where the initial droplet charge was implemented by incorporation of 38 Na^+ and 20 I^- (Figure 3.5). The droplets underwent rapid evaporative shrinkage, in conjunction with the ejection of Na^+ that were solvated by some water or water/sulfolane. For both water and water/sulfolane we never observed the ejection of bare Na^+ ions. Ultimately, NaI clusters were formed by droplet evaporation to dryness, in agreement with earlier NaCl simulations on water droplets²⁵ and consistent with the observation of abundant cluster ions in our experiments (Figure 3.1). Droplet evaporation to dryness implies that the salt clusters are CRM products. The alternative process, i.e., the IEM ejection of clusters larger than Na_2I^+ was never observed. For the water/sulfolane systems we observed enrichment of sulfolane during evaporative droplet shrinkage, i.e., sulfolane tended to stay behind as expected based on its low vapor pressure.³⁵ For the MD runs in Figure 3.5, the water droplet produced a completely desolvated $[\text{Na}_{22}\text{I}_{20}]^{2+}$ cluster. In contrast, the water/sulfolane droplet produced a $[\text{Na}_{23}\text{I}_{20}\text{Sulfolane}_3]^{3+}$ cluster. All the remaining sulfolane molecules were located on the cluster surface rather than in the interior. Qualitatively, these MD data agree well with the experimental mass spectra of (Figure 3.1); water droplets produced solvent-free clusters in low charge states while water/sulfolane droplets produced higher charge states containing some residual sulfolane. However, the absolute charge states produced in our MD runs were somewhat higher than in the experiments, i.e. 2+/3+ vs. 1+/2+.

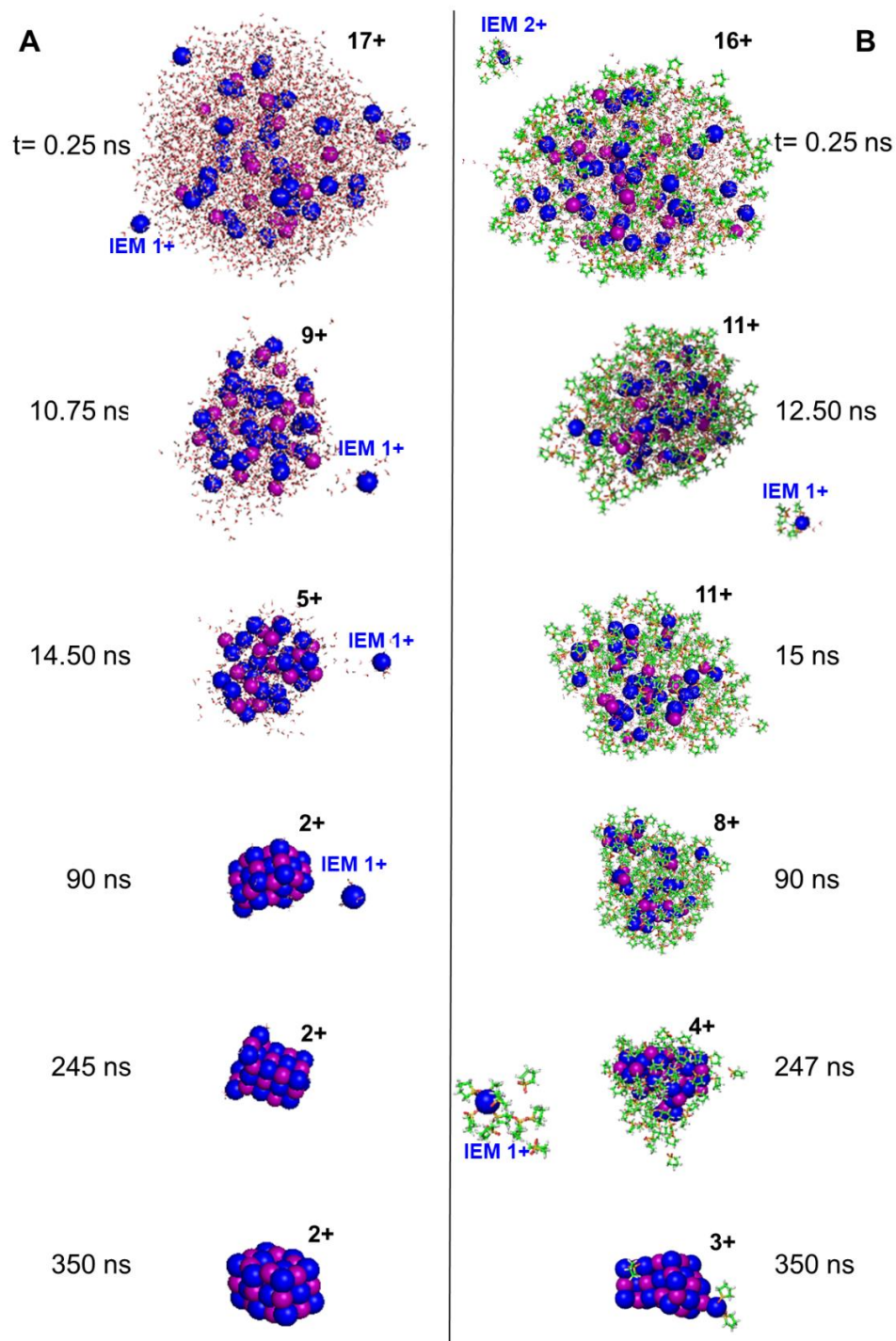


Figure 3.5 MD simulation snapshots depicting the temporal evolution of ESI droplets with an initial charge of 18+ (38 Na⁺ and 20 I⁻) in (A) water and (B) water/sulfolane. Field emission events for Na⁺ are marked as “IEM”. The droplet charge is indicated. Na⁺, blue; I⁻, purple; sulfolane carbon, green.

For the MD data in Figure 3.5 reflecting droplets that initially contained 38 Na⁺/ 20 I⁻, Figure 3.6 tallies the number of molecules in the droplet vs. time for various constituents averaged over five runs. For aqueous droplets (Figure 3.6A), Na⁺ was ejected as the water molecules evaporated. Just before the final water molecules left, the clusters attained their final charge state and remained stable for the remainder of the run.

The process for water/sulfolane droplets (Figure 3.6B) contrasts the straightforward IEM ejection observed in Figure 3.6A. Water evaporation occurred early in the run, but there was hardly any sulfolane evaporation until the temperature was increased to 450 K at 200 ns. At 450 K, the sulfolane began to evaporate and the charge carriers had a greater likelihood of being ejected. As long as there were a large number of sulfolane molecules in the droplet, the droplet charge remained high. Qualitatively, this is consistent with the experimental observation that sulfolane adduction facilitates charge enhancement. The average cluster composition [Na_(22.2±0.8) I_(20.0±0.4) Sulfolane_(0.8±1.1)]^{(2.4±0.5)+} formed under the MD conditions of Figure 3.6D resemble the experimentally observed [Na/I/Sulfolane]²⁺ signals in Figure 3.1B/C at m/z > 1500.

MD runs were also conducted on droplets with other initial ion compositions, while retaining an initial droplet charge of 18+ (26 Na⁺/8 I⁻, 48 Na⁺/30 I⁻, and 58 Na⁺/40 I⁻). Figure 3.7 shows results for these initial Na⁺/ I⁻ ratios, all of which qualitatively resulted in very similar behavior: high charge was maintained in the presence of sulfolane until temperature was increased and sulfolane began to evaporate, upon which charge was lost.

Returning to the key finding of this work, our ESI-MS experiments (Figure 3.1) show that the presence of sulfolane results in salt clusters with higher charge states. The MD simulations reproduce this key finding, as the average final charge of clusters run in sulfolane/water is higher than clusters run in water. Figure 3.8 highlights this trend in the MD data for different time points. This figure also makes it clear that the trend to form higher charge states is most prominent early during the runs, when the clusters still carry a large sulfolane shell (*t* = 100 ns, 200 ns, Figure 3.8A/B). As time progresses, the charge state difference diminishes but remains visible even at the end of the runs (*t* = 350 ns, Figure 3.8D).

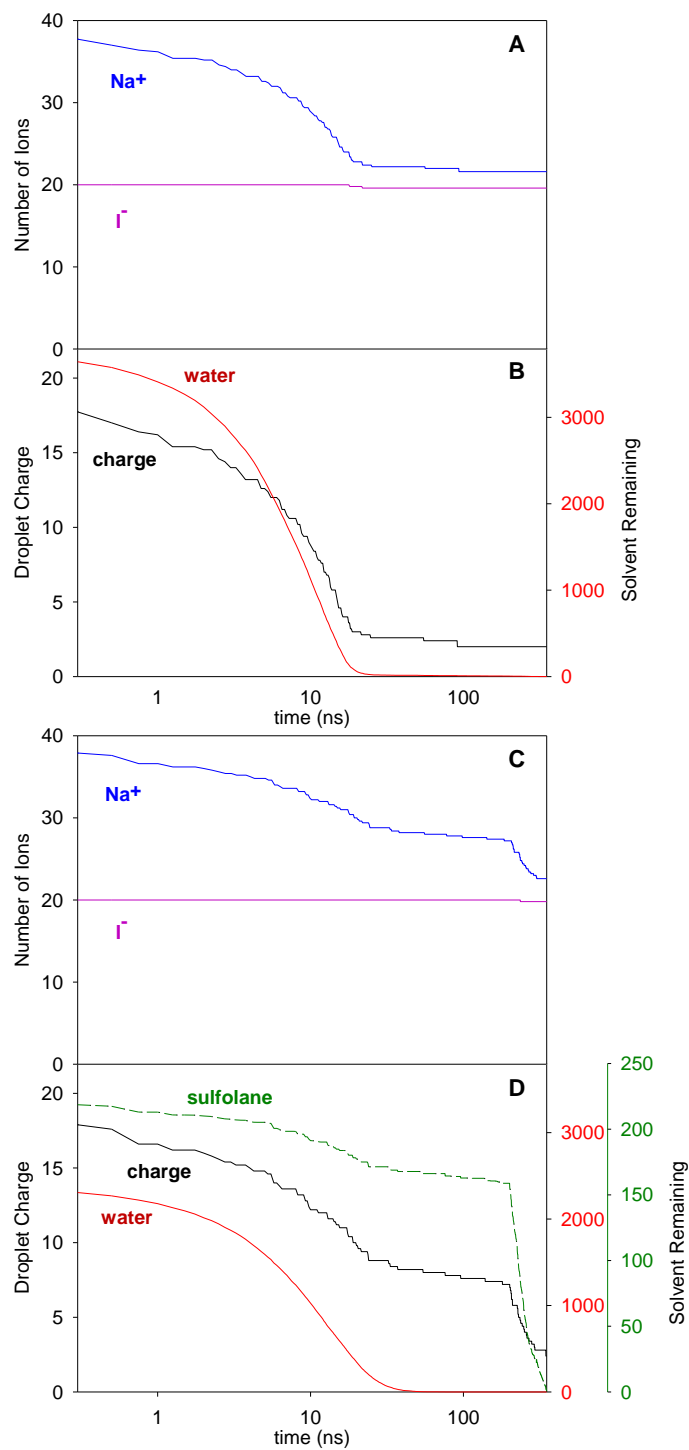


Figure 3.6 MD data, depicting changes of various droplet components over time. The initial droplets contained 38 Na^+ and 20 I^- . (A/B) Water droplet. (C/D) Water/sulfolane droplet. Each of the profiles represents an average of five independent runs. Time axes are scaled logarithmically.

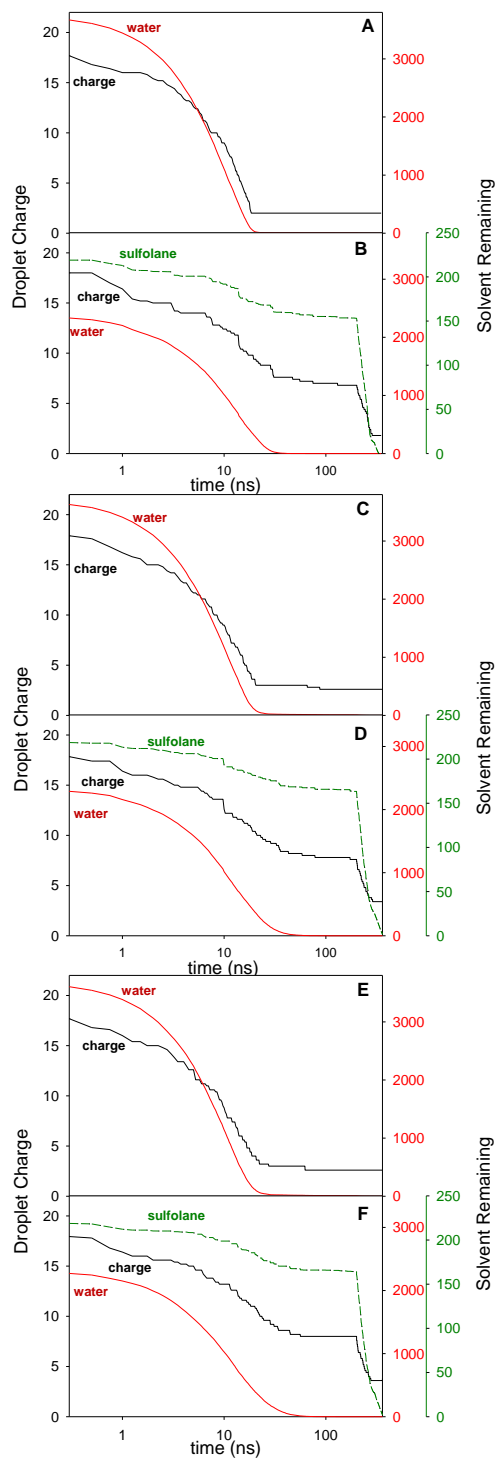


Figure 3.7 MD data, depicting changes of various droplet components over time for water (A/C/E) and water/sulfolane droplets (B/D/F). The initial droplets contained (A/B) 26 Na^+ /8 I^- , (C/D) 48 Na^+ / 30 I^- , and (E/F) 58 Na^+ / 40 I^- .

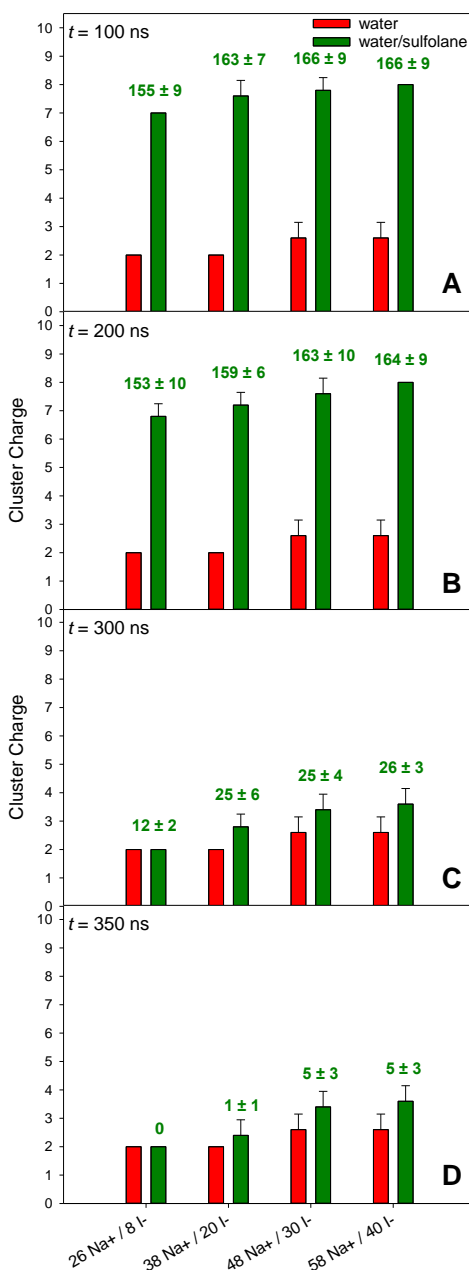


Figure 3.8 MD data, depicting the average cluster charge for various conditions at (A) $t = 100$ ns, (B) $t = 200$ ns and (C) $t = 300$ ns and (D) $t = 350$ ns. Clusters in water are indicated as red bars and clusters in water/sulfolane are indicated as green bars. The average number of sulfolane molecules remaining in the droplet at each time point is indicated in green above the sulfolane cluster bar. Results are the average of 5 individual runs for each condition. The absence of error bars refers to conditions that consistently yielded the same charge state.

To further investigate the sulfolane-induced charge stabilization of the NaI clusters, partially desolvated clusters were heated in MD runs employing a temperature ramp from 450 K to 1400 K over 100 ns (Figure 3.9). Qualitatively, these conditions mimic the collisional heating experiments of Figure 3.2. The initial cluster conformations for these simulations were taken from $t = 300$ ns in Figure 3.6B/D, when forced evaporation would have started. At this time point, cluster ions from water droplets were completely desolvated and cluster ions for water/sulfolane droplets retained ~ 22 sulfolane molecules. This time point was chosen for these simulations as the initial cluster stoichiometries resemble the approximate m/z range displayed in Figure 3.1. Any stabilization should result in delayed fragmentation. Indeed, the presence of sulfolane does delay fragmentation of the cluster, even though clusters run in water/sulfolane begin with a higher charge than in water (Figure 3.9B). Consequently, the fragmentation of sulfolane-adducted NaI clusters is only prevalent upon sulfolane departing from the cluster (Figure 3.9B). Under these conditions, high temperature activation results in the loss of sulfolane molecules followed by the fragmentation of doubly or triply charged clusters to singly charged or neutral product ions. This result matches the experimental findings in Figure 3.2, where we observed that high cone voltage collisional activation caused the loss of residual sulfolane molecules and fragmentation of doubly charged ions into singly charged product ions.

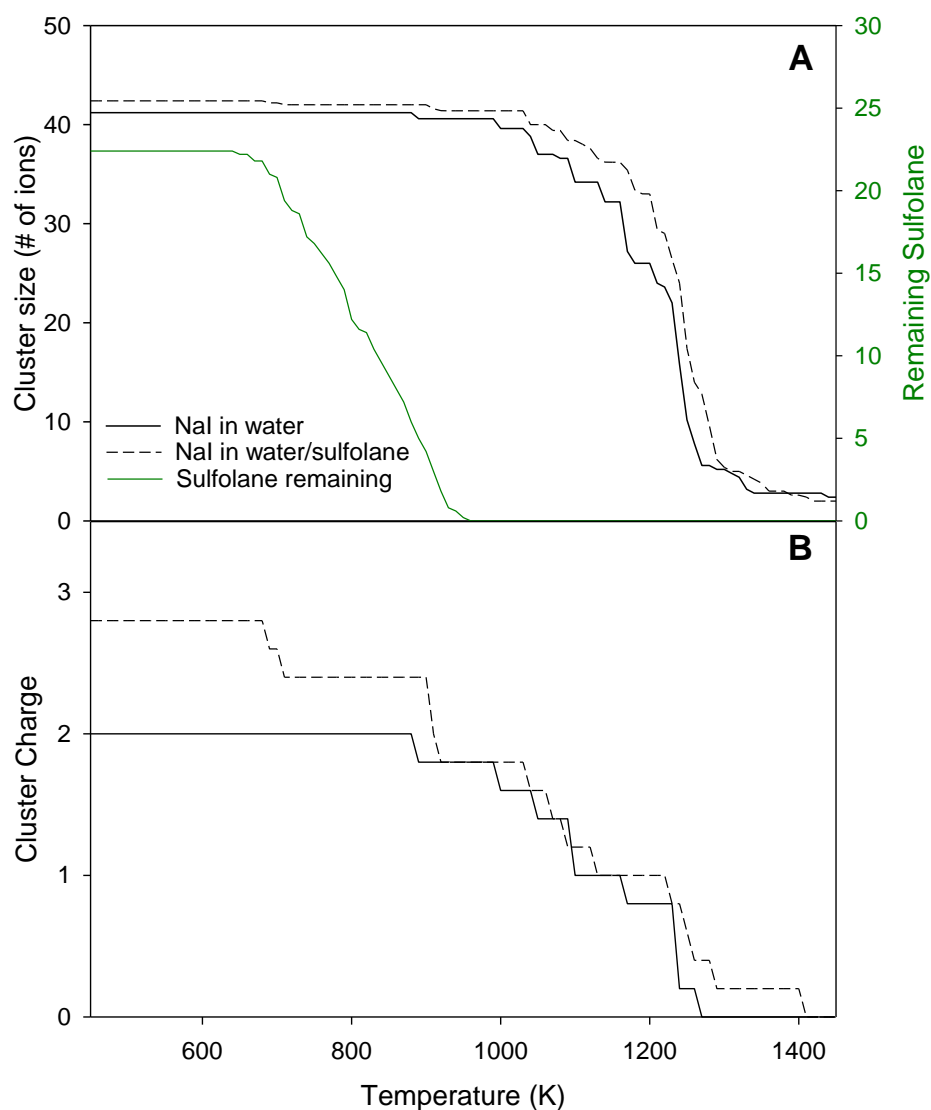


Figure 3.9 MD data for “collisionally heated clusters”, depicting fragmentation behaviour for NaI that was previously in water; black, and NaI clusters with adducted sulfolane molecules; black dashed. (A) Indicates the size of the cluster based on the number of ions and (B) indicates the net cluster charge. Green line indicates the number of sulfolane molecules remaining in the sulfolane-containing clusters. The profiles shown here were averaged from 5 individual runs.

3.4 Conclusions

This chapter explored the use of salt solutions as test systems to elucidate mechanistic aspects of the ESI process. Our experiments revealed that spiking NaI solutions with sulfolane results in the formation of more highly charged clusters (mostly $2+/3+$ opposed to $1+/2+$ in water). We attribute this effect to the presence of residual sulfolane molecules which stabilize highly charged clusters due to charge-dipole interactions. This supercharging mechanism relies on two critical features of the SCA used here. (1) The dipole moment of sulfolane is more than twice that of water.^{16,31,32} (2) The low vapor pressure of sulfolane renders this molecule very “sticky” so that it remains associated with the clusters after the transition in the gas phase.^{16,30,33,34} This can be contrasted to the behavior of water, which has a lower dipole moment and a higher vapor pressure.

Although this chapter did not focus on proteins, we can nonetheless draw some conclusions related to protein supercharging. Salt clusters cannot “unfold” in the droplet, yet, they undergo supercharging in the presence of sulfolane. This observation demonstrates that ESI-MS analytes can show supercharging *without* undergoing major conformational changes, thereby suggesting that the same may be true for proteins. In other words, we consider the data presented here as evidence against the proposed unfolding mechanism. Overall, this work provides another successful example for the use of MD simulations in conjunction with experimental investigations for probing fundamental aspects of ESI mechanisms.

3.5 References

- 1 G. F. Pirrone, R. E. Iacob and J. R. Engen, *Anal. Chem.*, 2015, **87**, 99–118.
- 2 V. L. Mendoza and R. W. Vachet, *Mass Spectrom. Rev.*, 2009, **28**, 785–815.
- 3 U. Kaur, D. T. Johnson, E. E. Chea, D. J. Deredge, J. A. Espino and L. M. Jones, *Anal. Chem.*, 2019, **91**, 142–155.
- 4 A. Sinz, C. Arlt, D. Chorev and M. Sharon, *Protein Sci.*, 2015, **24**, 1193–1209.
- 5 P. Kebarle and U. H. Verkerk, *Mass Spectrom. Rev.*, 2009, **28**, 898–917.
- 6 I. G. Loscertales and J. Fernández De La Mora, *J. Chem. Phys.*, 1995, **103**, 5041–5060.
- 7 L. Konermann, E. Ahadi, A. D. Rodriguez and S. Vahidi, *Anal. Chem.*, 2013, **85**, 2–9.
- 8 M. Dole, L. L. Mack, R. L. Hines, D. O. Chemistry, R. C. Mobley, L. D. Ferguson and M. B. Alice, *J. Chem. Phys.*, 1968, **49**, 2240–2249.
- 9 M. T. Donor, S. A. Ewing, M. A. Zenaidee, W. A. Donald and J. S. Prell, *Anal. Chem.*, 2017, **89**, 5107–5114.
- 10 H. Metwally, Q. Duez and L. Konermann, *Anal. Chem.*, 2018, **90**, 10069–10077.
- 11 A. T. Iavarone and E. R. Williams, *Int. J. Mass Spectrom.*, 2002, **219**, 63–72.
- 12 M. A. Zenaidee and W. A. Donald, *Analyst*, 2015, **140**, 1894–1905.
- 13 R. D. Smith, X. Cheng, J. E. Brace, S. A. Hofstadler and G. A. Anderson, *Nature*, 1994, **369**, 137–139.
- 14 A. T. Iavarone and E. R. Williams, *J. Am. Chem. Soc.*, 2003, **125**, 2319–2327.
- 15 S. H. Lomeli, S. Yin, R. R. Ogorzalek Loo and J. A. Loo, *J. Am. Soc. Mass Spectrom.*, 2009, **20**, 593–596.
- 16 C. A. Teo and W. A. Donald, *Anal. Chem.*, 2014, **86**, 4455–4462.
- 17 C. C. Going and E. R. Williams, *Anal. Chem.*, 2015, **87**, 3973–3980.
- 18 H. Metwally and L. Konermann, *Anal. Chem.*, 2018, **90**, 4126–4134.
- 19 H. Metwally, R. G. McAllister, V. Popa and L. Konermann, *Anal. Chem.*, 2016, **88**, 5345–5354.
- 20 U. H. Verkerk and P. Kebarle, *J. Am. Soc. Mass Spectrom.*, 2005, **16**, 1325–1341.

- 21 R. N. Grewal, H. El Aribi, J. C. Smith, C. F. Rodriguez, A. C. Hopkinson and K. W. M. Siu, *Int. J. Mass Spectrom.*, 2002, **219**, 89–99.
- 22 J. Zhang, B. Bogdanov, A. Parkins and C. M. McCallum, *J. Phys. Chem. A*, 2020, **124**, 3535–3541.
- 23 C. Hao, R. E. March, T. R. Croley, J. C. Smith and S. P. Rafferty, *J. Mass Spectrom.*, 2001, **36**, 79–96.
- 24 A. T. Blades, M. Peschke, U. H. Verkerk and P. Kebarle, *J. Am. Chem. Soc.*, 2004, **126**, 11995–12003.
- 25 L. Konermann, R. G. McAllister and H. Metwally, *J. Phys. Chem. B*, 2014, **118**, 12025–12033.
- 26 L. Charles, D. Pépin, F. Gonnet and J. C. Tabet, *J. Am. Soc. Mass Spectrom.*, 2001, **12**, 1077–1084.
- 27 S. Zhou and M. Hamburger, *Rapid Commun. Mass Spectrom.*, 1996, **10**, 797–800.
- 28 T. D. Schachel, H. Metwally, V. Popa and L. Konermann, *J. Am. Soc. Mass Spectrom.*, 2016, **27**, 1846–1854.
- 29 J. F. Anacleto, S. Pleasance and R. K. Boyd, *Org. Mass Spectrom.*, 1992, **27**, 660–666.
- 30 S. H. Lomeli, I. X. Peng, S. Yin, R. R. Ogorzalek Loo and J. A. Loo, *J. Am. Soc. Mass Spectrom.*, 2010, **21**, 127–131.
- 31 K. A. Douglass and A. R. Venter, *J. Am. Soc. Mass Spectrom.*, 2012, **23**, 489–497.
- 32 U. Tilstam, *Org. Process Res. Dev.*, 2012, **16**, 1273–1278.
- 33 R. R. Ogorzalek Loo, R. Lakshmanan and J. A. Loo, *J. Am. Soc. Mass Spectrom.*, 2014, **25**, 1675–93.
- 34 H. J. Sterling, A. F. Kintzer, G. K. Feld, C. A. Cassou, B. A. Krantz and E. R. Williams, *J. Am. Soc. Mass Spectrom.*, 2012, **23**, 191–200.
- 35 I. Peters, H. Metwally and L. Konermann, *Anal. Chem.*, 2019, **91**, 6943–6952.
- 36 E. Aliyari and L. Konermann, *Anal. Chem.*, 2020, **92**, 10807–10814.
- 37 D. Kim, N. Wagner, K. Wooding, D. E. Clemmer and D. H. Russell, *J. Am. Chem. Soc.*, 2017, **139**, 2981–2988.
- 38 M. J. Abraham, T. Murtola, R. Schulz, S. Páll, J. C. Smith, B. Hess and E. Lindah, *SoftwareX*, 2015, **1–2**, 19–25.

- 39 J. Huang and A. D. MacKerell, *J. Comput. Chem.*, 2013, **34**, 2135–2145.
- 40 J. L. F. F. Abascal and C. Vega, *J. Chem. Phys.*, 2005, **123**, 234505.
- 41 B. A. Bauer and S. Patel, *J. Chem. Phys.*, 2010, **132**, 024713.
- 42 M. T. Jafari-Chermahini and H. Tavakol, *Comput. Theor. Chem.*, 2018, **1145**, 37–43.

Chapter 4. Conclusions and Future Directions

4.1 Conclusions

Many mechanistic aspects related to ESI are contentious and continue to be examined by laboratories around the world. Many issues surround the question of how the transition from solution into the gas phase affects the structure of analytes, and how exactly the overall charge of electrosprayed analytes is determined. Solution additives such as organic SCAs and multivalent metal salts facilitate the generation of higher ESI charge states for proteins and other analytes.¹⁻⁵ The mechanisms whereby these additives affect the outcome of the ESI process are particularly contentious. The persistence of these open questions prompted us to ascertain how supercharging reagents behave using a combination of ESI-MS experiments and MD simulations. The work in this thesis complements earlier MD simulation studies that have uncovered the mechanistic foundation of other ESI-related phenomena.^{1,6-13}

In Chapter 2, we utilized MD simulations to investigate the protein charge enhancing effects of LaCl_3 when electrosprayed in non-denaturing solutions. The trivalent nature of La^{3+} drives the formation of chelation contacts with the protein early during the ESI process, when the electrospray droplet is still highly solvated. Irreversible binding of multiple La^{3+} ions to the protein prevents the IEM ejection of these metal ions. The resulting dried-out protein ions carry more charge than for droplets that only contain monovalent ions such as Na^+ . In Chapter 3 we focused on a much simpler system, by combining ESI-MS experiments with MD simulations to examine the supercharging effects of sulfolane on NaI clusters. The motivation to study such a non-protein system was to determine if protein-specific features (“unfolding”) are at the core of the supercharging mechanism. Spiking NaI solutions with sulfolane resulted in the formation of sulfolane-adducted cluster ions with a higher charge than electrospraying in water only. MD simulations establish that sulfolane supports additional charge within shrinking electrospray droplets compared to sulfolane-free solutions, and sulfolane favors the formation of highly charged salt clusters by dipole-mediated electrostatic stabilization. Evidently, this NaI supercharging has nothing to do with protein conformational changes. In other words, our findings argue against proposals put forward by some researchers,

according to which unfolding in the droplet is responsible for protein supercharging¹⁴ (because NaI clusters cannot “unfold”).

The mechanism of La³⁺-induced charge enhancement as well as the salt cluster stabilization effects of sulfolane illustrates how MD simulations can be combined with MS experiments to elucidate mechanistic aspects of ESI. Continuous advancements in computational and experimental capabilities will allow more sophisticated systems to be investigated. Our hope is that further studies will provide new insights into the mechanisms by which analytes are transferred from solution into the gas phase during ESI.

4.2 Future Directions

The investigation of charge enhancement from trivalent La³⁺ provides an interesting purview into the use of salt solutions for MS-based applications. A potential avenue for exploration is the effects of additional salts, especially metal ions that are physiologically relevant such as Fe²⁺, Mg²⁺ and Zn²⁺. These metal ions are common protein cofactors and prevalent contaminants in native protein MS samples.^{15–19} Thus, understanding the binding mechanisms, the effects on ionization, and the possible contribution to charge enhancement of these metals are important research goals. These additives can again be tested using a combination of native ESI-MS and MD simulation techniques.

The formation of ESI-generated droplets begins in the μm range until fission events and desolvation forms offspring droplets in the nm range.²⁰ One of the limitations of MD simulations is that increasing the size of the system presents computational tradeoffs as large systems (such as μm ESI droplets) are very computationally expensive. These systems require extremely long run times (months to years, with currently available resources).²¹ As the technological capabilities of graphics processing units (GPUs) increase and performance is continuously optimized for simulations, much larger and more complicated systems will soon come within reach. The quality of MD data improves by including as many real parameters as possible, so modeling ESI droplets in the μm range would provide a truly holistic view of the entire ESI process. This may be possible in the future with the release of new, upgraded simulation software packages and powerful GPU additions.

4.3 References

- 1 L. Konermann, H. Metwally, Q. Duez and I. Peters, *Analyst*, 2019, **144**, 6157–6171.
- 2 S. H. Lomeli, S. Yin, R. R. Ogorzalek Loo and J. A. Loo, *J. Am. Soc. Mass Spectrom.*, 2009, **20**, 593–596.
- 3 T. G. Flick and E. R. Williams, *J. Am. Soc. Mass Spectrom.*, 2012, **23**, 1885–1895.
- 4 K. A. Douglass and A. R. Venter, *J. Am. Soc. Mass Spectrom.*, 2012, **23**, 489–497.
- 5 M. T. Donor, S. A. Ewing, M. A. Zenaidee, W. A. Donald and J. S. Prell, *Anal. Chem.*, 2017, **89**, 5107–5114.
- 6 V. Znamenskiy, I. Marginean and A. Vertes, *J. Phys. Chem. A*, 2003, **107**, 7406–7412.
- 7 A. Patriksson, E. Marklund and D. van der Spoel, *Biochemistry*, 2007, **46**, 933–945.
- 8 M. Z. Steinberg, K. Breuker, R. Elber and R. B. Gerber, *Phys. Chem. Chem. Phys.*, 2007, **9**, 4690–4697.
- 9 S. Consta, M. I. Oh, V. Kwan and A. Malevanets, *J. Am. Soc. Mass Spectrom.*, 2018, **29**, 2287–2296.
- 10 M. Porrini, F. Rosu, C. Rabin, L. Darre, H. Gomez, M. Orozco and V. Gabelica, *ACS Cent. Sci.*, 2017, **3**, 454–461.
- 11 R. Beveridge, L. G. Migas, R. K. Das, R. V Pappu, R. W. Kriwacki and P. E. Barran, *J. Am. Chem. Soc.*, 2019, **141**, 4908–4918.
- 12 S. Consta and J. K. Chung, *J. Phys. Chem. B*, 2011, **115**, 10447–10455.
- 13 D. Kim, N. Wagner, K. Wooding, D. E. Clemmer and D. H. Russell, *J. Am. Chem. Soc.*, 2017, **139**, 2981–2988.
- 14 A. T. Iavarone and E. R. Williams, *J. Am. Chem. Soc.*, 2003, **125**, 2319–2327.
- 15 D. F. Wallace, *Clin. Biochem. Rev.*, 2016, **37**, 51–62.
- 16 B. Zhang, Y. Zhang, Z. X. Wang and Y. Zheng, *J. Biol. Chem.*, 2000, **275**, 25299–25307.
- 17 J. Pan, K. Xu, X. Yang, W. Y. Choy and L. Konermann, *Anal. Chem.*, 2009, **81**, 5008–5015.
- 18 N. A. Bushmarina, *Protein Sci.*, 2006, **15**, 659–671.
- 19 K. A. McCall, C. Huang and C. A. Fierke, *J. Nutr.*, 2000, **130**, 1437S–1446S.
- 20 P. Kebarle and U. H. Verkerk, *Mass Spectrom. Rev.*, **28**, 898–917.

- 21 J. Wong-ekkabut and M. Karttunen, *Biochim. Biophys. Acta - Biomembr.*, 2016, **1858**, 2529–2538.

Appendix I – Permissions



RightsLink®



Home



Help



Email Support



Sign in



Create Account

Enhancing Protein Electrospray Charge States by Multivalent Metal Ions: Mechanistic Insights from MD Simulations and Mass Spectrometry Experiments



Author: Leanne M. Martin, Lars Konermann

Publication: Journal of the American Society for Mass Spectrometry

Publisher: American Chemical Society

Date: Jan 1, 2020

Copyright © 2020, American Chemical Society

PERMISSION/LICENSE IS GRANTED FOR YOUR ORDER AT NO CHARGE

This type of permission/license, instead of the standard Terms & Conditions, is sent to you because no fee is being charged for your order. Please note the following:

- Permission is granted for your request in both print and electronic formats, and translations.
- If figures and/or tables were requested, they may be adapted or used in part.
- Please print this page for your records and send a copy of it to your publisher/graduate school.
- Appropriate credit for the requested material should be given as follows: "Reprinted (adapted) with permission from (COMPLETE REFERENCE CITATION). Copyright (YEAR) American Chemical Society." Insert appropriate information in place of the capitalized words.
- One-time permission is granted only for the use specified in your request. No additional uses are granted (such as derivative works or other editions). For any other uses, please submit a new request.

[BACK](#)

[CLOSE WINDOW](#)

Curriculum Vitae

Leanne Martin

Post-secondary Education

Western University

London, Ontario, Canada

2018-Present M.Sc Candidate Physical and Analytical Chemistry

Carleton University

Ottawa, Ontario, Canada

2014- 2018 Honours B.Sc Biochemistry and Biotechnology

Honours and Awards

Carleton University Dean's List

2014-2015, 2017-2018

Related Work Experience

Teaching and Research Assistant

Western University

2018-2020

Publications

L. M. Martin and L. Konermann "Enhancing Protein Electrospray Charge States by Multivalent Metal Ions: Mechanistic Insights from MD Simulations and Mass Spectrometry Experiments" *J. Am. Soc. Mass Spectrom.* 31, 25 (2020).

Conference Presentations

L. Martin and L. Konermann "Enhancing Protein Electrospray Charge States by Multivalent Metal Ions: Mechanistic Insights from MD Simulations and Mass Spectrometry Experiments" *32nd Annual Tandem Mass Spectrometry Workshop* - Lake Louise, Alberta, December 2019.

L. Martin and L. Konermann "Investigating the Mechanism of Multivalent Cation-Induced Protein Supercharging through MD Simulations and Native MS Experiments" *67th ASMS Conference on Mass Spectrometry and Allied Topics* - Atlanta, Georgia, June 2019.

UWO Course Work

Course	Weight	Grade
CHEM9494: Biophysical Chemistry	0.50	86
CHEM9544: Mass Spectrometry	0.50	96